Toward Quantum Opto-Mechanics in a Gram-Scale Suspended Mirror Interferometer

by

Christopher Wipf

Submitted to the Department of Physics
in partial fulfillment of the requirements for the degree of

Doctor of Philosophy

at the

MASSACHUSETTS INSTITUTE OF TECHNOLOGY

February 2013

Author . . . .
Department of Physics
January 11, 2013

Certified by. . . . .
Nergis Mavalvala
Professor of Physics
Thesis Supervisor

Accepted by . . . .
Krishna Rajagopal
Associate Department Head for Education

Toward Quantum Opto-Mechanics in a Gram-Scale Suspended Mirror Interferometer

by

Christopher Wipf

Abstract

A new generation of interferometric gravitational wave detectors, currently under construction, will closely approach the fundamental quantum limits of measurement, serving as a prominent example of quantum mechanics at the macroscale. Simultaneously, numerous experiments involving micro-mechanical oscillators are beginning to explore the quantum regime, with the help of optical cooling techniques.

We discuss the approach to the quantum regime in a gram-scale opto-mechanical experiment, and in large-scale gravitational wave detectors. The gram-scale experiment is designed so that radiation pressure forces completely dominate the dynamics of the mechanical mirror suspensions. We review a series of optical trapping and cooling techniques that we have demonstrated using this apparatus. A variant of these techniques is applied to a gravitational wave interferometer — yielding an effective temperature of 1.4 microkelvin and a phonon occupation number of 234 in a kilogram-scale oscillator. Then we analyze the displacement noise spectrum in the gram-scale system, which is currently limited by thermally driven fluctuations of the mirror suspensions. We identify methods for improving the suspension, in order to reveal the quantum fluctuations attributable to back-action of a displacement measurement. Finally, we propose a scheme for exploiting the opto-mechanical coupling in this system to generate optical entanglement.

Thesis Supervisor: Nergis Mavalvala
Title: Professor of Physics

Acknowledgments

It is a pleasure to thank the people who helped me complete this thesis, beginning with my advisor, Nergis Mavalvala. Nergis is a fierce and tireless advocate for her students. I am grateful not only for her sage advice and good humor, but also for the boundless support and encouragement she has offered me. We are truly lucky to have her at MIT. In addition, I thank Leonid Levitov and Vladan Vuletić for the dedication they showed during their service on my thesis committee.

I am deeply indebted to my lab-mates on the ponderomotive experiment: Thomas Corbitt, Tim Bodiya, and Eric Oelker. They formed an exceptionally smart, creative, and good-natured group of people to share my days with (on top of a sizable number of bleary-eyed nights together in the control room). I thank Thomas for blazing the trail, and for acting as an exemplary mentor. I thank Tim for the countless adventures we've shared, great and small, on the mountains of New Hampshire as well as in the lab. I thank Eric for asking excellent questions, and for his painstaking attention to detail in all aspects of the experiment. Also, I am grateful to Abraham Neben, whose contributions to this project included a beautifully convincing thermal noise model, and delicious chocolate chip cookies. I thank my "Kids' Room" office-mates Tim Bodiya, Sheila Dwyer, and Nicolás Smith-Lefebvre for their camaraderie and support.

Many more people both at MIT and elsewhere have given me much-appreciated help and advice, including: Sarah Ackley, Lisa Barsotti, Rolf Bork, Yanbei Chen, Fred Donovan, Matt Evans, Peter Fritschel, Keisuke Goda, Richard Hughes, Edith Innerhofer, Alex Ivanov, Florian Marquardt, Fabrice Matichard, Eugeniy Mikhailov, Rich Mittleman, Jane Nordholt, David Ottaway, Daniel Sigg, Stan Whitcomb, and Mike Zucker. Also, I have benefited greatly from the know-how of Myron MacInnis, and the resourceful administrative support of Marie Woods.

Most of all, I thank my loved ones: my fiancée Elizabeth, my parents, and the rest of my family, who have nourished me with their unconditional love and unflagging encouragement. This thesis is dedicated to the memory of my grandmother, Inez Craig, who loved me "enough for two gramas".

Contents

List of Figures

List of Tables

Chapter 1

Introduction

The program of experiments we discuss in this thesis has sprouted at the interface of general relativity and quantum mechanics, arguably the two greatest theoretical developments of 20th century physics.

An important progenitor and skeptic of both of these fields was Albert Einstein, who predicted in 1916, as a consequence of general relativity, the existence of propagating ripples in spacetime known as gravitational waves — and nearly withdrew his prediction in 1936, feeding a controversy that would linger on for decades more [71]. In quantum physics, Einstein provoked the field's other pioneers with his doubts about whether the new theory offered a complete description of the macroscopic world. For example, in a 1935 exchange with Erwin Schrödinger he grappled with a thought-experiment concerning a keg of unstable gunpowder, whose quantum state would evolve into a bizarre superposition of exploded and unexploded (a conundrum that Schrödinger intensified in his famous "Schrödinger's cat" paradox) [50].

Today, we are beginning to see both gravitational and quantum physics come into their own as experimental sciences. For one thing, we are building interferometric devices sensitive enough to deserve to be called *gravitational wave detectors*. We are also engineering quantum systems macroscopic, complex, and entangled enough to challenge our intuitions, in the manner of Schrödinger's cat. We are even finding that the interferometric gravitational wave detectors we are building *must* be thought of as quantum systems — quite macroscopic ones! — that are capable of exhibiting a

variety of quantum effects, such as back-action and entanglement.

1.1 The hunt for gravitational waves

Gravitational waves alternately stretch and squeeze the space through which they propagate. Their effect is analogous to a mechanical strain, resulting in a change in length ΔL that is proportional to the baseline L whose length is being monitored. (For a review, see reference [33].) The strongest gravitational wave sources that we can conceive of are astrophysical in nature, involving cataclysmic events such as stellar death explosions [106], collisions of black holes and neutron stars [2], and possibly the Big Bang itself [14]. Even for these sources, the predicted signals are exceedingly faint, with peak strains on the order of 10^{-21}.

Beginning in 1960, Joseph Weber brought gravitational waves into the realm of experiment [138], undaunted by the theoretical controversies still associated with the subject at that time. In a pioneering effort to make a direct detection, he deployed massive metallic bars, whose resonances would be excited by the fluctuating strain of a burst of gravitational waves. However, Weber's subsequent claims of detection [139] plunged the field into another vigorous dispute, as other experimental groups using his methods did not detect any such events [135, 83], while theorists struggled to explain how bursts of such staggering intensity could come about [57, 95].

As yet, no direct detection of gravitational waves has been confirmed, although compelling indirect evidence for their existence was provided by observations of orbital decay in the Hulse-Taylor binary pulsar system [134]. Today's most sensitive and wideband detectors use laser interferometry to monitor displacements across kilometer-scale baselines. The conceptual basis for this approach was suggested by Felix Pirani in 1956 [115], and a prototype was built in 1971 by Robert Forward (a former student of Weber) [97]. In 1972, Rainer Weiss made a comprehensive study of interferometric gravitational wave detection [140]. With remarkable foresight, his analysis charted essentially all of the noise sources that limit the performance of interferometers today.

Subsequently a global network of interferometers has developed, consisting of

the Laser Interferometer Gravitational-wave Observatory (LIGO), which operates detectors in the U.S. states of Washington and Louisiana [4], as well as the GEO600 detector in Germany [65] and the Virgo detector in Italy [10]. Activities within this network have been coordinated so as to improve the chance of multiple detections of the same event, in order to verify the detection and to localize the source of the waves.

In the *Initial LIGO* phase of operations, between 2002 and 2007, the LIGO detectors completed five "science runs" in which several years of observations were accumulated, at progressively higher levels of sensitivity. The sensitivity eventually attained the limits anticipated in the interferometer design. A sixth science run concluded in 2010, in an incrementally upgraded configuration known as *Enhanced LIGO*.

At present a more radical upgrade called *Advanced LIGO* is under construction. The new interferometers will have a target sensitivity substantially exceeding that of any previous detector, and they are widely expected to usher in the era of gravitational wave astronomy.

1.2 Macroscopic quantum mechanics

In Advanced LIGO, quantum fluctuations have emerged as the fundamental limit to measurement across a broad band of frequencies. It is a striking fact that the scale of displacement these interferometers must measure to detect gravitational waves of astrophysical origin (about 10^{-19} m) is also the scale at which the quantum mechanics of the interferometer becomes important. This is, however, no coincidence, since the quantum limit is what will always remain to challenge us in a carefully engineered instrument, where every other species of noise has been wrung out of the data.

Gravitational wave interferometers are among the largest of the many categories of mechanical systems now poised to explore the quantum regime. Macroscopic quantum mechanics has emerged as an active and global experimental research program in its own right. As the subject of thought experiments, it can be traced back at least to Einstein and Schrödinger's exchange. Subsequently, theoretical investigations

were motivated by the quantum measurement limits in gravitational wave detection, including pioneering work by Braginsky and Manukin [24], and Caves [35, 34]. A further impetus was provided by the impressive experimental progress seen in laser cooling and control of ions and atoms. Numerous proposals were advanced for observing quantum behavior such as unitary evolution, superposition, entanglement, and decoherence in opto-mechanical systems [85, 20, 136]

Within the past decade, a remarkably wide assortment of micro-mechanical experiments have marched toward the ground state of motion, an initial milestone marking the quantum regime. (The status of the field was recently reviewed in reference [17].) The feature uniting most of these systems is that cooling techniques that exploit strong optical forces have proven to be an essential resource.

1.3   Ponderomotive interferometer

Quantum back-action, also called radiation pressure noise, is likely to be the first signature of quantum mechanics accessible in gravitational wave interferometers and related systems. With this in mind, we have worked on modeling, constructing, and debugging a *ponderomotive interferometer*, designed to allow radiation pressure to play as prominent a role as possible. The motivation for this experiment arose from the challenges faced by future gravitational wave detectors, in which radiation pressure and quantum noise were expected to become important. However, we soon became aware of, and were inspired by the parallels between our efforts, and those of the community of researchers pushing micro-mechanical devices toward the quantum ground state.

The ponderomotive interferometer is designed around gram-scale suspended mirrors and meter-scale optical path lengths — straddling the kilogram-kilometer scale of gravitational wave interferometers, and the sub-microgram, sub-millimeter scale typical of micro-mechanics. Distinct from the micro-mechanical community, it features very compliant mirror suspensions: its mirrors respond to an applied force almost as free masses would do. As a result, in our experiment the radiation pressure forces can

completely overwhelm the mechanical restoring and damping forces exerted by the suspension. We have exploited this feature to demonstrate powerful new methods for optical trapping and cooling of macroscopic mirrors. We also expect to observe quantum back-action in this system, as well as quantum correlations of the optical field induced by the opto-mechanical coupling.

The rest of this thesis is organized as follows. Chapter 2 offers a review of quantum opto-mechanics, culminating with the Standard Quantum Limit and ponderomotive squeezing of the quantum noise of light. In chapter 3, we present the design and the current experimental status of the ponderomotive interferometer. Chapter 4 tells the story of a sequence of experiments demonstrating trapping and cooling of gram-scale and kilogram-scale mirrors. We also discuss the prospects for attaining the quantum ground state via these techniques. Chapter 5 analyzes thermal fluctuations of the gram-scale mirror suspension, which have so far prevented us from observing quantum back-action in the ponderomotive interferometer. An approach is suggested for mitigating the suspension thermal noise. In chapter 6 we propose a method for entangling optical fields in the ponderomotive interferometer. Finally, we discuss the outlook for future experimental work in chapter 7.

Chapter 2

Theoretical foundations

In this chapter, we provide the conceptual background needed to understand the design of the ponderomotive interferometer, and to motivate the goals we have for its performance. In section 2.1, we review topics from optical interferometry. Then we introduce the opto-mechanical coupling of light and the mirrors of an interferometer in section 2.2. Finally, in section 2.3, we progress to a fully quantum treatment of the opto-mechanical system.

2.1   Interferometry

Interference is a well known effect in optics, observed when two phase-coherent optical fields overlap. It serves as powerful evidence of the wave nature of light. *Interferometry* is a precision measurement technique that involves superimposing optical fields to generate a pattern of interference fringes, and then measuring some aspect of that pattern. Often the goal is to learn about phenomena that influence the phase of the optical fields in the interferometer. For example, as we noted in chapter 1, a passing gravitational wave may cause the length of an optical path to vary, hence modulating the phase.

Since an optical field oscillates on an ultra-fast timescale (10^{-14} seconds or less), its phase is sensitive to extremely subtle effects. But for the same reason, it is also quite
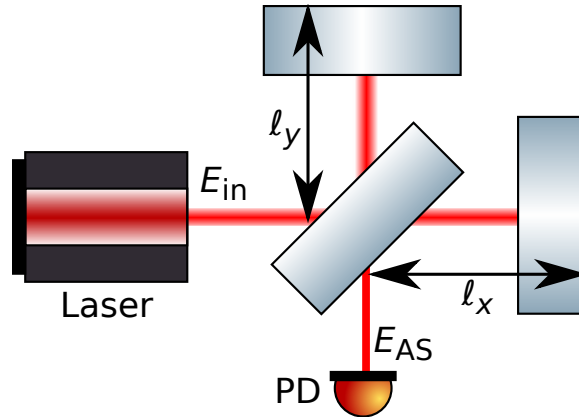
Figure 2-1: Schematic layout of a Michelson interferometer, illustrating the optical fields and path lengths.

difficult to register the phase directly.* However, the brightness of an interference fringe is a phase-sensitive observable that is simple to quantify using a photodetector (and may well be visible to the eye).

In the following sections we introduce the building blocks for the ponderomotive interferometer: the Michelson interferometer, and the optical cavity.

2.1.1 Michelson interferometer

The key feature of the Michelson interferometer is that it allows us to make measurements that are unaffected (to first order, at least) by fluctuations of the amplitude and phase of the light source. Albert Michelson in 1881 [94] managed to observe interference fringes in his apparatus lit by flickering, incoherent white light from a burning flame — demonstrating the power of a clever experimental design in overcoming technological limitations.

The optical layout of the Michelson interferometer is shown in figure 2-1. Suppose the optical field applied to the input port (also called the symmetric port) of the beamsplitter is E_{in}. Then after propagating the field in each arm out to the end mirror, and back to recombine at the beamsplitter, the field at the output port (or

---

*Although it has recently become *possible* to record the waveform of an optical field directly [62], interferometric techniques remain far more developed and easier to apply.

antisymmetric port) can be written as follows:

$$\widetilde{E}_{AS} = (\widetilde{E}_{\text{in}} t_{BS} e^{i\Omega l_x/c} r_X e^{i\Omega l_x/c} r_{BS}) - (\widetilde{E}_{\text{in}} r_{BS} e^{i\Omega l_y/c} r_Y e^{i\Omega l_y/c} t_{BS}) \qquad (2.1)$$

Here we are working in the frequency domain,[†] so that $\widetilde{E}$ denotes the Fourier component of the field varying at frequency Ω. The variables r_j and t_j denote the amplitude reflectivity and transmissivity of the optical element j.

We will assume a perfectly balanced (50:50) beamsplitter and neglect losses, so that $r_{BS} = t_{BS} = 1/\sqrt{2}$, and $r_X = r_Y = 1$. Then the output field simplifies to

$$\widetilde{E}_{AS} = \frac{1}{2}(e^{2i\Omega l_x/c} - e^{2i\Omega l_y/c})\widetilde{E}_{\text{in}} \qquad (2.2)$$

Note that if the arm lengths are made identical, then $\widetilde{E}_{AS} \to 0$ for all Ω, and so the fringe at the antisymmetric port is dark — no matter what the characteristics of the light source are. For a nearly monochromatic source such as a laser, operating at a frequency $\Omega = \omega_0$ (wavelength $\lambda = 2\pi c/\omega_0$), the fringe becomes dark whenever $l_x - l_y$ is equal to an integer number of half-wavelengths. In the rest of this section, we will assume such a source is being used. This allows us to drop the frequency domain notation, since we consider only a single frequency component. Then the power emerging from the antisymmetric port is given by

$$\begin{aligned} P_{AS} &= |E_{AS}|^2 \\ &= P_{\text{in}} \sin^2 \phi \end{aligned} \qquad (2.3)$$

where $\phi = (l_x - l_y)\omega_0/c$.

The fringe at the antisymmetric port can be used as a readout for small displacements of the differential arm length $l_x - l_y$. Perhaps the simplest strategy for this is to adjust the arm lengths, introducing an offset in ϕ, in order to move the antisymmetric

---

[†]We adopt the following conventions for frequency domain calculations in this thesis. The complex exponential propagation factor is $e^{-i\Omega(t-x/c)}$, so that $\frac{d}{dt} \to -i\Omega$. The Fourier transform is defined by $\widetilde{x} = \int dt\, x e^{i\Omega t}$, and the inverse transform is defined by $x = \int \frac{d\Omega}{2\pi} \widetilde{x} e^{-i\Omega t}$. The power spectral density, denoted $S_x(\Omega)$, is one-sided and its units are spectral power per 1 Hz bandwidth.

port away from the dark fringe slightly. Then P_{AS} becomes linearly dependent on small fluctuations $\delta\phi$, with the slope given by

$$\frac{dP_{AS}}{d\phi} = 2P_{\text{in}} \sin\phi \cos\phi \tag{2.4}$$

The offset in ϕ should be kept small, for two reasons. First, away from the dark fringe, P_{AS} becomes increasingly sensitive to any technical imperfections (excess amplitude and phase fluctuations) of the laser. Second, even if the laser is ideal, the fundamental *shot noise* associated with photodetection of laser light grows as more power is detected. Its power spectral density is[‡]

$$S_P^{(S)}(\Omega) = 2\hbar\omega_0 P \tag{2.5}$$

By combining equations (2.3)–(2.5), we can obtain the power spectral density of a measurement of $\delta\phi$, as limited by shot noise:

$$\begin{aligned} S_{\delta\phi}^{(S)}(\Omega) &= \left(\frac{dP_{AS}}{d\phi}\right)^{-2} S_{P_{AS}}^{(S)}(\Omega) \\ &= \frac{\hbar\omega_0}{2P_{\text{in}}} \frac{1}{\cos^2\phi} \end{aligned} \tag{2.6}$$

This result confirms that the measurement sensitivity is optimized near the dark fringe.

We note that in practice, achieving the shot noise limit using this simple readout strategy can be a challenge — especially in interferometers that are more elaborate than the simple Michelson arrangement [89, 52]. In our experiment, it is convenient to use a slightly more complex Michelson readout scheme, the discussion of which is deferred to chapter 3.

[‡]The presence of Planck's constant in equation (2.5) is an indication that shot noise is rooted in the quantum fluctuations of the light. We will treat the effect more systematically in section 2.3 below, where the quantum description of the optical field is introduced.
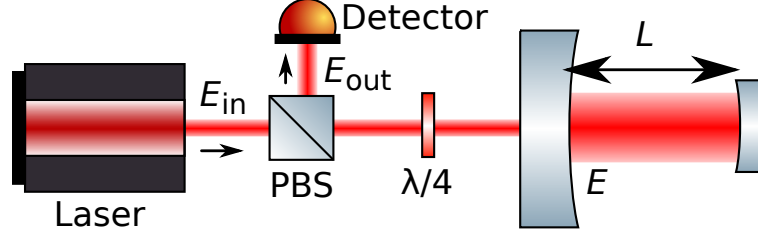
Figure 2-2: Schematic layout of a Fabry-Perot optical cavity. The polarizing beamsplitter (PBS) and quarter wave plate ($\lambda/4$) separate the reflected field E_{out} from the input field E_{in}. In this configuration a phase-sensitive detector (such as a homodyne detector) must be used to monitor the cavity displacement. We use a different readout strategy in the experiment, which is discussed in chapter 3.

2.1.2 Optical cavity

An optical cavity (or Fabry-Perot interferometer) is composed of two mirrors that face each other, as depicted in figure 2-2. Light can undergo repeated reflections back and forth, making numerous round trips inside the cavity, which prolongs and intensifies the interaction between the optical field and the mirrors.

Interference occurs at the input mirror, which is weakly transmissive with amplitude reflectivity r_I slightly less than 1. (The end mirror we idealize as a perfect reflector.) When the cavity is illuminated with a field E_{in}, a small portion of the incoming light leaks through the input mirror, into the cavity. Neglecting losses, we can write this field as $t_I E_{\text{in}}$, where $t_I = \sqrt{1 - r_I^2}$ is the input mirror's amplitude transmissivity. If the light source has been on for some time, there will also be light reflecting from the inside surface of the input mirror, which has already made one or more round trips within the cavity. We need to sum up these components in order to find the total cavity field E:

$$
\begin{aligned}
\widetilde{E} &= t_I \widetilde{E}_{\text{in}} + t_I \widetilde{E}_{\text{in}} r_I e^{2i\Omega L/c} + t_I \widetilde{E}_{\text{in}} (r_I e^{2i\Omega L/c})^2 + \ldots \\
&= \frac{t_I}{1 - r_I e^{i\phi(\Omega)}} \widetilde{E}_{\text{in}}
\end{aligned}
\tag{2.7}
$$

where $\phi(\Omega) = 2\Omega L/c$ is the round trip phase.

Note that perfect constructive interference occurs whenever the cavity length L is equal to an integer number of half-wavelengths, so that $\phi \equiv 0 \mod 2\pi$. Near these

working points, the cavity exhibits a resonant response. To better characterize this response, we will consider a small offset $\delta\phi \ll 1$ in the vicinity of a resonance at frequency $\Omega = \omega_c$, and then approximate the cavity field as a rational function (using the Padé approximant). We find that

$$\widetilde{E} \approx \frac{2}{t_I} \frac{1}{1 - i\frac{2\,\delta\phi}{t_I^2}} \widetilde{E}_{\text{in}} \tag{2.8}$$

Here we have also assumed $t_I \ll 1$, and kept only the leading order terms in t_I and $\delta\phi$.

For a monochromatic light source, the optical power inside the cavity near resonance can be written as follows:

$$\begin{aligned}
P &= |E|^2 \\
&\approx \frac{4}{t_I^2} \frac{1}{1 + (\frac{2\,\delta\phi}{t_I^2})^2} P_{\text{in}} \\
&= \frac{4}{t_I^2} \frac{1}{1 + \delta^2} P_{\text{in}}
\end{aligned} \tag{2.9}$$

Defining $\delta = 2\,\delta\phi/t_I^2$, we can see that equation (2.9) for the intracavity power is a Lorentzian in δ. The parameter δ we refer to as the cavity's *dimensionless detuning*, or simply the detuning. In these units the cavity linewidth[§] is normalized to 1. However, it is also very common to speak of the detuning in units of frequency, where it is defined as $\Delta = \omega_0 - \omega_c = \gamma_c \delta$, and $\gamma_c = \dfrac{t_I^2 c}{4L}$ is the linewidth in (angular) frequency units. There are two further cavity parameters that it is useful to be aware of: the *free spectral range* $\text{FSR} = \dfrac{c}{2L}$ is the spacing between cavity resonances in (ordinary) frequency units; and the *finesse* $\mathcal{F} = \text{FSR}\,\pi/\gamma_c$ is the ratio of the FSR to a resonance's full width.

Since we are neglecting losses, and the end mirror is totally reflective, all the optical power that is incident on the input mirror must ultimately be reflected back toward the light source. The reflected field E_{out} has two components: the prompt

---

[§]The linewidth as it is defined here refers to the half width at half maximum (HWHM) of the resonance.

reflection of the field E_{in} from the input mirror, and the leakage of the cavity field E. We write it as

$$
\begin{aligned}
\widetilde{E}_{\mathrm{out}} &= r_I \widetilde{E}_{\mathrm{in}} - t_I e^{2i\Omega L/c} \widetilde{E} \\
&\approx -\widetilde{E}_{\mathrm{in}} e^{2i\delta}
\end{aligned}
\tag{2.10}
$$

Notice that near the resonance, the phase of the reflected field E_{out} is linear in the detuning δ, with a slope of 2. Thus it is also linear in the cavity round trip phase $\delta\phi$, with a slope of $4/t_I^2 = 2\mathcal{F}/\pi$. In other words, the phase of E_{out} behaves as though the input light had made the round trip between the mirrors $2\mathcal{F}/\pi$ times, each time incrementing its phase by $\delta\phi$. In a high finesse cavity, this gain factor may be enormous — which makes such cavities very useful for optical sensing applications.

However, the tradeoff is that the phase of E_{out} has a linear response only in a narrow range around the resonance. If the cavity is allowed to drift away from resonance, the prompt reflection soon dominates over the cavity signal, and so the sensitivity to the round trip phase becomes almost nil.

2.2   Opto-mechanics

Since the theory of electromagnetic radiation was set forth by James Clerk Maxwell, it has been understood that light carries momentum, which it can impart to matter that it comes into contact with. This radiation pressure, though omnipresent, is so feeble that we seldom notice it in everyday life. However, if you have ever observed a comet's tail projecting away from the sun, you have witnessed radiation pressure in action. The effect also plays an important role in understanding how the interior structure of a star supports itself against gravity, how matter in the early universe behaved shortly after the big bang, and a variety of other phenomena in the domain of astrophysics.

In 1873, Maxwell [91] had already anticipated that a laboratory demonstration of radiation pressure should be possible, writing that "the concentrated rays of the electric lamp... falling on a thin metallic disk, delicately suspended in a vacuum, might

perhaps produce an observable mechanical effect." A number of early experiments were made in pursuit of this goal, all of them plagued to some degree by residual gas effects.¶ The first widely accepted experimental results were obtained in 1900 by Lebedev [81], and independently by Nichols and Hull in 1901 [102]. This body of work is now recognized as the genesis of the field of opto-mechanics.

Subsequently, in the 1960s, Braginsky inaugurated the study of *dynamic* effects of radiation pressure in a cavity, both theoretically [22], and in an experiment using a microwave resonator [23]. The effects that were identified by Braginsky and co-workers arise from a kind of feedback that can develop in the dynamics of the mirrors and the cavity field. The conditions under which this feedback occurs are the following:

- One (or more) of the cavity mirrors is movable.

- The radiation pressure force is strong enough to have an appreciable influence on the movable mirror.

- The cavity is detuned to either side of a resonance.

In these circumstances, the radiation pressure force,

$$F_{RP} = \frac{2P}{c} \tag{2.11}$$

causes a displacement of the movable mirror. This displacement alters the detuning of the cavity, thereby imposing a change in the intra-cavity power P according to equation (2.9). As the intra-cavity power changes, so does the radiation pressure force in equation (2.11) — thus closing the feedback loop. The feedback may be either positive or negative depending on the sign of the detuning. Figure 2-3 offers a graphical interpretation of this phenomenon, which is sometimes called "dynamical back-action".

¶A well known example is the Crookes radiometer, consisting of a black-and-white "light mill" structure in a partially evacuated bulb. Residual gas effects are far in excess of radiation pressure in this device.
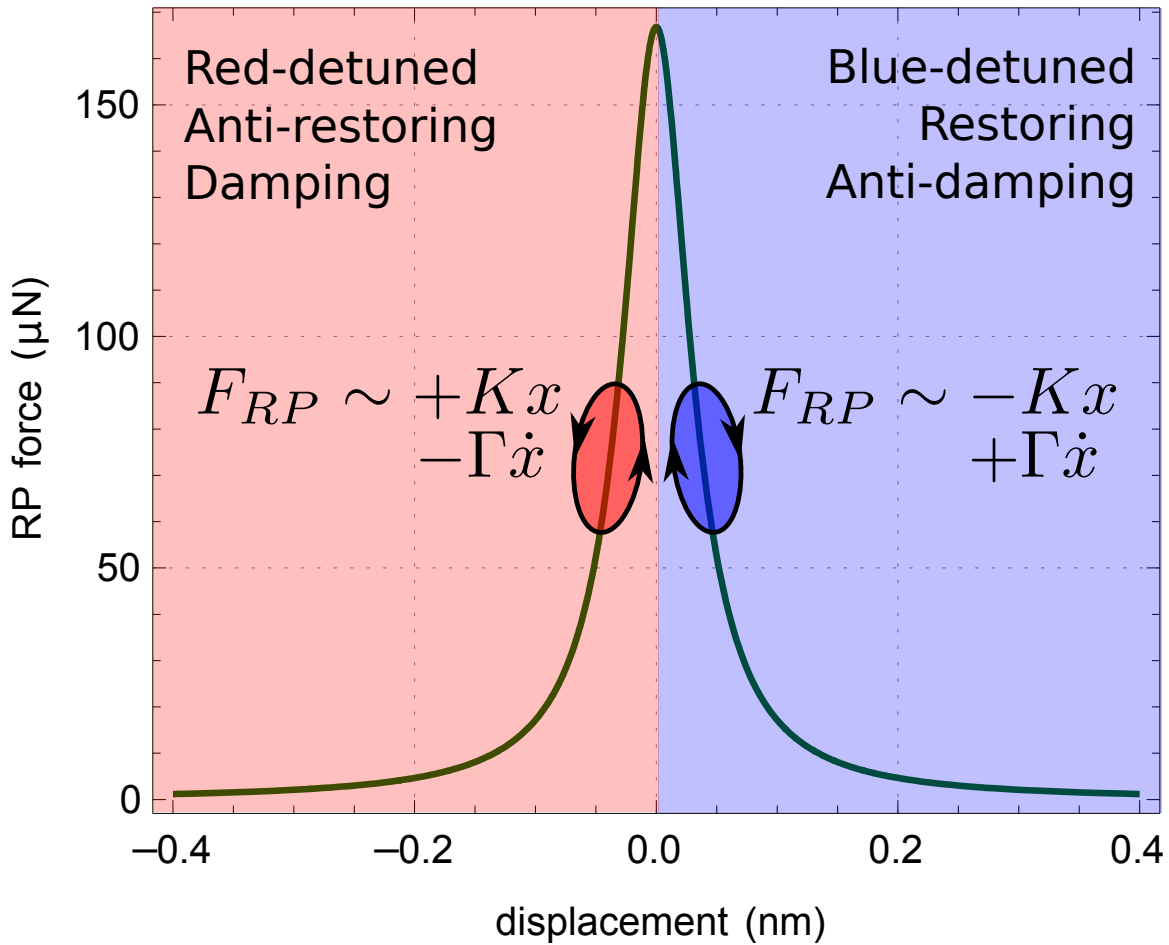
Figure 2-3: Classification of the radiation pressure forces that arise in a detuned optical cavity. The force becomes linearly dependent on the mirror displacement, giving rise to a spring-like force on one side of the resonance and an anti-spring on the other. The ellipses represent the fact that the intra-cavity power lags the mirror motion, resulting in a type of hysteresis that can either extract work from the mirror (damping it) or do work on it (anti-damping), depending again on the sign of the detuning.

2.2.1 Optical spring

In a detuned cavity, the dynamic radiation pressure force has a component that is linearly proportional to the fluctuating displacement of the movable mirror. Typically such fluctuations are kept small, and so this linear component dominates over the nonlinear terms. A force that is linear in displacement is analogous to the restoring force of a mechanical spring. Accordingly, this aspect of the radiation pressure force has come to be known as the *optical spring* [29, 27, 128, 96, 38].

The optical spring can be described by a spring constant K_o, which is given by

$$
\begin{aligned}
K_o &= -\frac{dF_{RP}}{dL} \\
&= -\frac{2}{c}\frac{dP}{d\delta}\frac{d\delta}{dL} \\
&= \frac{8P_{\text{in}}\omega_0}{\gamma_c^2 L^2}\frac{\delta}{2}\left(\frac{1}{1+\delta^2}\right)^2
\end{aligned}
\tag{2.12}
$$

provided that the cavity is illuminated by a laser with power P_{in} and frequency ω_0. Note that the sign of the detuning δ controls the sign of the spring constant. While a positive detuning (in our convention) corresponds to a spring-like restoring force, a negative detuning results in an *anti*-restoring force. An anti-restoring force, rather than opposing the movable mirror's departure from equilibrium, actually accelerates it (which tends to destabilize the cavity).

If the movable mirror has mass m, then we can assign a resonant frequency $\Omega_o^2 = K_o/m$ to the optical spring. Interpreting the pre-factor of equation (2.12) in terms of a characteristic frequency Ω_q, we can write

$$
\Omega_q^2 = \frac{8P_{\text{in}}\omega_0}{m\gamma_c^2 L^2}
\tag{2.13}
$$

$$
K_o = m\Omega_q^2 \frac{\delta}{2}\left(\frac{1}{1+\delta^2}\right)^2
\tag{2.14}
$$

For the moment, Ω_q merely represents a convenient bundle of parameters. However, it will take on a deeper significance in section 2.3 below, when we discuss the quantum limit of monitoring the mirror displacement.

A particularly interesting situation occurs when the optical spring overwhelms the spring constant of the movable mirror's suspension, $K_m = m\Omega_m^2$. Then the mirror no longer resonates at Ω_m, but at a new frequency $\Omega_{\text{eff}}^2 = (K_m + K_o)/m$, thus providing a mechanical mode whose dynamics can be controlled by optical means. Several advantages and applications of this regime will be discussed later on, in chapters 4 and 6.

Finally, notice that we have tacitly assumed in this calculation that the cavity field responds *instantaneously* to the movable mirror. This assumption is also known as the quasistatic (or adiabatic) limit. It is a valid approximation when considering mirror motion at frequencies that are negligible compared to the cavity linewidth γ_c.

However, when we correctly account for the dynamics of the cavity field, we will discover that the optical spring "constant" becomes frequency dependent. In fact, at high frequencies the restoring (or anti-restoring) force must weaken, because the cavity field cannot build up and decay fast enough to keep up with arbitrarily fast motion of the movable mirror. The full optical spring constant $K_o(\Omega)$ will be derived in section 2.3 below. Here we simply quote the result:

$$K_o(\Omega) = m\Omega_q^2 \frac{\delta}{2} \left(\frac{1}{1+\delta^2} \right) \left(\frac{1}{(1-i\Omega/\gamma_c)^2 + \delta^2} \right) \qquad (2.15)$$

It is evident that equations (2.14) and (2.15) agree in the limit where $\Omega \ll \gamma_c$.

It is also apparent that as Ω increases, K_o rotates in the complex plane, acquiring an imaginary component. The implications of this imaginary part of the spring constant will be considered next.

2.2.2 Optical damping

We can relax the quasistatic limit somewhat by expanding $K_o(\Omega)$ in Ω. Then the zeroth order term recovers the quasistatic spring constant of equation (2.14), while the linear term is purely imaginary:

$$K_o(\Omega) = m\Omega_q^2 \frac{\delta}{2} \left(\frac{1}{1+\delta^2} \right)^2 \left(1 + i\Omega \frac{2}{\gamma_c} \frac{1}{1+\delta^2} + \dots \right) \qquad (2.16)$$

In the frequency domain, the $i\Omega$ term takes the time derivative of the displacement, so this added term represents a force that is proportional to the velocity, rather than the position. In other words, it describes viscous damping, with a damping rate[||] given by

$$
\begin{aligned}
\Gamma_o &= -\frac{\text{Im}\{K_o\}}{m\Omega} \\
&= -\frac{\Omega_q^2}{\gamma_c}\delta\left(\frac{1}{1+\delta^2}\right)^3
\end{aligned}
\tag{2.17}
$$

Ordinary viscous damping takes place when the detuning is negative, but a positive detuning gives rise to *anti*-damping. An anti-damping force causes small oscillations of the movable mirror to grow exponentially in amplitude. (Like an anti-restoring force, it is a destabilizing effect.)

Finally, just as it is possible for the optical restoring force to overwhelm its mechanical counterpart, the optical damping force may also dominate, so that the new effective damping rate for the mirror becomes $\Gamma_{\text{eff}} = \Gamma_m + \Gamma_o$. We will revisit the topic of optical damping forces in chapter 4.

2.2.3 Parametric instability

Under the opto-mechanical coupling we have been discussing, the cavity mode can be thought of as a parametric oscillator, whose resonant frequency $\omega_c(L)$ is a function of the displacement of the movable mirror. Optical anti-damping of the mirror, if strong enough to make the total effective damping Γ_{eff} negative, will destabilize the system, resulting in a *parametric instability*. Although the phenomenon is generic, we most often use the term "parametric instability" to refer to a specific type of opto-mechanical interaction, involving one or more of the internal vibrational modes of a cavity mirror [26, 70, 25, 144, 38].

These modes are engineered to be quite stiff, in order to keep the mirror surface rigid. As a result, the resonances may be found at frequencies well above the cavity

---

[||]The damping rate as we define it turns out to be equal to the full width at half maximum (FWHM) of the resonance. However, recall that the linewidth was defined as the HWHM. We live with this minor discrepancy because it simplifies the presentation, absorbing many factors of 2. In our notation damping rates are written uppercase (Γ) and linewidths are lowercase (γ).

linewidth. Typically, the optical restoring force has a negligible effect on the dynamics of such a mode.

Nonetheless, if the mode's mechanical quality factor $Q_m = \Omega_m/\Gamma_m$ is high (implying a small damping rate Γ_m), then the dynamics may be tipped into instability by even a modest optical anti-damping force. Note that it is desirable to make cavity mirrors out of very low-loss materials in order to minimize thermal fluctuations of the mirror surface, which results in a high quality factor for the internal modes. (See chapter 5 for more discussion on thermal noise.) The consequence is that parametric instabilities are easily triggered, and they may limit the power handling ability of the cavity or the range of detunings where it can be operated.

The "relaxed" quasistatic approximation we introduced in the previous section is not adequate to describe the situation where the mode frequency of interest is outside the cavity linewidth. Instead we have to go back to the full expression for the complex spring constant given in equation (2.15). Then we find that for frequencies $\Omega \gtrsim \gamma_c$, the optical damping rate has a frequency dependence:

$$
\begin{aligned}
\Gamma_o(\Omega) &= -\frac{\mathrm{Im}\{K_o(\Omega)\}}{m\Omega} \\
&= -\frac{\Omega_q^2}{\gamma_c}\delta \left(\frac{1}{1+\delta^2}\right)\left(\frac{1}{(1+\delta^2+(\Omega/\gamma_c)^2)^2+4(\Omega/\gamma_c)^2}\right)
\end{aligned}
\tag{2.18}
$$

At frequencies $\Omega \gg \gamma_c, \gamma_c\delta$, it can be seen that $\Gamma_o(\Omega)$ is aggressively filtered by the cavity, and scales as $\gamma_c\Omega^{-4}$. Therefore, an effective way to minimize parametric instabilities is to arrange that the cavity linewidth is small relative to the mirror internal mode frequencies.

We note, however, that in very long cavities (like those found in gravitational wave interferometers) the picture is more complicated, because the internal mode frequencies may be comparable to the cavity FSR. Consequently, mechanical modes can scatter light into other optical modes of the cavity. This hazard was pointed out by Braginsky and co-workers [26]. Fortunately it does not arise for the tabletop-scale interferometer that is the focus of this thesis, where the FSR is 150 MHz or more.

2.3 Quantum opto-mechanics

In this section, we present a review of the quantum mechanical model of an optical cavity with a movable mirror. We follow the quantum Langevin approach set forth in references [53, 60] and many other recent papers. Starting from the Hamiltonian, we will derive the equations of motion and solve them, verifying that they reproduce the previously discussed classical dynamics of the optical spring. We will also uncover the fundamental limit of displacement sensitivity in this system: the quantum noise.

2.3.1 Radiation pressure Hamiltonian

The paradigmatic example of an opto-mechanical system is a Fabry-Perot cavity in which one (weakly transmitting) mirror is fixed, and the other (perfectly reflecting) mirror can move along the cavity axis, being suspended as a harmonic oscillator. The light in the cavity couples to the position of the movable mirror through radiation pressure. The Hamiltonian of this system is written as follows:

$$H_s = \hbar\omega_c a^\dagger a + \frac{p^2}{2m} + \frac{1}{2}m\Omega_m^2 x^2 + H_{\text{int}} \qquad (2.19)$$

The first term represents the energy of the quantized electromagnetic field in the cavity mode, with resonant frequency ω_c and annihilation operator $a^\dagger, a$. The next two terms describe the energy of the quantized movable mirror, with mass m, resonant frequency Ω_m, momentum operator p and position x. The non-vanishing commutation relations are $[x, p] = i\hbar$ and $[a, a^\dagger] = 1$.

The radiation pressure interaction is governed by the H_{int} term:

$$H_{\text{int}} = -\hbar\omega_c a^\dagger a \frac{x}{L} \qquad (2.20)$$

A very simple, albeit informal justification for this term can be given, following reference [108]. First we recall that for a fixed position of the movable mirror, the Hamiltonian is $H_0 = \hbar\omega_c a^\dagger a$, and ω_c is related to the cavity length according to $\omega_c = n\pi c/L$, where n is a positive integer. If the mirror is now moved slightly

$(L \rightarrow L + x)$, the Hamiltonian becomes

$$
\begin{aligned}
H_0' &= \hbar \omega_c \frac{L}{L + x} a^\dagger a \\
&\approx \hbar \omega_c a^\dagger a \left(1 - \frac{x}{L} \right) \\
&= H_0 + H_{\text{int}}
\end{aligned}
\tag{2.21}
$$

It should be noted that the Hamiltonian H_s considers only a single cavity mode, and we have so far ignored couplings to the fields outside the cavity. We were obliged to assume that the mirror's displacement is small $(x \ll L)$, in order to approximate H_{int} as linear in equation (2.21). We also assumed that the mirror's motion is slow $(\Omega_m \ll \text{FSR})$, so that no photons are scattered into other cavity modes. (A more rigorous and general treatment relaxing these assumptions was offered by Law [80].)

In order to include the illumination of the cavity by a laser source, we can add a driving term [60]

$$
H_d = i \hbar \mathcal{E}_{\text{in}} (a^\dagger e^{-i\omega_0 t} - a e^{i\omega_0 t})
\tag{2.22}
$$

which describes a coherent driving field at frequency ω_0 (which may be detuned from ω_c). The coupling rate is $|\mathcal{E}_{\text{in}}| = \sqrt{2 P_{\text{in}} \gamma_c / (\hbar \omega_0)}$.

The environment and its couplings add still more terms to the Hamiltonian [53]:

$$
H_{se} = \hbar \sum_n \omega_n a_n^\dagger a_n + \hbar \sum_n g_n \left(a_n^\dagger a + a^\dagger a_n \right) + \sum_n \left(\frac{p_n^2}{2 m_n} + \frac{1}{2} m_n \Omega_n^2 (x_n - x)^2 \right)
\tag{2.23}
$$

including couplings for the cavity field (second term) and mirror (third term). Both degrees of freedom are coupled to baths of harmonic oscillators. The couplings look different because we assume the cavity field evolves rapidly compared to its relaxation time $(\omega_c \gg \gamma_c)$: thus we ignore all $a_n a$ and $a_n^\dagger a^\dagger$ terms, which carry an $e^{\pm 2 i \omega_c t}$ dependence in the rotating frame. The mirror has a more general linear coupling appropriate for the case of quantum Brownian motion.

Collecting all of these terms, we write the total Hamiltonian as

$$
H = H_s + H_d + H_{se}
\tag{2.24}
$$

35

2.3.2 Quantum Langevin equations

The "quantum Langevin equations" are merely the Heisenberg equations of motion for the system operators a, x, and p, under the Hamiltonian we have just described. Writing them in the interaction picture with respect to $\hbar\omega_0 a^\dagger a$, we obtain

$$
\begin{aligned}
\dot{x} &= \frac{p}{m} \\
\dot{p} &= -m\Omega_m^2 x - \Gamma_m \frac{p}{m} + \frac{\hbar\omega_c}{L} a^\dagger a + F_T \\
\dot{a} &= -(\gamma_c - i\omega_0 + i\omega_c)a + i\omega_c \frac{x}{L} a + \mathcal{E}_{\text{in}} + \sqrt{2\gamma_c}\, a_{\text{in}}
\end{aligned}
\tag{2.25}
$$

Here F_T and a_{in} are the noise operators that we get by taking the continuum limit of the environmental couplings to the mirror and cavity field, respectively [53].

This is a set of coupled, nonlinear differential equations for the system operators. An approximate solution can be found for the case of an intense, steady driving field. Under these conditions the system settles into a steady state where the cavity field has a coherent amplitude $\bar{a}$ and the mirror has a mean displacement $\bar{x}$. After taking expectation values of the above equations (with time derivatives set to zero), they reduce to the following:

$$
\begin{aligned}
\bar{x} &= \frac{\hbar\omega_c |\bar{a}|^2}{m\Omega_m^2 L} \\
\bar{a} &= \frac{1}{\gamma_c} \frac{\mathcal{E}_{\text{in}}}{1 - i\delta}
\end{aligned}
\tag{2.26}
$$

a set of coupled, nonlinear algebraic equations whose solution determines the steady state. In this step we have introduced the cavity field detuning, which includes a correction for the mirror's mean displacement:

$$
\delta = \frac{\omega_0}{\gamma_c} - \left(1 - \frac{\bar{x}}{L}\right)\frac{\omega_c}{\gamma_c}
\tag{2.27}
$$

Note that since we are free to choose the phase of the input field in $\mathcal{E}_{\text{in}}$, we can adjust it so that $\bar{a}$ is real, which will streamline our calculations:

$$
\bar{a} = \frac{1}{\gamma_c} \frac{|\mathcal{E}_{\text{in}}|}{\sqrt{1 + \delta^2}}
\tag{2.28}
$$

The next step is to simplify the quantum Langevin equations by linearizing around the steady state. From each operator O we subtract off the classical steady state mean $\bar{O}$, leaving only the quantum fluctuation operator. (For brevity, we will just relabel $O - \bar{O}$ as O.) The fluctuations are assumed small, and their cross-couplings neglected. The resulting equations are:

$$\dot{x} = \frac{p}{m}$$
$$\dot{p} = -m\Omega_m^2 x - \Gamma_m \frac{p}{m} + \frac{\hbar\omega_c}{L}\bar{a}\left(a^\dagger + a\right) + F_T \qquad (2.29)$$
$$\dot{a} = -(1 - i\delta)\gamma_c a + i\omega_c \bar{a}\frac{x}{L} + \sqrt{2\gamma_c}a_{\text{in}}$$

The linearized equations are straightforward to solve in the frequency domain:

$$-i\Omega\widetilde{x} = \frac{\widetilde{p}}{m}$$
$$-i\Omega\widetilde{p} = -m\Omega_m^2\widetilde{x} - \Gamma_m \frac{\widetilde{p}}{m} + \frac{\hbar\omega_c}{L}\bar{a}\left(\widetilde{a}^\dagger + \widetilde{a}\right) + \widetilde{F}_T \qquad (2.30)$$
$$-i\Omega\widetilde{a} = -(1 - i\delta)\gamma_c\widetilde{a} + i\omega_c\bar{a}\frac{\widetilde{x}}{L} + \sqrt{2\gamma_c}\widetilde{a}_{\text{in}}$$

In the solution, it is convenient to express the optical fields in terms of the quadrature operators $X = (a^\dagger + a)/\sqrt{2}$ and $Y = i(a^\dagger - a)/\sqrt{2}$, often called the amplitude quadrature and phase quadrature, respectively. The quadrature operators are Hermitian, describing physical quantities that can be measured using a homodyne detector.

Solving first for the mirror dynamics, we find:

$$\widetilde{x} = \chi(\Omega)(\widetilde{F}_T + \widetilde{F}_{RP})$$
$$\chi(\Omega) = \frac{1}{K_m(\Omega) + K_o(\Omega) - m\Omega^2} \qquad (2.31)$$

where $\chi(\Omega)$ is the susceptibility (transfer function of force to displacement), with the mechanical spring constant $K_m(\Omega) = m\Omega_m^2 - i\Omega\Gamma_m$, and the optical spring constant $K_o(\Omega)$ given by equation (2.15). We have approximated $\omega_0/\omega_c \approx 1$ in this step.

Next we investigate the $\widetilde{F}_{RP}$ term in equation (2.31). This term describes a

fluctuating force that is driven by the quantum noise of the optical field — in other words, a quantum radiation pressure force:

$$\widetilde{F}_{RP} = \sqrt{\frac{\hbar m \Omega_q^2}{1 + \delta^2}} \frac{(1 - i\Omega/\gamma_c)\widetilde{X}_{\text{in}} - \delta \widetilde{Y}_{\text{in}}}{(1 - i\Omega/\gamma_c)^2 + \delta^2} \tag{2.32}$$

The power spectral density of this force, $S_F^{(RP)}(\Omega)$, can be determined using our knowledge of the correlation functions of the input field a_{in}, which are

$$\langle 0|a_{\text{in}}(t)a_{\text{in}}^\dagger(t')|0\rangle = \delta_{\text{Dirac}}(t - t')$$
$$\langle 0|a_{\text{in}}^\dagger(t)a_{\text{in}}(t')|0\rangle = \langle 0|a_{\text{in}}(t)a_{\text{in}}(t')|0\rangle = \langle 0|a_{\text{in}}^\dagger(t)a_{\text{in}}^\dagger(t')|0\rangle = 0 \tag{2.33}$$

for the vacuum state $|0\rangle$. Here the Dirac delta correlation function tells us that the spectrum of the input noise is "white" (that is, uniform for all frequencies). Note that the power spectral density of an operator O is related to the correlation function via the Fourier transform, as follows:

$$\pi \delta_{\text{Dirac}}(\Omega - \Omega') S_O(\Omega) = \frac{1}{2}\langle \widetilde{O}(\Omega)\widetilde{O}^\dagger(\Omega') + \widetilde{O}^\dagger(\Omega')\widetilde{O}(\Omega)\rangle \tag{2.34}$$

Putting all of the pieces together, we find that the power spectral density of the quantum radiation pressure force is given by:

$$S_F^{(RP)}(\Omega) = \frac{\hbar m \Omega_q^2}{1 + \delta^2}\left(\frac{1 + \delta^2 + (\Omega/\gamma_c)^2}{(1 + (\delta - \Omega/\gamma_c)^2)(1 + (\delta + \Omega/\gamma_c)^2)}\right) \tag{2.35}$$

This formula is worth highlighting, even though it is a little unwieldy. It expresses the strength of the quantum back-action in an optical cavity at *any* frequency and detuning (within the limits of our approximations). If we make the "relaxed" quasistatic approximation, keeping terms up to first order in Ω/γ_c, then we find that within the cavity linewidth, the spectrum is approximately white:

$$S_F^{(RP)}(\Omega) \approx \hbar m \Omega_q^2 \left(\frac{1}{1 + \delta^2}\right)^2 \tag{2.36}$$

Radiation pressure is central to the work described in this thesis, and the expression we have just obtained for the quantum fluctuations of this force is a result that we will refer to again and again. However, radiation pressure is only half of the story of quantum noise in this system. The other half, shot noise, will be considered next.

2.3.3 Cavity output field

Shot noise comes into play when we try to gather information about the state of the cavity, by measuring the output optical field. To compute the output field, we need to use the cavity input-output relation [54]:

$$a_{\text{out}} = \sqrt{2\gamma_c}a - a_{\text{in}} \tag{2.37}$$

Applying this relation, we can find the output quadrature operators $\widetilde{X}_{\text{out}}$ and $\widetilde{Y}_{\text{out}}$. More generally, we can rotate the quadrature basis by θ, to obtain the operator for any intermediate quadrature phase: $\widetilde{Y}_\theta = \cos(\theta)\widetilde{Y}_{\text{out}} - \sin(\theta)\widetilde{X}_{\text{out}}$. We find that the mirror displacement signal $\widetilde{x}$ shows up in the output with the following structure:

$$\widetilde{Y}_\theta = C(\theta, \Omega)(\widetilde{x} + \widetilde{x}_S(\theta)) \tag{2.38}$$

Here $C(\theta, \Omega)$ is the transfer function of displacement to $\widetilde{Y}_\theta$, while $\widetilde{x}_S(\theta)$ is a noise term of optical origin, called the shot noise of $\widetilde{Y}_\theta$, calibrated in displacement units.

The exact formulas for $C(\theta, \Omega)$ and $\widetilde{x}_S(\theta)$ are rather cumbersome, so we do not reproduce them here. However, using them we can obtain the power spectral density of a shot noise limited displacement measurement, written in the "relaxed" quasistatic limit:

$$S_x^{(S)}(\theta, \Omega) \approx \frac{\hbar}{m\Omega_q^2} \left(\frac{(1 + \delta^2)^3}{(\cos\theta + \delta\sin\theta)^2} \right) \tag{2.39}$$

This result tells us two things. First, the shot noise is approximately white within the cavity linewidth; and second, to optimize the ratio of the displacement signal to the

shot noise, we should measure in a specific quadrature phase given by:

$$\theta_{\text{opt}} = \frac{\delta}{|\delta|} \arccos \frac{1}{\sqrt{1+\delta^2}} \tag{2.40}$$

After the optimization, the displacement sensitivity as limited by shot noise becomes

$$S_x^{(S)}(\theta_{\text{opt}}, \Omega) \approx \frac{\hbar}{m\Omega_q^2}(1+\delta^2)^2 \tag{2.41}$$

2.3.4 Standard Quantum Limit and beyond

Together, shot noise and radiation pressure noise determine the quantum-limited sensitivity of an opto-mechanical sensor, such as a gravitational wave interferometer.** How the two quantum noises combine depends on how they are correlated.

For the situation we have been discussing, where the input noise consists of vacuum fluctuations, and we measure $\widetilde{Y}_{\theta_{\text{opt}}}$, it can be shown that the shot noise and the radiation pressure noise are uncorrelated. So we simply add up the power spectral densities given in equations (2.36) and (2.41):

$$
\begin{aligned}
S_x(\Omega) &= |\chi(\Omega)|^2 S_F^{(RP)}(\Omega) + S_x^{(S)}(\theta_{\text{opt}}, \Omega) \\
&\approx \hbar m\Omega_q^2 |\chi(\Omega)|^2 \left(\frac{1}{1+\delta^2}\right)^2 + \frac{\hbar}{m\Omega_q^2}(1+\delta^2)^2 \\
&= \hbar|\chi(\Omega)| \left(|\mathcal{K}(\Omega)| + \frac{1}{|\mathcal{K}(\Omega)|}\right)
\end{aligned}
\tag{2.42}
$$

where $\mathcal{K}(\Omega) = m\Omega_q^2 \chi(\Omega)/(1+\delta^2)^2$ is the factor that determines the relative contribution of radiation pressure and shot noise. Apparently the noise is minimized when $|\mathcal{K}(\Omega)| = 1$, so that both contribute equally. The limiting sensitivity of this carefully optimized

---

**One might ask whether quantum fluctuations intrinsic to the *mirror* (as opposed to those of the *light*) play any role in limiting the sensitivity. The answer, for the interferometer configurations we will discuss in this thesis, is no — they do not [28]. Even the room-temperature thermal fluctuations of the mirror, which are much larger than the zero-point fluctuations, may be dominated by the light's radiation pressure if a low loss mirror suspension is used. Note that in our formalism, the quantum and thermal fluctuations of the mirror suspension are both contained in F_T. For details of the quantum Langevin treatment of these noises, see reference [53] and chapter 6.

measurement is known as the Standard Quantum Limit (SQL):

$$S_x^{(\mathrm{SQL})}(\Omega) = 2\hbar|\chi(\Omega)| \tag{2.43}$$

Note that in general, it is only possible to arrange that $|\mathcal{K}(\Omega)| = 1$ at a single frequency Ω. For example, if the cavity is at zero detuning and the mechanical spring constant is negligible, then we find that $|\mathcal{K}(\Omega)| = (\Omega_q/\Omega)^2$. So we can interpret Ω_q as the frequency at which the quantum limited sensitivity reaches the SQL in this case. At frequencies lower than Ω_q, the radiation pressure dominates the shot noise, while at higher frequencies the reverse is true.

However, the Standard Quantum Limit is not the end of the story. The limit is only valid when the optical noise is driven by vacuum fluctuations and the measurement quadrature is $\widetilde{Y}_{\theta_{\mathrm{opt}}}$. If we relax either of those assumptions, then we find that radiation pressure and shot noise can become correlated, and the SQL can in fact be surpassed.

Along these lines a variety of practical proposals exist for beating the SQL (see for example reference [76]). We will concentrate on a related scheme for engineering quantum correlations in the output optical fields, which is of special relevance for the interferometer that is the topic of this thesis.

When the quantum noise is correlated between the two quadratures X_{out} and Y_{out}, we can choose a measurement quadrature Y_θ such that the noise cancels at least partially, permitting the measured spectral density to drop below the normal shot noise level, $S_{Y_\theta}(\Omega) = 1$ (in shot noise units). Such a field is called "squeezed". Squeezed light can be used to improve the sensitivity of quantum noise limited measurements and circumvent the SQL. Note that the uncertainty relation requires that in the quadrature orthogonal to the measurement, there must be an excess of quantum noise (which is known as "anti-squeezing").

The opportunity to correlate the output quadratures opto-mechanically stems from the fact that, according to equation (2.38), the output quadrature $Y_{\theta_{\mathrm{opt}}}$ has two components, $\widetilde{x}$ and $\widetilde{x}_S(\theta_{\mathrm{opt}})$, both of which are driven by different quadratures of the input quantum noise.

41

For convenience, we will consider a cavity at zero detuning, and neglect damping and thermal noise. This causes the input-output relationship to take a particularly simple form. According to equations (2.31) and (2.32), the mirror motion $\widetilde{x}$ is driven by radiation pressure fluctuations alone — and the radiation pressure fluctuations are due only to the $\widetilde{X}_{\text{in}}$ quadrature of the input noise. Meanwhile the shot noise term $\widetilde{x}_S$ in the optimal quadrature $\widetilde{Y}_{\theta_{\text{opt}}} = \widetilde{Y}_{\text{out}}$ arises solely from the input quadrature $\widetilde{Y}_{\text{in}}$.

To sum up these input-output relations, we can write

$$
\begin{bmatrix} \widetilde{X}_{\text{out}} \\ \widetilde{Y}_{\text{out}} \end{bmatrix} = \frac{1 + i\Omega/\gamma_c}{1 - i\Omega/\gamma_c} \begin{bmatrix} 1 & 0 \\ \mathcal{K}(\Omega) & 1 \end{bmatrix} \begin{bmatrix} \widetilde{X}_{\text{in}} \\ \widetilde{Y}_{\text{in}} \end{bmatrix} \tag{2.44}
$$

Note that if radiation pressure dominates ($|\mathcal{K}(\Omega)| \gg 1$), then $\widetilde{Y}_{\text{out}}$ becomes strongly correlated with $\widetilde{X}_{\text{out}}$. And if we rotate the measurement quadrature $\widetilde{X}_{\text{out}}$ slightly so as to minimize the noise, then we find the optimal rotation angle $\theta(\Omega) \approx -1/\mathcal{K}(\Omega)$ and

$$
S_{X_{\theta(\Omega)}}(\Omega) \approx \frac{1}{|\mathcal{K}(\Omega)|^2} \tag{2.45}
$$

which confirms that the output field is indeed squeezed.

For the scenario we have just discussed, the squeezing may be inconvenient to observe and use in practice, because the low-noise quadrature may have a distinct frequency dependence. For example, if the mirror is idealized as a free mass so that $\chi(\Omega) = -(m\Omega^2)^{-2}$, then the quadrature rotates as $(\Omega/\Omega_q)^2$.

It is tempting to think of putting the movable mirror on a stiff mechanical suspension, which would allow $\chi(\Omega)$ and $\mathcal{K}(\Omega)$ to remain nearly constant below the resonant frequency Ω_m. However, such a suspension almost inevitably couples an excessive amount of thermal noise onto the mirror, overwhelming the radiation pressure and obliterating the squeezing.

This consideration led to a proposal to observe opto-mechanical squeezing with the help of an *optical spring*, to stiffen the mirror's response without adding thermal noise [40] — which, in turn, motivated the construction of the experiment we will describe in the next chapter.

Chapter 3

The apparatus

This chapter is concerned with the ponderomotive interferometer's design and its as-built configuration (as of 2012). The goal of the design is to make the mirror displacement due to radiation pressure fluctuations a dominant effect, overwhelming all other noise sources. Observation of squeezing and entanglement of light should be possible once this goal has been achieved, as discussed in chapters 2 and 6.

There were three earlier generations of this experiment in which the classical dynamics of radiation pressure were studied using a simpler optical configuration (a single cavity). Key features of the earlier setups are discussed in chapter 4, along with the results we obtained, and they are described in detail in Thomas Corbitt's thesis [41].

3.1 Opto-mechanical system

A schematic of the interferometer's opto-mechanical layout is shown in figure 3-1. The main factors that affect the radiation pressure noise level are the laser powering the interferometer, the finesse of the optical cavities, the mass of the cavity mirrors, and the resonant frequencies of their suspensions. We discuss each of these factors below.

Parameter	Symbol	Value	Unit
Laser wavelength	λ	1064	nm
Laser power	P_{in}	4	W
Laser intensity noise		10^{-8}	$1/\sqrt{\mathrm{Hz}}$
Laser frequency noise		10^{-4}	$\mathrm{Hz}/\sqrt{\mathrm{Hz}}$
Modulation frequency		25	MHz
Input mirror mass		250	gram
Input mirror resonant frequency		1	Hz
Input mirror transmission	t_I^2	800	ppm
Input mirror radius of curvature	R_I	0.55	m
End mirror reduced mass	m	0.5	gram
End mirror resonant frequency	$\Omega_m/2\pi$	10	Hz
End mirror transmission	t_E^2	10	ppm
End mirror radius of curvature	R_E	0.55	m
Loss per bounce		10	ppm
Michelson asymmetry		8.4	cm
Contrast defect	ϵ_c	1	%
Cavity length	L	1	m
Cavity finesse	$\mathcal{F}$	8000	
Cavity linewidth (HWHM)	$\gamma_c/2\pi$	10	kHz
Circulating power	P	10	kW
Beam spot radius	w	1	mm
End mirror coating thickness	d	10	μm
Parallel coating loss angle	$\phi_\parallel$	400	ppm
Perpendicular coating loss angle	$\phi_\perp$	400	ppm
Substrate Young's modulus	E_s	7.3×10^{10}	N/m^2
Coating Young's modulus	E_c	1.1×10^{11}	N/m^2
Temperature	T	300	K

Table 3.1: Summary of parameters, their symbols, and their nominal values.
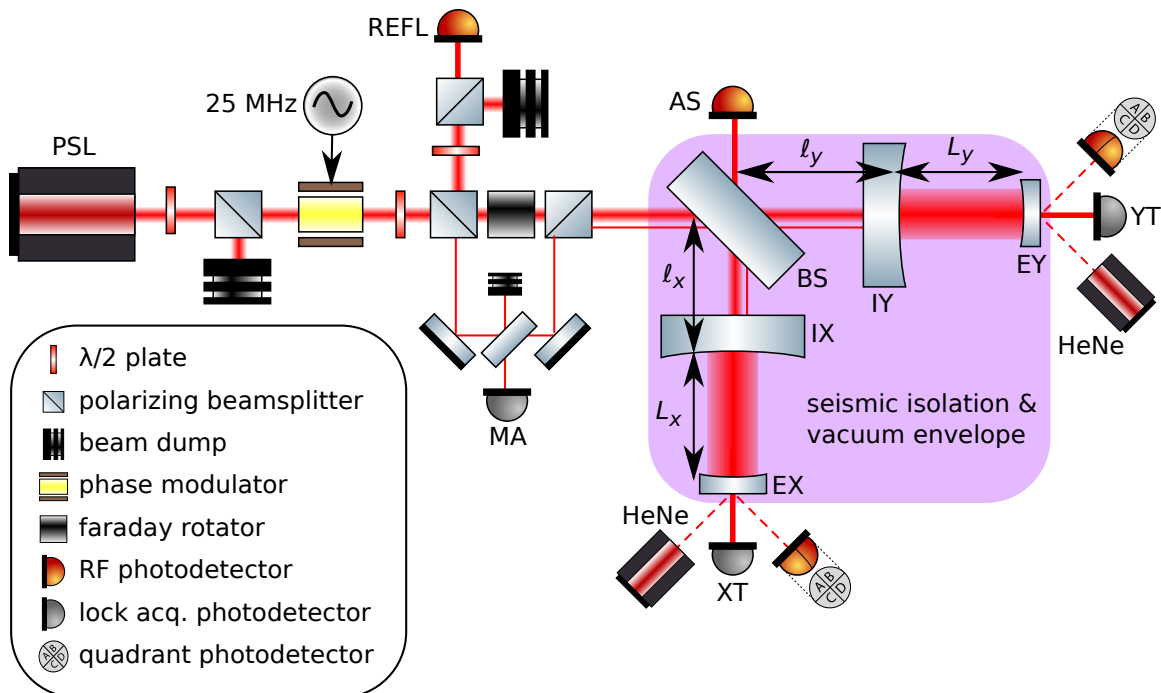
Figure 3-1: Schematic layout of the ponderomotive interferometer.

3.1.1 Laser source

To power the interferometer, we use the Pre-Stabilized Laser (PSL) source that was developed for Initial LIGO. This system is extensively documented elsewhere (see for instance [125, 5, 6]); here we briefly review the important features. Other than a custom intensity stabilization servo [121], our setup makes no significant departures from the LIGO PSL design.

The vital element is a Nd:YAG laser (Lightwave 126MOPA) that outputs continuous wave 1064 nm light. This laser contains a master oscillator that supplies about 500 mW of optical power, followed by a power amplifier that boosts the output to as much as 10 W. The master oscillator (Lightwave 126) provides a slow (temperature) and a fast (piezoelectric) frequency actuator, which we use in concert with a phase modulator (New Focus 4004) to stabilize the laser's frequency. The power amplifier stage (a sequence of diode-pumped Nd:YAG rods) includes the gain actuator [8] that we use to stabilize the laser's intensity.

The laser light is then mode-matched to a small, critically coupled cavity called the "Pre-Mode Cleaner" cavity (PMC) [141]. The PMC is designed to separate the TEM00

spatial mode, which is transmitted through the cavity when resonant, from higher order spatial modes, which do not resonate alongside the TEM00 and are reflected. Due to the cavity's 5 MHz linewidth, it also rejects frequency and intensity noise at the 25 MHz sideband frequency used by the interferometer's length sensing and control (which is discussed in section 3.2).

A small fraction of the PMC transmission beam is picked off and detected, in order to obtain an error signal for the servo that stabilizes the laser's intensity. This servo achieves a relative intensity noise of about $10^{-8}/\sqrt{\text{Hz}}$ [120].

Then another pickoff is used to stabilize the laser's frequency to the resonance of a monolithic reference cavity that is suspended inside a vacuum chamber. There is an adjustable frequency offset between the laser and the reference cavity, which is implemented using a voltage controlled oscillator (Synergy Microwave CRO-P-AO3) that drives an acousto-optic modulator (Isomet 1205C-843). This arrangement provides a fast frequency actuator that is crucial for controlling the interferometer (see section 3.2.2). However, the VCO's phase noise limits the frequency stability of the PSL to about 10^{-2} Hz/$\sqrt{\text{Hz}}$.

Finally, the 25 MHz sidebands are applied by a phase modulator (New Focus 4004), before the beam is mode-matched and steered into the interferometer.

3.1.2   Optical configuration

The ponderomotive interferometer's configuration unites the features of two simpler optical designs. First, each input mirror–end mirror pair forms an optical cavity (or Fabry-Perot interferometer). Second, the beamsplitter and the input mirrors together form a Michelson interferometer. The combined configuration is referred to as a Fabry-Perot Michelson interferometer (FPMI).

The purpose of the Michelson interferometer is to reject the noise of the laser. Even after the stabilization we apply to the laser source, its technical noise remains far in excess of the shot noise level. But the laser light together with the excess noise it bears is made to destructively interfere at the Michelson's antisymmetric port.
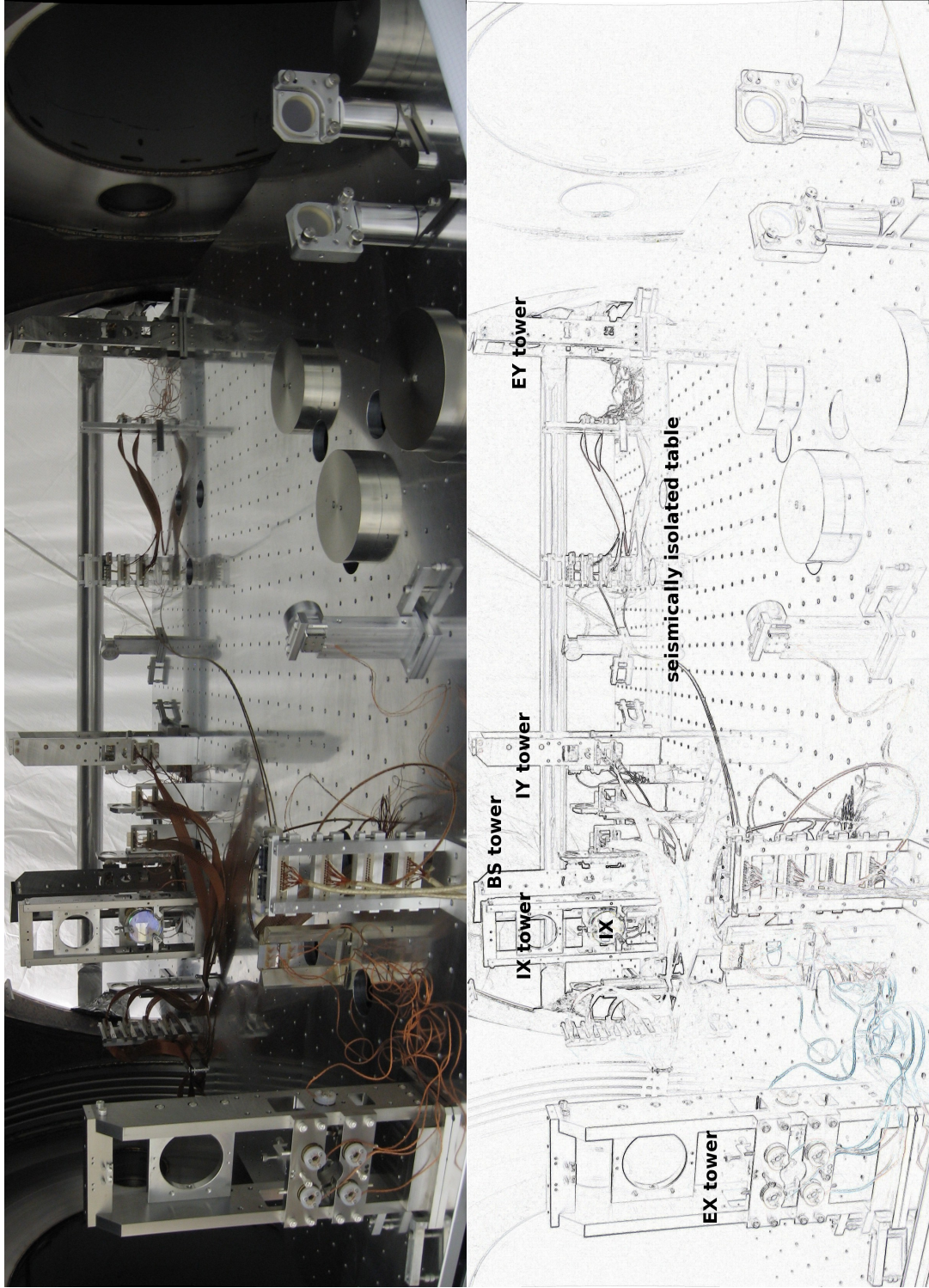
Figure 3-2: Panoramic view of the in-vacuum apparatus. The five suspension towers can be seen, along with one of the suspended optics.

The labels visible in the figure: EY tower, seismically isolated table, IY tower, BS tower, IX tower, IX, EX tower.

The available cancellation is limited by the so-called contrast defect, defined as $\epsilon_c = P_{AS}/P_{\text{in}}$, where P_{AS} is the power exiting the antisymmetric port on a dark fringe, and P_{in} is the power incident on the beamsplitter (excluding, in both cases, any power in the 25 MHz sidebands).

The typical value of ϵ_c that we obtain is better than 1%. This defect is highly sensitive to the positioning of the mode-matching lenses in each arm. With the lens positions optimized, much of the remaining defect is attributable to the nonuniform spatial distribution of losses on the cavity mirrors.

The cavities are designed to be over-coupled: that is, the input mirror transmission greatly exceeds both the end mirror transmission, and the absorption and scattering losses. As a result, most of the optical power that enters the cavity ultimately exits back through the input mirror. To the Michelson interferometer, each cavity essentially looks like a somewhat lossy mirror — with the important exception that the cavity treats the 25 MHz sidebands differently from the carrier field. (The sidebands are discussed further in section 3.2.)

Optical cavities are used in order to magnify the effect of radiation pressure. On resonance, the optical power incident on the cavity's mirrors is multiplied by a factor of $2\mathcal{F}/\pi$ over the input power. (This factor is about 5000 for our cavities.) The quantum radiation pressure fluctuations are multiplied by the same factor.

Recall from equation (2.36) that the back-action power spectrum is proportional to the square of the "quantum frequency" Ω_q. This fact implies that the spectrum scales with the cavity finesse more favorably than it scales with the input power (quadratic vs. linear). Physically, this difference arises because improving the cavity finesse permits each photon to *coherently* interact with the mirrors a greater number of times. It is analogous to shrinking the laser wavelength and thus increasing the momentum imparted by each photon, while leaving the number of photons unchanged. On the other hand, cranking up the input power increases the number of independent photons, whose radiation pressure noise adds *incoherently*.

Thus, from an input laser power of 4 W, the mirrors experience radiation pressure noise as large as a 100 MW laser would impart, if unassisted by cavities.

The technical limit for our two-mirror cavities, as set by typical intra-cavity losses of 10 ppm per bounce, is a finesse of about 300000. In order to remain in the over-coupled regime that lets us efficiently extract the squeezing or entanglement generated in the cavity, we must keep the finesse well below this limit. The designed cavity finesse of 8000 was in fact chosen rather conservatively, and could be increased in a future iteration of this experiment.

The geometry of each cavity, specified by its length L and the radii of curvature of its mirrors R_I and R_E, must satisfy several constraints. For example, the spatial mode should be stable, which requires the so-called g-factor, defined as $g = g_I g_E = (1 - L/R_I)(1 - L/R_E)$, to fall within the range $0 \leq g \leq 1$. The value of g is tuned to avoid degeneracy between the TEM00 mode and higher order modes.

Whenever large radiation pressure forces are developed in a suspended mirror cavity, the Sidles-Sigg angular instability [129] is another consideration that constrains the cavity geometry. In short, radiation pressure can exert not just a longitudinal force on each cavity mirror, but also a torque. The magnitude and sign of the torque depends on the beam spot position on the mirror, which in turn depends on the alignment of the cavity. When a mirror becomes misaligned, this torque may tend either to correct the alignment, or to deflect the mirror further. As the circulating power increases, the radiation pressure torques also grow. Sidles and Sigg showed that these torques eventually overwhelm the restoring torque of the mirror suspension, and act to destabilize the system.

However, the power level at which the instability occurs depends on the cavity geometry. In particular, it is advantageous to choose g_I and g_E both to be negative (that is, $R_I < L$ and $R_E < L$), in order to reduce the magnitude of the instability.

In addition, the cavity geometry determines the spatial extent of the cavity mode. For a symmetric cavity ($R_I = R_E$), the radius* w of the beam spot on the mirrors is given by $w^2 = \lambda L/(\pi \sqrt{1-g})$. The size of the beam spot is significant for two reasons:

- There is rumored to be a threshold optical power density of about 1 MW/cm^2, above which the mirror coatings may sustain damage. Accordingly, for our

---

*A Gaussian beam's radius extends to the $1/e$ point in the field amplitude.

cavities with up to 10 kW of circulating power, the beam radius at the mirror should be larger than about 0.5 mm.

- Larger beams pick up less of the thermal noise of the mirror coatings, because they perform spatial averaging over a larger area of the mirror's surface (see section 3.4).

To make the beam spot size at the mirrors sufficiently large, we use a nearly concentric geometry with $g_I \approx g_E \approx 1$.

Finally, increasing the cavity length not only helps to achieve a larger beam spot size, it also narrows the cavity linewidth, which reduces the optical anti-damping forces that give rise to parametric instabilities of the mirrors' acoustic modes (see chapter 2). The dimensions of our optical table limit the cavity length to $L \sim 1$ m.

3.1.3   Mirrors and suspensions

The 1 gram end mirror of each optical cavity is responsible for converting the radiation pressure force developed in the interferometer to an observable displacement. Thus the design of this mirror and its suspension is of great importance.

The mass of the end mirror should be kept as low as possible, in order to optimize the displacement per force. However:

- The surface area of the mirror has a lower bound, imposed by the need to limit diffraction losses of the light in the cavity mode. [†]

- There is also a constraint on the mirror thickness. As the mirror is made thinner, the resonant frequencies of its acoustic modes fall, causing them to be subjected to stronger optical anti-damping forces which eventually give rise to parametric instabilities (see chapter 2).

[†]A quick estimate of the diffraction losses can be made by approximating the beam profile as an ideal Gaussian: then the fractional power lost due to clipping at radius r is given by e^{-2r^2/w^2}. Such an estimate suggests that these losses are negligible in our experiment, as long as the beam remains centered on the mirror within a few mm.
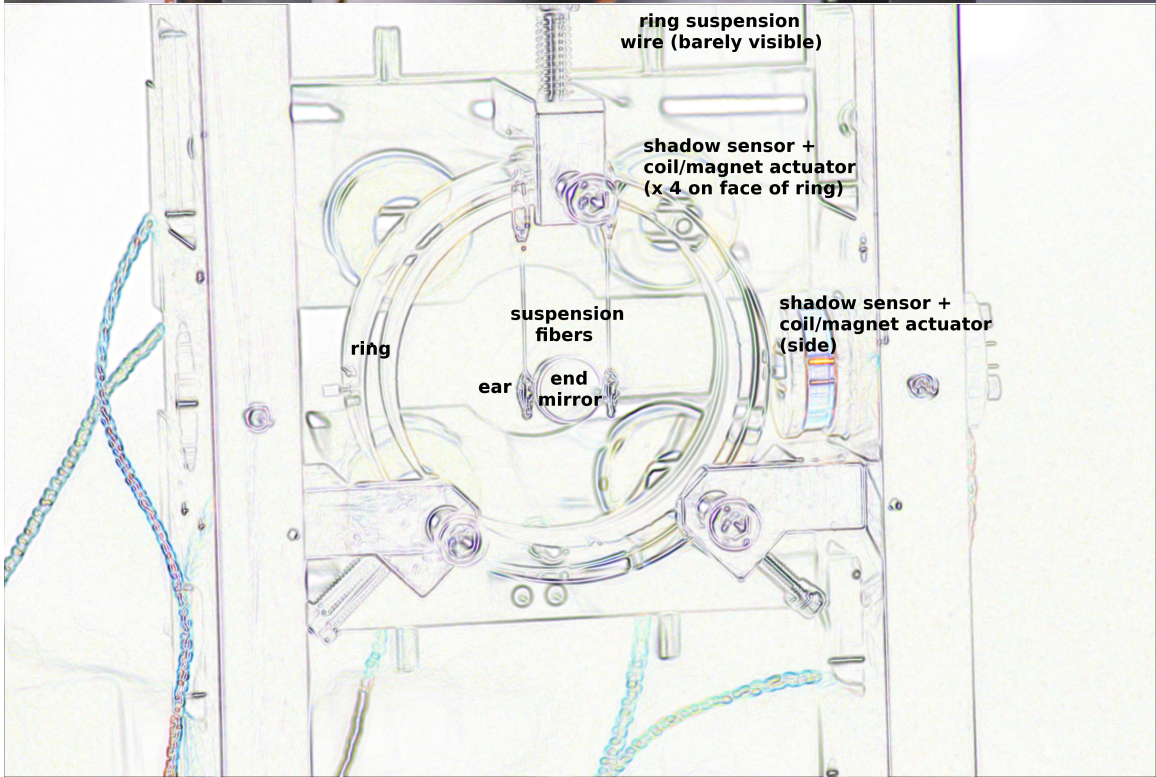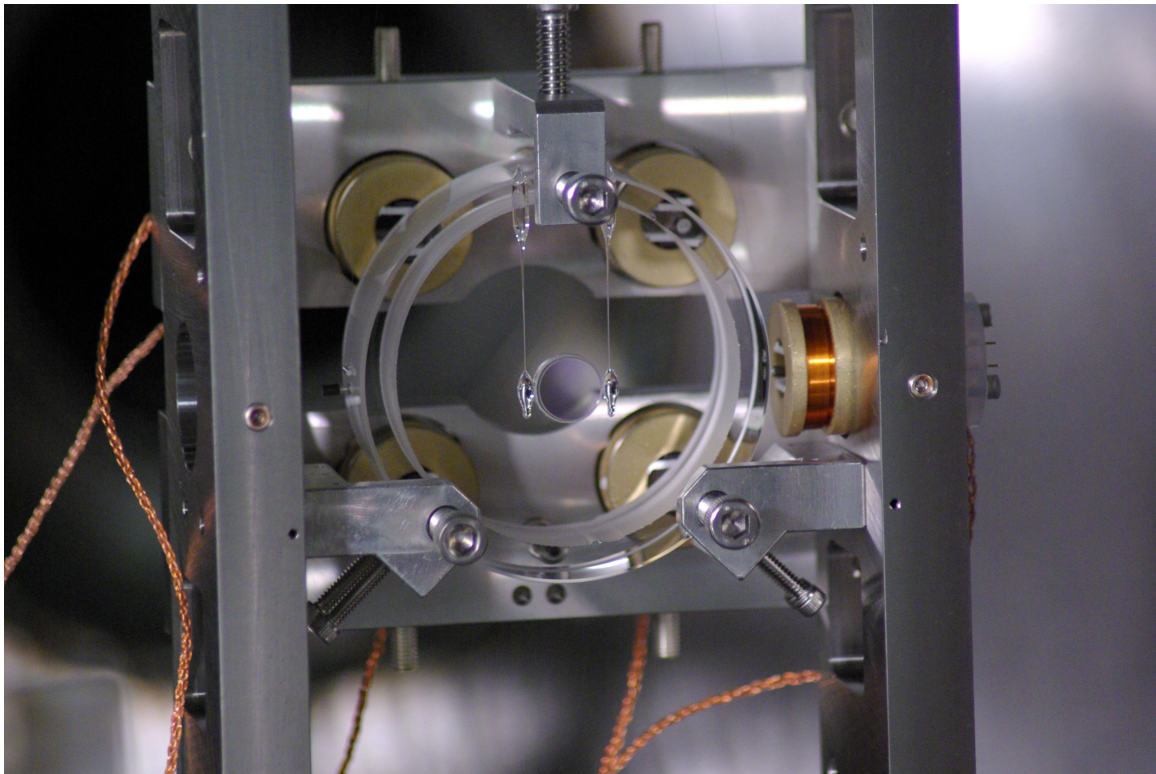
Figure 3-3: The 1 gram end mirror and its suspension.

Ultimately, the selection of a gram-scale mirror mass was driven by practical considerations. Smaller would have been better, but this scale is close to the smallest that can be accommodated using the handling techniques and suspension technologies developed for gravitational wave interferometers.

The LIGO Small Optic Suspension (SOS) [69] is used for the top stage of the end mirror suspension. It is also the sole stage used for suspending the input mirrors and the beamsplitter (which have a mass of 250 grams). This suspension includes a set of shadow sensors used to monitor the optic's motion, a set of magnet-coil actuators used to control the optic, and it serves to decouple the optic from motion of the table at frequencies above its 1 Hz resonance.

The bottom stage of the end mirror suspension consists of a fused silica ring (of the same dimensions as a 250 gram optic), and two specially tapered fused silica fibers that support the 1 gram mirror (see figure 3-3). This suspension is designed to minimize the amount of thermal noise that couples to the mirror.

In order to minimize the suspension's thermal noise, it should be made as tenuous as possible. Here a constraint arises due to the need to control the mirror's pitch angle using the coil-magnet actuators located on the ring. If the fibers were to be made so floppy that the restoring force due to their elasticity became negligible, then the mirror would always hang straight down under gravity, like a pendulum, no matter how the ring was oriented.

The resonances of the seismic stack supporting the optics table impose an even more stringent constraint. We prefer not to allow the suspension resonances to overlap with those of the stack: such a coincidence would amplify the effect of ground motion. Numerous stack resonances occur at frequencies ranging up to 7 Hz, which led us to set the fundamental mode frequency of the end mirror suspension to 10 Hz.

The fiber's tapering profile was tailored to maximize the mechanical quality factor of the 10 Hz mode. The losses in the structure were expected to be dominated by the ring/fiber joint and the fiber/mirror joint, because these joints were made of a Vac-Seal (Tra-Con), a lossy epoxy adhesive. By including a stiff "rod" element at the top of the fiber where it meets the ring, and a stiff "ear" at the bottom where it

contacts the mirror, we can ensure that almost all of the energy of the 10 Hz mode goes into bending the slender central section of the fiber, which is pristine, while the portion in contact with the lossy adhesive scarcely moves.

This suspension design was successful in achieving a very high quality factor of more than 10^6 for the 10 Hz mode (see chapter 5). The thermal noise of this mode, considered by itself, is far better than is required to observe radiation pressure. However, the off-resonant thermal noise of other modes of the structure, particularly the modes involving the "ears", remains a challenge. The ear mode issue is being addressed by new mirror and suspension designs that increase the stiffness of the ear-mirror bond. This topic is discussed further in chapter 5.

3.2 Length sensing and control

As the interferometer mirrors move in response to radiation pressure fluctuations, ground motion, or other applied forces, the two arm cavity lengths change. A length sensing and control (LSC) system is responsible for reading out the cavity and Michelson displacements, and for applying feedback forces to the mirrors to hold them in place. The procedure for taking the interferometer from the initial uncontrolled state, to the operating state where all mirrors are under active control to "lock" it on resonance, is discussed in section 3.2.3 below. For the moment, we will assume this procedure has already been carried out successfully.

What is the fate of the 10 W of optical power that enters the interferometer when locked? To reject excess light and noise at the antisymmetric port, the Michelson is locked with the antisymmetric port dark and the symmetric port at a bright fringe: roughly 90% of the power incident on the beamsplitter is ultimately reflected back toward the laser from the symmetric port. Much of the rest exits via the antisymmetric port. A small part of the remainder is transmitted out the end of either cavity, and the rest is consumed by losses inside the interferometer.

A small fraction of the input power is in the sidebands. But after entering the interferometer, the sideband content of the light is designed to vary greatly from place

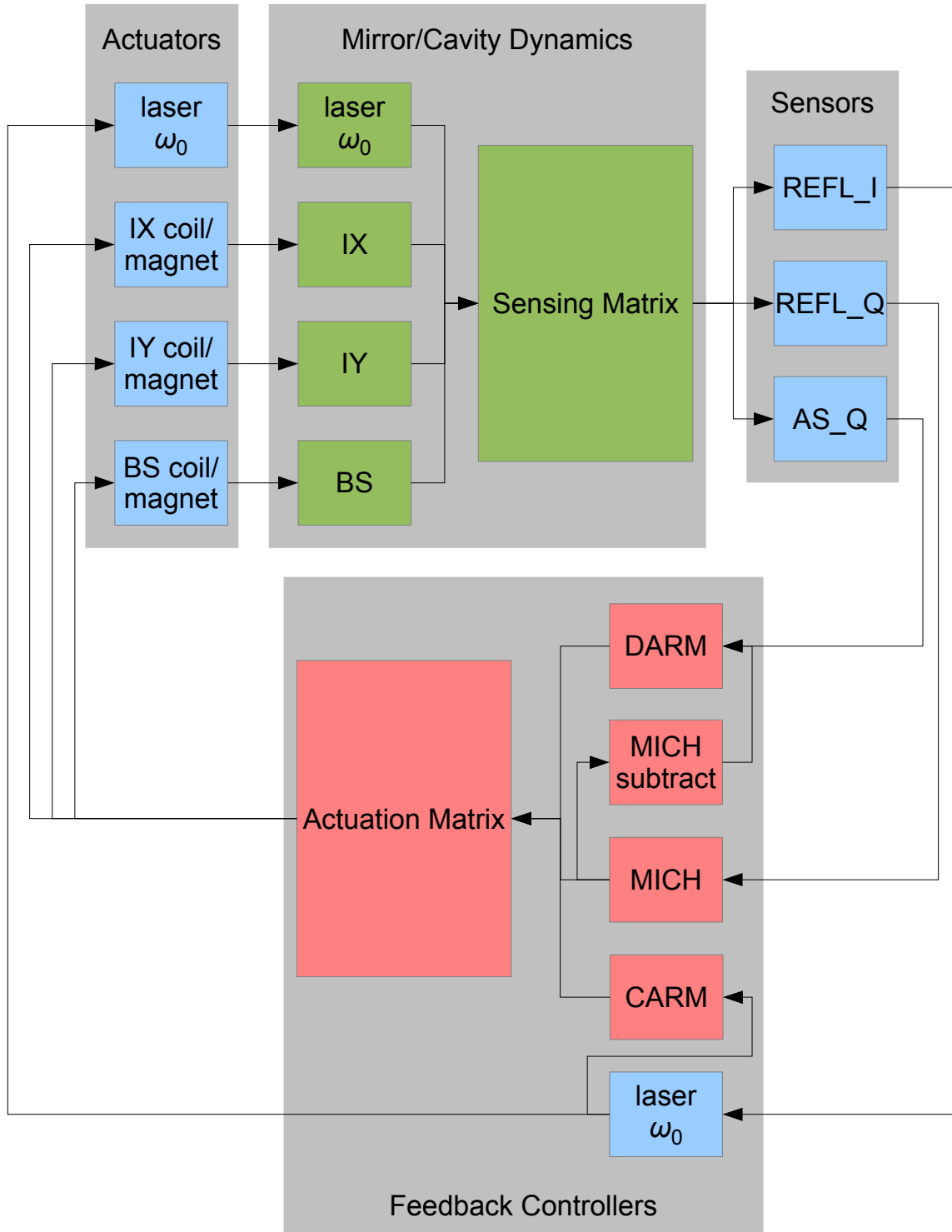**Figure 3-4:** Block diagram of the length sensing and control system. Blocks representing physical dynamics are tinted green, blocks representing analog electronics are tinted blue, and blocks representing digital computations are tinted red. Abbreviations are defined in figure 3-1 and the text of section 3.2.1. Several narrowband damping loops for individual modes of the mirrors and their suspensions are not shown.

to place. This dispersion is what lets us obtain the signals needed to read out the cavity and Michelson displacements.

3.2.1 Readout

To read out the cavities, we use the Pound-Drever-Hall (PDH) technique [46]. The 25 MHz modulation frequency is chosen such that the sidebands cannot enter the cavity to resonate alongside the carrier. As we saw in chapter 2, the carrier emerges from the cavity with a phase shift that depends sharply on the cavity length; however, the phase of the sidebands remains unaffected. The phase shift between carrier and sidebands converts some of the incident phase modulation into amplitude modulation, which shows up on our photodetector.

For the Michelson, we use the Schnupp modulation technique [127, 133]. The Michelson was designed with a macroscopic (8.4 cm) asymmetry in the position of the two input mirrors, which results in a frequency response. That is, when the symmetric port is at a bright fringe of the carrier, it is not at a bright fringe of the sidebands. A displacement from the carrier's bright fringe moves one sideband closer to its bright fringe, while the other sideband is shifted farther away, which again converts the phase modulation into a detectable amplitude modulation signal.

The light that returns from the symmetric port is separated from the inbound beam using a Faraday isolator, and most of it is dumped, while a small amount is sensed on a photodetector [13]. This detector's output is demodulated at 25 MHz to recover the amplitude-modulated signals. A numerical computation [48] of the coupling of mirror motion to the demodulated photodetector output is shown in figure 3-5. One quadrature (called REFL_I) is used to read out the common mode of cavity motion, $L_x + L_y$, which is referred to as CARM (short for *common arm*). The other quadrature (REFL_Q) can be used to read out the Michelson's displacement, $l_x - l_y$, referred to as MICH.

At the antisymmetric port, a small amount of light is picked off and sensed by another photodetector, and the resulting signal demodulated to yield a signal (AS_Q) for the differential mode of cavity motion, $L_x - L_y$, referred to as DARM (see figure 3-6).
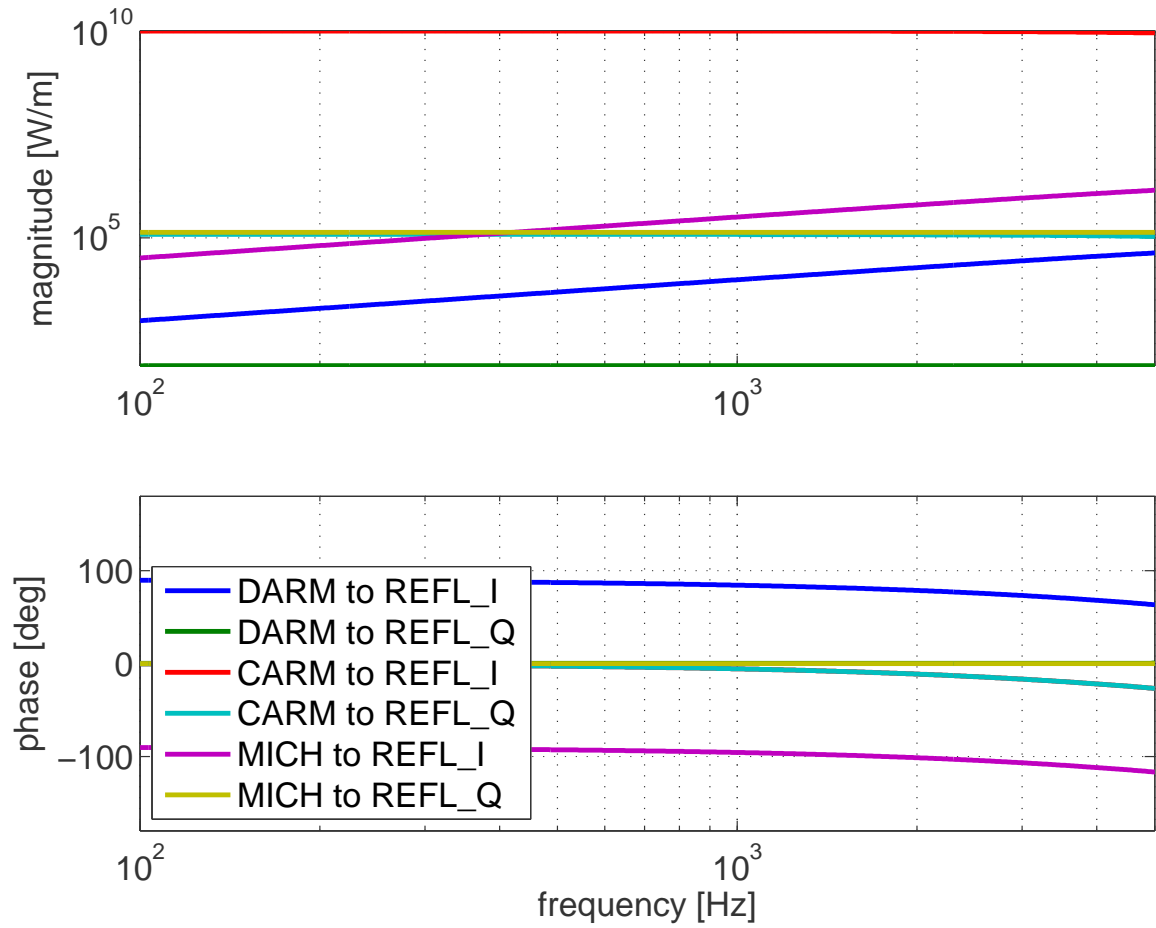
Figure 3-5: Sensing matrix elements for the demodulated signals at the symmetric port.
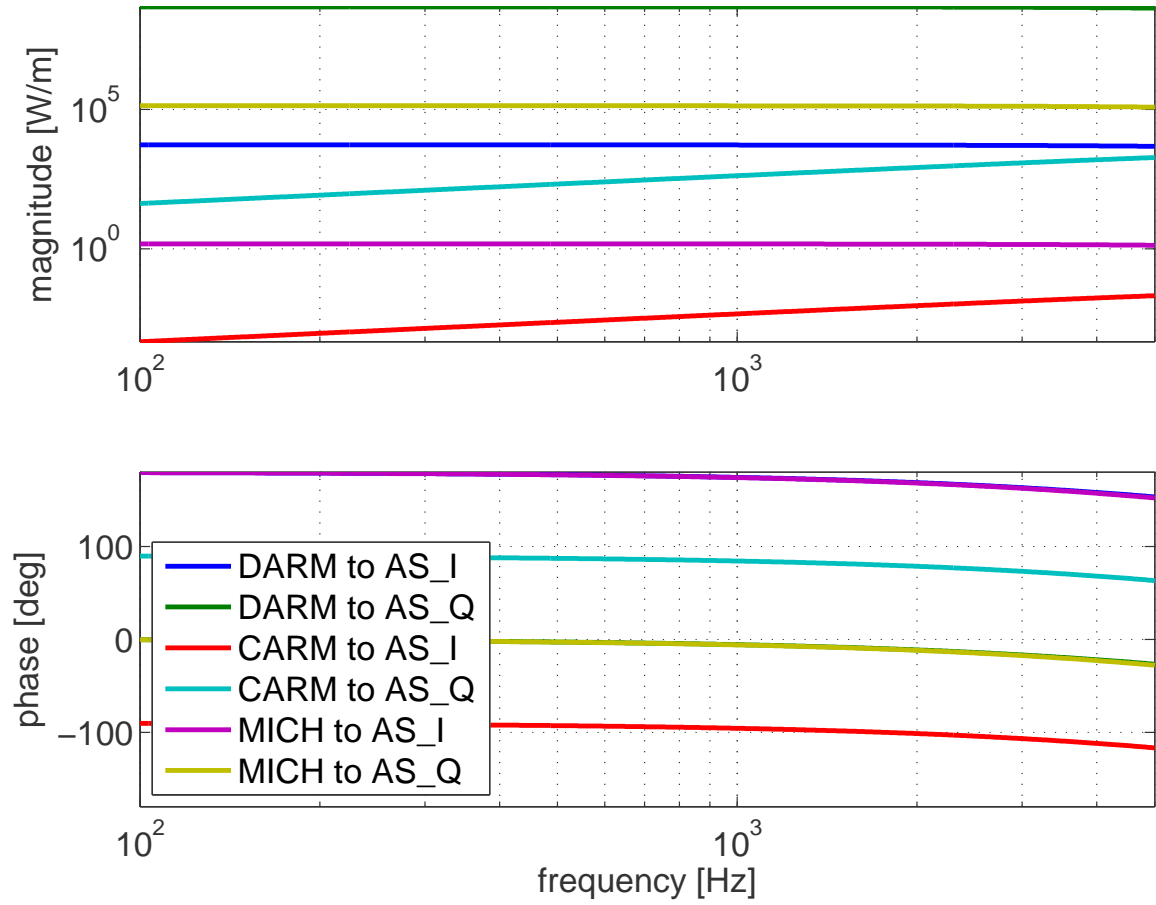
Figure 3-6: Sensing matrix elements for the demodulated signals at the antisymmetric port.

This is the readout that is designed to be the best isolated from laser noise, and the most sensitive to quantum radiation pressure fluctuations.

3.2.2 Feedback

The design of the feedback controls is motivated by the noise sources and opto-mechanical dynamics that affect each degree of freedom:

- Ground motion rattles every suspended optic, and requires all servos to push back on the optics (via the coil-magnet actuators) with a lot of gain at low frequencies (below 10 Hz or so). We tailor the servos with digital filters at these frequencies in order to accommodate features in the plant, such as suspension and stack resonances.

- The cavities, when detuned, give rise to stiff (~ 1 kHz), unstable optical springs. The CARM and DARM cavity servos require bandwidths of 1 kHz or greater in order to provide the active control needed to stabilize the system. The MICH servo does not experience these dynamics and can get by with a low unity gain frequency (UGF) of typically 100 Hz or so.

- Laser frequency noise is broadband and is sensed by the CARM readout. CARM needs to actuate the laser frequency with high bandwidth in order to suppress this noise. At low frequencies, seismically driven displacement noise dominates over the frequency noise, and CARM should actuate the optics' position to avoid imprinting seismic noise onto the laser. CARM is therefore split between two feedback paths: a slow path to the optics via the digital control system, and a fast path to the laser, which is all-analog in order to minimize delay. The total bandwidth is typically 20 kHz or greater, with the crossover frequency set at a few hundred Hz.

The digital control system is a prototype of the system designed for Advanced LIGO. It samples 64 inputs and synthesizes 32 outputs, with 16 bit resolution at a 65536 Hz sample rate. Arbitrary computations can be performed on the signals,

limited only by the 15 μs/sample execution time. The code is parallelized across four cores of the system's CPU (Intel Xeon W5590). Standard signal processing techniques for whitening, anti-aliasing, and noise shaping are used to minimize the effect of noise introduced in the analog-digital-analog conversion process.

Most of the length actuation is assigned to the input mirrors and the beam-splitter. The end mirrors have little actuation range above the 10 Hz mode of the bottom suspension stage, and so they receive only narrowband feedback to damp their resonances.

In this readout and actuation scheme, a cross-coupling exists between the DARM and MICH servos:

- When the DARM servo actuates the input mirrors to control $L_x - L_y$, it changes $l_x - l_y$ also. So DARM must actuate the beamsplitter as well, in order to cancel its effect on MICH.

- The residual noise in MICH is also weakly sensed by the DARM readout at the antisymmetric port (see figure 3-6). So when MICH is limited by sensing noise (which is true across most of our measurement band), this noise can be imprinted onto DARM as well. It is removed by digitally subtracting the MICH component from the DARM signal.

Parametric instability causes a 27.5 kHz drumhead mode of the input mirrors to ring up when the cavities are detuned. This mode is sensed by detecting the cavity transmitted light, and suppressed by a narrowband digital damping loop that actuates the mirror.

To control the unstable optical spring, our strategy is to apply a digital filter in DARM that essentially undoes the spring's effect on the open loop transfer function. This filter boosts the loop gain at low frequencies — where the optical spring suppresses the action of the servo — in order to avoid undesired unity gain crossings. Around the optical spring frequency, the filter incorporates a notch that flattens out the resonance. To keep the loop stable when the cavity detuning is reduced and the optical spring frequency falls, the notch can be filled in by engaging a resonant gain filter, which

simulates the optical spring resonance.

As the detuning or input power changes, the gains of the DARM, CARM, and MICH readouts also change, and the loop gains must be adjusted to compensate. The gain error is determined by injecting a small modulation into the loop, and measuring its open loop transfer coefficient. The result is fed back to the digital gain control by a slow (sub-1 Hz bandwidth) *UGF servo*, so as to maintain the loop gain of the underlying length servo.

The UGF servo modulations may also be used to automatically remove undesired DC offsets in the readouts. The offset in the CARM and DARM servos is found by measuring the transfer coefficient of a laser frequency modulation (used to maintain the UGF of CARM) to the cavities' transmission monitors. A pair of *offset servos* act to minimize these coefficients, in order to maintain the cavities at zero detuning. Similarly, a MICH offset servo ensures the antisymmetric port is held precisely at a dark fringe, by minimizing the transfer coefficient of the MICH UGF modulation to a photodetector at the antisymmetric port.

3.2.3 Lock acquisition procedure

When uncontrolled, the suspended optics have an RMS displacement that is typically a few microns (dominated by seismic noise), with a typical velocity of a few microns per second.

If not dealt with, this amount of random motion would render the interferometer useless. It spans several Michelson fringes, and it vastly exceeds the linear range of the arm cavity length signals, which provide an intelligible readout only when the cavity mirrors are localized within about 0.1 nm of the resonance.

To lock the interferometer, the uncontrolled motion must be counteracted during the time when the mirrors happen to swing through the resonance, while the motion can be sensed. A typical opportunity for locking lasts only a few tens of microseconds.

The large bandwidth of the laser frequency actuator can be used to good effect in locking the first cavity. However, it has a much more limited utility in locking the second cavity. A frequency deviation made to accommodate the second cavity will

simultaneously pull the first cavity off resonance, which may unlock it.

The input mirror's coil-magnet actuators are marginally adequate to the task of locking the cavity. The maximum force they can apply is 25 mN [13], so they can do at most 2.5 pJ of work on the mirror while it swings through the resonance. Thus they could remove kinetic energy corresponding to a velocity of about 4.5 microns per second for the 250 gram mirror.

However, to attenuate the noise of the coil driver electronics, we have had to use only 10% of the maximum range, and so the tolerable velocity is reduced to about 1.5 microns per second. To satisfy this restriction requires aggressive local damping and active seismic isolation (see sections 3.3.2 and 3.3.3).

We can also get a little help from radiation pressure. When the mirrors swing through resonance in such a way that the cavity length is contracting, radiation pressure acts as a restoring force. At the full input power $P_{in} \approx 4$ W, the maximum circulating power P is about 10 kW, corresponding to a force $F_{RP} = 2P/c \approx 0.1$ mN. This force, while tiny, is applied directly to the 1 gram end mirror — where, compared to the 250 gram input mirror's actuators, it is 250 times more effective. It would correspond to a velocity of more than 5 microns per second.

The actual radiation pressure force the end mirror experiences during locking is smaller than this. For one thing, light cannot fully build up in the cavity in the tens of microseconds it takes the mirrors to cross a fringe (the build-up happens on a timescale set by the cavity HWHM linewidth $\gamma_c/2\pi \approx 10$ kHz). In addition, the applied force deflects the end mirror, changing its pointing and misaligning the cavity. The misalignment can be corrected by an alignment servo (see section 3.3.1), but not on the timescale needed for lock acquisition. Therefore, we have to lock the cavities with low input power (circa 120 mW), so that the radiation pressure forces are unimportant, and slowly raise the power later.

None of the demodulated readouts at the symmetric and antisymmetric ports give usable signals unless *both* the Michelson and the cavities are near the designed operating point. We do not use these readouts for lock acquisition, because it is simpler to use other, less sensitive readouts that respond to only one degree of freedom.

For the cavities, we use the cavity transmission monitors, which do not sense the Michelson. For the Michelson, we inject and monitor an auxiliary input beam, which is misaligned so that it cannot enter the cavities.

First we lock both cavities at one linewidth detuning: that is, the point where the transmission reaches half of its value at zero detuning. A 900 Hz optical spring is present at this detuning. Then we lock the Michelson, and reduce the detuning until the transmission reaches the 90% level. At this point we hand off the DARM and CARM servos to the PDH readouts, and turn on a filter to simulate the presence of the optical spring. After the cavities have reached zero detuning, we hand off MICH, and start to raise the input power.

The lock acquisition procedure is fully scripted and automatic. After a lock loss, the interferometer reacquires lock and reaches zero detuning typically within 2–3 minutes.

3.2.4 Calibration

Length signals can be calibrated against the known wavelength of the laser. In particular, half a wavelength is the displacement the mirrors undergo between two adjacent Michelson dark fringes. This fact allows us to calibrate the Michelson readout, by observing its response as the mirrors swing freely through several adjacent fringes. Then we use this calibrated readout to measure the strength of the input mirrors' force actuators. Finally, by applying a known force to the input mirrors, we can calibrate the arm cavity readouts as well.

In the initial stages of this experiment, which involved a single cavity without a Michelson, we used a different approach: we calibrated the tuning input of the PSL's VCO using a spectrum analyzer. Then we could shift the laser wavelength by a known amount, and observe the response in the cavity readout.

Both of these techniques are commonly used to calibrate gravitational wave interferometers, and further details can be found elsewhere [61].

3.3 Other degrees of freedom

3.3.1 Alignment

The alignment of each cavity's axis to that of the input beam is automatically optimized by dithering both of its mirrors in pitch and in yaw, at four distinct frequencies in all, and monitoring the cavity transmitted light. When the cavity is well aligned, the light it transmits is maximized, and so an alignment modulation doesn't affect the transmission, to first order. Otherwise, the modulation shows up in the transmission with a linear coupling, whose slope depends on the magnitude and direction of the misalignment. We measure this slope by demodulating the transmission signal at each of the four frequencies.

At each frequency, the transmission responds to misalignments of either mirror. So each demodulated signal is fed back to both mirrors, with the appropriate coefficients in order to diagonalize the system. The diagonalization lets us achieve greater than 1 Hz bandwidth for all the alignment servos. We cannot obtain an alignment signal with much higher bandwidth without saturating the mirrors' magnet-coil actuators. (That limitation could be lifted, however, by dithering the alignment of the input beam instead. Wavefront sensing could also be used [90].)

The location of the beam spot on each optic is monitored in much the same way as the cavity alignment, by measuring the slope of the linear coupling between the alignment dither and the cavity length. At present there is no active control of these degrees of freedom.

3.3.2 Local damping

Each suspended optic is sensed in four degrees of freedom (longitudinal, pitch, yaw, and side-to-side motion) by shadow sensors attached to the suspension towers. These signals are filtered and fed back to the coils to damp the optics, reducing their RMS motion. The bandwidth of these loops is kept low and the gain is rolled off steeply in order to eradicate the sensing noise of these loops in the measurement band. The

two remaining bulk degrees of freedom (bounce and roll) do not couple to the optical field's phase or alignment to first order, and they are left uncontrolled.

Unfortunately, the shadow sensors are not very sensitive to the modes of the bottom stage of the end mirror suspension. The ring is far more massive than the 1 gram mirror, and so it reacts only weakly to the mirror's motion. Instead, we sense these modes directly using an optical lever: a HeNe laser beam that reflects from the mirror surface and is monitored on a quadrant photodetector. The HeNe beam position signal is then fed back to damp the end mirror.

3.3.3   Seismic isolation

The optics are decoupled from ground motion through several stages of isolation. The Small Optic Suspension gives a $1/f^2$ reduction in motion above its resonant frequency of 1 Hz. The table on which the suspensions reside is supported by a 3-layer seismic isolation stack of masses and springs, with numerous resonances in the 1–10 Hz band. The entire assembly rests on an actively stabilized platform called the Hydraulic External Pre-Isolator (HEPI) [7].

The HEPI senses motion of its platform in all 6 degrees of freedom using inductive position sensors and accelerometers that ride on the platform, together with a seismometer on the ground. The two tilt degrees of freedom are responsible for most of the optics' motion, as seen by the shadow sensors.

Since the suppression of this motion was being limited by the noise of HEPI's sensors, we implemented a feedback of the shadow sensor signals to the HEPI platform. After setting up this extra feedback path, and optimizing the transfer function for seismometer feedforward, the coupling of ground motion was reduced by a factor of 10 to 100. Ground motion was once a serious obstacle to locking the interferometer during the day, when "anthropogenic noise" (that is, human activity) is at its peak, but now its effect is usually manageable.
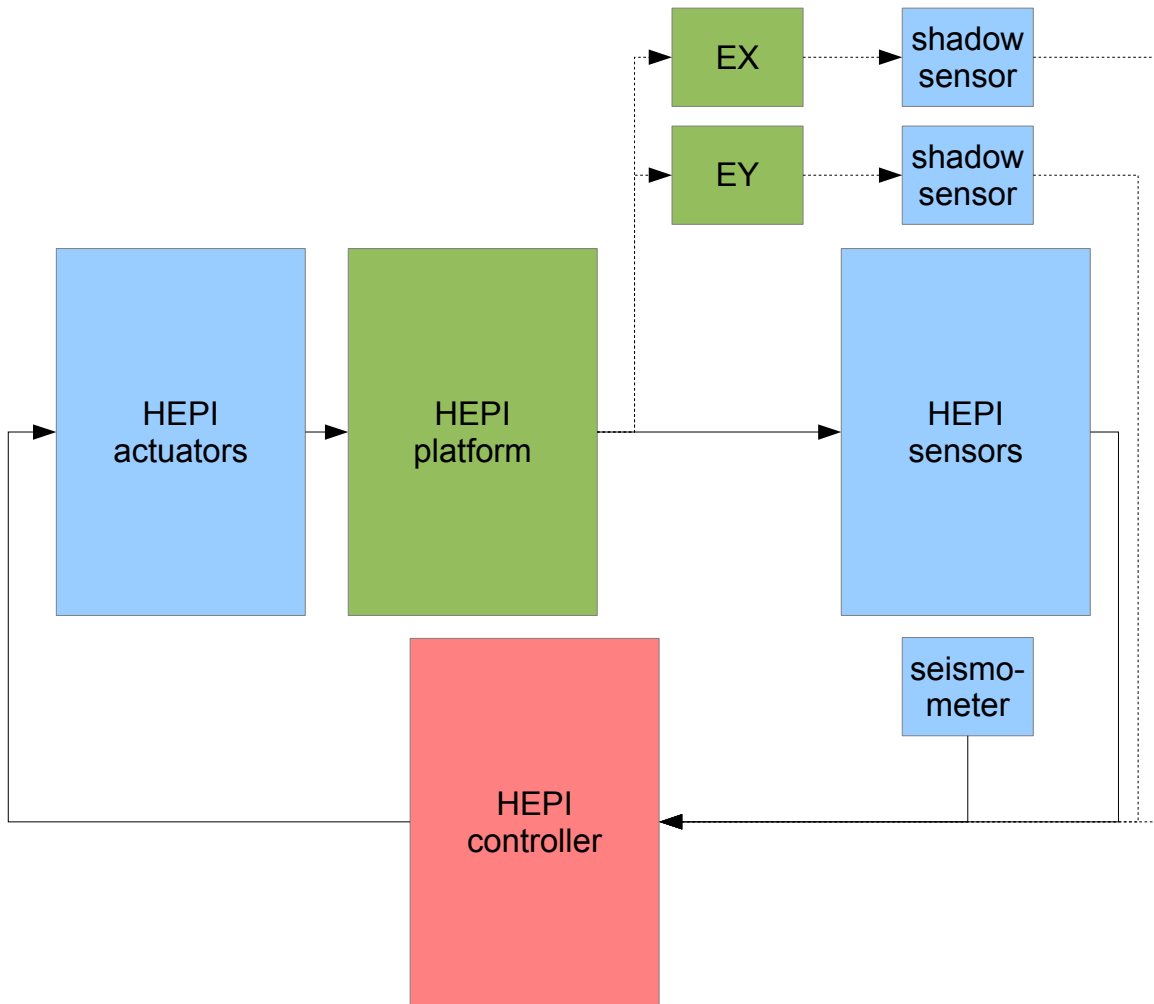
Figure 3-7: Block diagram of the HEPI active seismic isolation platform. Several of the HEPI sensors measure a combination of platform motion and ground motion; the latter is subtracted off using the signal from a nearby seismometer. Dashed lines indicate the feedback paths added to enhance the isolation.

3.3.4 Vacuum envelope

The passive seismic isolation stack and all the optics it supports are housed within a LIGO HAM (Horizontal Access Module) vacuum chamber. This chamber is part of the LASTI (LIGO Advanced Systems Test Interferometer) facility at MIT. The vacuum system is maintained at a pressure near 10^{-7} torr by a turbomolecular pump, which is sufficient to limit air damping, acoustic coupling, and residual gas phase noise to a negligible level.

The HAM chamber is made of 304L stainless steel, which was heat treated to reduce outgassing. During this treatment, it acquired a coating of loosely bound oxide particles, which serves to reduce the backscattering of stray light from the chamber walls, but also has been found to produce a rain of particles that contaminate the optics.

To catch some of these particles, we draped a thin metal canopy over the suspension towers of the cavity optics. We also unmounted a noisy diaphragm pump from the exterior, to avoid vibrating more particles loose. We reduced the existing contamination to tolerable levels through drag wiping with methanol (Sigma-Aldrich spectrophotometric grade), and a polymer cleaning solution (Photonic Cleaning Technologies First Contact).

3.4 Noise status

To conclude this chapter, we present a displacement noise plot (figure 3-8) that summarizes our understanding of the thermal noise terms that contribute the differential mode measurement.

In this plot, the quantum noise curve has been computed numerically for a 4 W input power, using a model that takes into account the known imperfections and losses of the interferometer [48]. This curve — which defines the sensitivity goal for the experiment — is mostly swamped by suspension thermal noise, but approaches within a factor of 3 near 200 Hz.

The power spectral density of thermal displacement noise arising in the coating
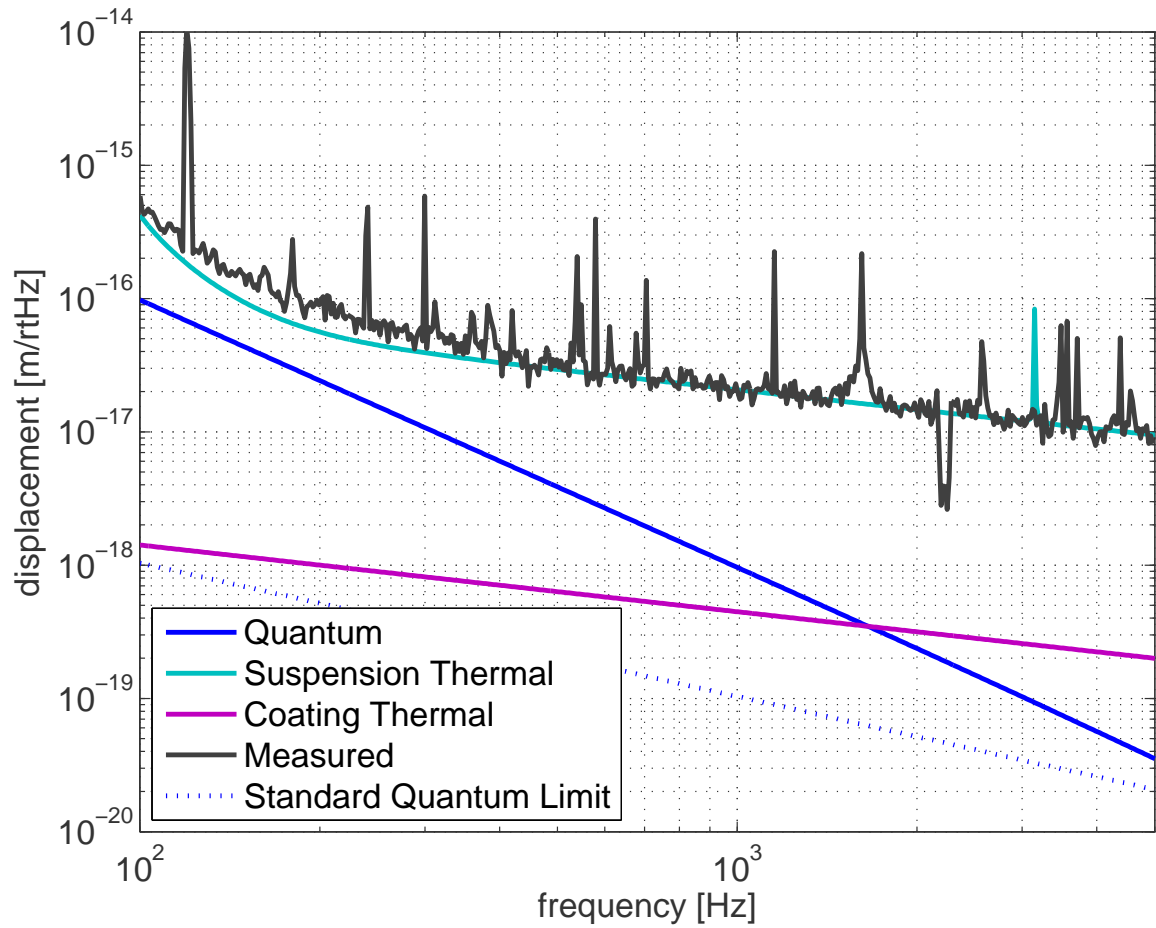
Figure 3-8: Measured displacement noise spectrum for the differential mode, plotted with thermal noise models and the expected quantum noise.

and substrate of each mirror is estimated using the following equation [67]:

$$S_x(\Omega) = \frac{4k_B T}{\Omega \sqrt{\pi}} \frac{1}{w E_s} \left[\phi_s + \frac{d}{w\sqrt{\pi}} \left(\frac{E_c}{E_s} \phi_\parallel + \frac{E_s}{E_c} \phi_\perp \right) \right] \qquad (3.1)$$

where the various symbols are defined as given in table 3.1. Here we assume that the contribution of the substrate loss angle ϕ_s is negligible compared to the contribution due to the coating. We also assume that the input mirror coatings are negligible compared to those of the end mirrors, which have a higher reflectivity and therefore a greater thickness d. Note that the coating thermal noise is large enough to preclude reaching the SQL in this experiment with the end mirrors that we presently use.

The suspension thermal noise term, which explains almost all of the noise we observe, is the subject of chapter 5.

Chapter 4

Trapping and cooling

In this chapter, we discuss several experiments in which radiation pressure and feedback forces were used to trap and cool the suspended mirrors of an interferometer, with the ultimate objective of probing the quantum mechanics of the macroscopic mirrors.

Here *trapping* refers to the use of restoring forces, such as an optical spring, to localize an object. *Cooling*, on the other hand, comes about when damping forces are used to drain away the $k_B T$ thermal energy that the trapped object initially has.

Suppose the thermal energy can be reduced to less than the energy of one phonon, so that the trap's effective temperature T_{eff} satisfies the condition

$$k_B T_{\text{eff}} \lesssim \hbar \Omega_{\text{eff}} \tag{4.1}$$

where Ω_{eff} denotes the resonant frequency of the trap. Then the system settles into an increasingly pure quantum state: the motional ground state. Reaching such a state is a major milestone in itself, as well as a crucial step toward the subsequent preparation of quantum superpositions and entangled states involving the mirror.

As we will see, the right combination of trapping and cooling forces permits the gram- and kilogram-scale mirrors used in our experiments to enter this quantum regime.

4.1 Cold forces

4.1.1 Damping forces

Thermal energy flows into the mirror from the environmental heat bath via the mechanical suspension. The cooling techniques we use are based on the idea of coupling the mirror to an additional environmental bath: one that arises from the optical field. This new bath, at temperature T_o, can be much colder than the environment of the mirror's mechanical suspension at temperature T_m.

Then, instead of the mirror equilibrating with the hot bath at T_m, thermal energy flows through it from the hot bath to the cold one. The mirror eventually reaches an effective temperature T_{eff} that is intermediate between T_o and T_m.

With the mirror at T_{eff}, the rate of heating from the hot bath must balance the rate of cooling from the cold bath. Modeling the dissipation mechanism as viscous damping, characterized by the suspension's damping rate Γ_m and the cold damping rate Γ_o, lets us write a simple equation for the effective temperature:

$$\Gamma_m(T_m - T_{\mathrm{eff}}) = \Gamma_o(T_{\mathrm{eff}} - T_o) \tag{4.2}$$

As expected, we find that the effective temperature interpolates between the two bath temperatures:

$$T_{\mathrm{eff}} = T_m \frac{\Gamma_m}{\Gamma_{\mathrm{eff}}} + T_o \frac{\Gamma_o}{\Gamma_{\mathrm{eff}}} \tag{4.3}$$

Each bath's contribution is weighted by its damping rate relative to the total effective damping $\Gamma_{\mathrm{eff}} = \Gamma_m + \Gamma_o$.

The ratio T_m/T_{eff} is known as the *cooling factor*. Whenever the cold damping rate dominates the mechanical one, a large cooling factor is possible.

In our experiments, cold damping forces are derived from low-noise (ideally, quantum-limited) optical fields. Sometimes we choose to work with a detuned cavity, in which the radiation pressure force acts directly on the mirror. In other cases, we operate the cavity at zero detuning, and the optical field exiting the cavity is detected and fed back to the mirror. In the literature, only the latter technique is usually

referred to as "cold damping", while the former usually goes by the name of "cavity cooling".

The cavity cooling technique, it should be noted, is closely related to the family of laser cooling techniques developed for atomic systems, particularly the coherent scattering method described by Vuletić and Chu [137]. Cavity cooling can be understood in terms of the coherent scattering of photons by the mirror, into the two vibrational sidebands at $\pm\Omega_{\text{eff}}$. The detuned cavity serves to enhance the rate of scattering to the upper sideband. Every time this up-scattering process occurs, the mirror loses another phonon of vibrational energy.

The cooling factor we can attain with these techniques is subject to two limits:

- No matter how strong the damping force we apply, the mirror does not cool below the temperature T_o of the cold bath. Bath temperatures for cold damping and cavity cooling will be estimated in sections 4.3 and 4.5.

- No matter how cold the cold bath is, there is a limit to how strong a damping force it is *useful* to apply. Increasing the damping rate Γ_o degrades the effective quality factor $Q_{\text{eff}} = \Omega_{\text{eff}}/\Gamma_o$ of the mirror oscillator. The quality factor should not be degraded below $Q_{\text{eff}} \sim 0.5$, or else the mirror becomes critically damped and ceases to be an oscillator. This constraint implies a finite upper limit for the cooling factor, even when $T_o = 0$:

$$\frac{T_m}{T_{\text{eff}}} < \frac{2\Omega_{\text{eff}}}{\Gamma_m} \tag{4.4}$$

4.1.2   Restoring forces

Cold restoring forces vastly enlarge the class of mechanical systems that are able to approach the ground state. To understand why, let us first consider what happens when such forces are *not* being used, so that all the trapping force is provided by the mechanics ($\Omega_{\text{eff}} = \Omega_m$).

Ground state cooling becomes possible only when the cooling factor limit stated above in equation (4.4) is sufficient to reach the effective temperature required by

equation (4.1). That is, we require

$$k_B T_m \lesssim \hbar \Omega_\text{eff} \frac{2\Omega_\text{eff}}{\Gamma_m} \qquad (4.5)$$

In the absence of external trapping forces, we would have to design the suspension so as to optimize its resonant frequency-quality factor product Ω_m^2 / Γ_m. Tenuous, low frequency suspensions with minimal damping, like those used in gravitational wave detectors, fare poorly under this figure of merit, which favors increased stiffness over improved losses.

However, if cold restoring forces dominate ($\Omega_\text{eff} = \Omega_m + \Omega_o \gg \Omega_m$), then the suspension's stiffness is no longer relevant in equation (4.5): its damping rate is the only property that matters. Thus, we are free to optimize the damping rate and the resonant frequency as independent variables — designing the mechanical system purely to minimize losses, and placing the resonant frequency where we want it using a cold force.

This scheme for shifting the resonant frequency has been called "optical dilution", which is a name that alludes to the damping dilution effect of gravity in pendulums [124, 30, 119]. Consider that a thin wire loaded with a massive bob forms an oscillator even in zero gravity, since the wire's elasticity provides a (very weak) restoring force. Such a device would have damping similar to that of a pendulum under gravity. But in the pendulum, the gravitational restoring force (which is practically lossless) dominates over that of the wire, shifting the resonance to a much higher frequency. Consequently, a pendulum has less dissipation *per oscillation period* (that is, a better quality factor) than the same device would exhibit in the absence of gravity.

In our system, cold restoring forces that arise from the optical field play a role that is analogous to the gravitational force on a pendulum. As with the damping forces treated in the previous section, a cold restoring force can be produced in two ways. We may detune the cavity to produce an optical spring, or adjust the feedback to provide a "servo spring". In the experiment we will discuss next, the optical spring takes center stage.

4.2 Stable all-optical trap

The experiment introduced in this section was designed to show that a combination of radiation pressure forces can overwhelm the mechanical forces of a mirror suspension, creating a stable trap for the mirror. The result was published in reference [37].

4.2.1 Background

The previous literature on optical trapping of suspended mirrors includes a remarkable early experiment by Dorsel et al. [45], which illustrated both the stabilizing and the destabilizing aspects of radiation pressure forces. Subsequent work on suspended-mirror interferometers had considered optical springs and optical (anti-)damping forces in separate contexts:

- The possibility of making strong optical springs was explored, theoretically and experimentally [29, 27, 128]. Proposals were advanced for applying the optical spring to enhance the sensitivity of gravitational wave detectors [29, 96], and to generate ponderomotively squeezed light [40].

- The threat of the optical anti-damping force to destabilize a cavity, and give rise to parametric instabilities of the mirror acoustic modes, was identified and demonstrated [38, 96].

Meanwhile, in micro- and nano-mechanical experiments, optical springs strong enough to approach the stiffness of the mechanics had not been pursued. But several groups had demonstrated strong optical damping forces, and recognized their application to cooling the system toward the ground state [92, 100, 58, 15, 126].

As we will discuss below, the (stabilizing) optical spring force is normally accompanied by the (destabilizing) anti-damping force, while the (stabilizing) damping force is accompanied by a (destabilizing) anti-spring. Therefore, a stable system whose dynamics were fully dominated by radiation pressure forces had never been observed. The regime had been achieved only with the help of active feedback control to stabilize the dynamics [38, 96].
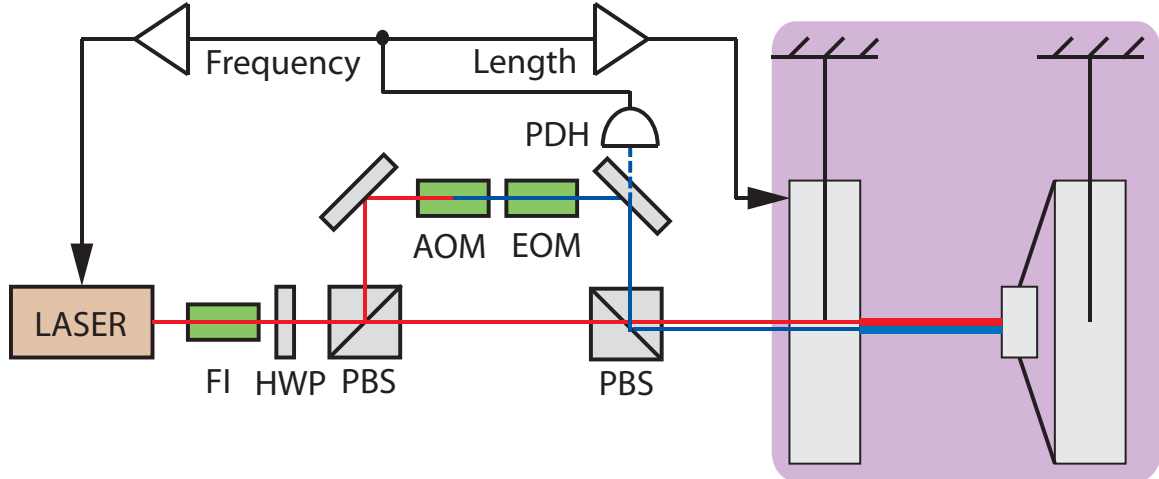
Figure 4-1: Simplified schematic of the double optical spring experiment. The high-power carrier beam is shown in red, while the low power subcarrier beam is shown in blue. The shaded box denotes seismically isolated suspended optics inside the vacuum chamber. Abbreviation key: FI = Faraday isolator; HWP = half-wave plate; PBS = polarizing beamsplitter; AOM = acousto-optic modulator; EOM = electro-optic modulator; PDH = Pound-Drever-Hall readout photodetector.

However, in this experiment, we overcome the instability by using the radiation pressure of a second optical field, thus providing a stable all-optical trap.

4.2.2 Experimental setup

The setup shown schematically in figure 4-1 was used to demonstrate the optical trapping scheme. The 250 gram input mirror of the $L = 0.9$ m long cavity is suspended as a pendulum with oscillation frequency of 1 Hz for the longitudinal mode. The 1 gram end mirror is suspended by two optical fibers 300 μm in diameter, giving a natural frequency $\Omega_m = 2\pi \times 172$ Hz for its mechanical mode, with quality factor $Q_m = 3200$. On resonance, the intracavity power is enhanced relative to the incoming power by a resonant gain factor $4/t_I^2 \approx 5 \times 10^3$, where t_I^2 is the power transmission of the input mirror, and the resonant linewidth (HWHM) is $\gamma_c = 2\pi \times 11$ kHz.

About 3 W of 1064 nm Nd:YAG laser light passes through a Faraday isolator before it is split into two paths by a half-wave plate and polarizing beamsplitter (PBS) combination that allows control of the laser power in each path. The carrier (C) field comprises most of the light incident on the suspended cavity. About 5% of the light is
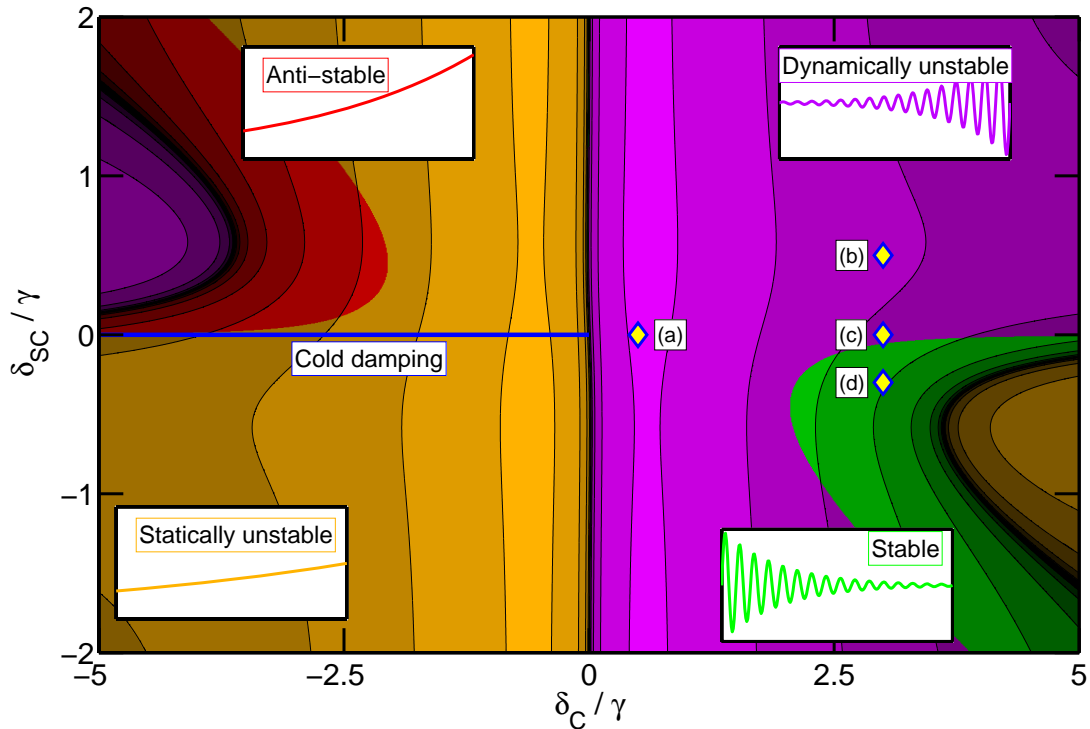
Figure 4-2: Graphical representation of the total optical rigidity due to both optical fields, as a function of carrier and subcarrier detuning, for fixed input power (power in the subcarrier field is $\sim 1/20$ the carrier power) and observation frequency ($\Omega = 2\pi \times 1$ kHz). The shaded regions correspond to detunings where the real and imaginary parts of the total spring constant are differently positive or negative. The (logarithmically spaced) contours shown are scaled according to Ω_{eff}: brighter regions have larger Ω_{eff}. The labels (a) – (d) refer to the measurements shown in figure 4-3.

frequency-shifted by 161.66 MHz, equal to one free spectral range (FSR) $\dfrac{c}{2L}$, using an acousto-optic modulator, and phase modulated by an electro-optic modulator (New Focus 4004). This subcarrier (SC) field can further be detuned from resonance to create a second optical spring. The two beams are recombined on a second PBS before being injected into the cavity, which is mounted on a seismic isolation platform in a vacuum chamber. A Pound-Drever-Hall (PDH) error signal [46] derived from the SC light reflected from the cavity is used to lock it, with feedback to both the cavity length as well as the laser frequency. By changing the frequency shift of the subcarrier, the carrier can be shifted off resonance by arbitrarily large detunings.

4.2.3 Double spring technique

As we found in chapter 2, when the cavity is detuned from resonance, the radiation pressure force acts as a spring with a complex, frequency-dependent spring constant, the real part of which can be written as follows in the quasistatic regime:

$$
\begin{aligned}
\mathrm{Re}\left\{K_o\right\} &= m\Omega_o^2 \\
&= m\Omega_q^2 \frac{\delta}{2}\left(\frac{1}{1+\delta^2}\right)^2
\end{aligned}
\tag{4.6}
$$

Recall that Ω_q is the "quantum frequency" where the undetuned cavity's quantum noise touches the SQL, and δ is the detuning relative to the cavity linewidth.

Note the dependence of Ω_o^2 on the sign of the detuning δ. For $\delta > 0$ (in our convention), $\Omega_o^2 > 0$ corresponds to a restoring force, while $\delta < 0$ gives an anti-restoring force. We do not explore the latter regime experimentally since it is always unstable for our system (see figure 4-2).

Moreover, due to the delayed response of the cavity light to mirror motion, the restoring force is accompanied by viscous damping, with damping rate Γ_o given by:

$$
\begin{aligned}
\mathrm{Im}\left\{K_o\right\} &= m\Omega\Gamma_o \\
&= -\mathrm{Re}\left\{K_o\right\}\frac{2\Omega}{\gamma_c}\left(\frac{1}{1+\delta^2}\right)
\end{aligned}
\tag{4.7}
$$

Because the cavity response lags the motion of the mirrors, a *restoring* spring constant coincides with *anti-damping*, while *damping* coincides with an *anti-restoring* force. We can now see that when both optical forces dominate their mechanical counterparts, the system becomes unstable.

To stabilize the system we use two optical fields that respond on different time scales. One field should respond quickly, so that it makes a strong restoring force and only a weak anti-damping force. The other field should respond slowly, so that it creates a strong damping force, with only a minor anti-restoring force.

This configuration could be achieved with two cavities of differing bandwidths that share a common end mirror. However, it is simpler to use a single cavity and two

fields with vastly different detunings. From equations (4.6) and (4.7), we find

$$\frac{\text{Im}\left\{K_o\right\}}{\text{Re}\left\{K_o\right\}} = -\frac{2\Omega}{\gamma_c}\left(\frac{1}{1+\delta^2}\right), \tag{4.8}$$

suggesting that an optical field with larger detuning has less damping per stiffness. The physical mechanism for this is that at larger detunings, the optical field resonates less strongly than for smaller detunings, so the time scale for the cavity response is shorter, leading to smaller optical damping.

To create a stable system, we consider a carrier field with large detuning $\delta_C \approx 3$ that creates a restoring force, but also a small anti-damping force. To counteract the anti-damping, a strong damping force is created by injecting a subcarrier with small detuning $\delta_{SC} \approx -0.5$. For properly chosen power levels in each field, the resulting system is stable; we found a factor of 20 higher power in the carrier to be suitable in this case.

To illustrate the behavior of the system at all detunings, the various stability regions are shown in figure 4-2 for this fixed power ratio. Point (d) in particular shows that the system is stable for our chosen parameters.

4.2.4   Discussion

Noteworthy features of this optical trapping technique include:

- **Extreme rigidity**: With no subcarrier detuning and $\delta_C \approx 0.5$, the 172 Hz mechanical resonance of the 1 gram mirror oscillator was shifted as high as 5 kHz (curve (a) in figure 4-3), corresponding to an optical rigidity of $\text{Re}\left\{K_o\right\} = 2 \times 10^6$ N/m.

  To put this number into perspective, consider replacing the optical mode with a rigid beam with Young's modulus E. The effective Young's modulus of this mode with area A of the beam spot (1.5 mm^2) and length $L = 0.9$ m of the cavity, is given by $E = m\Omega_{\text{eff}}^2 L/A = 1.2$ TPa, stiffer than any known material (but also with very small breaking strength). Such rigidity is required to operate
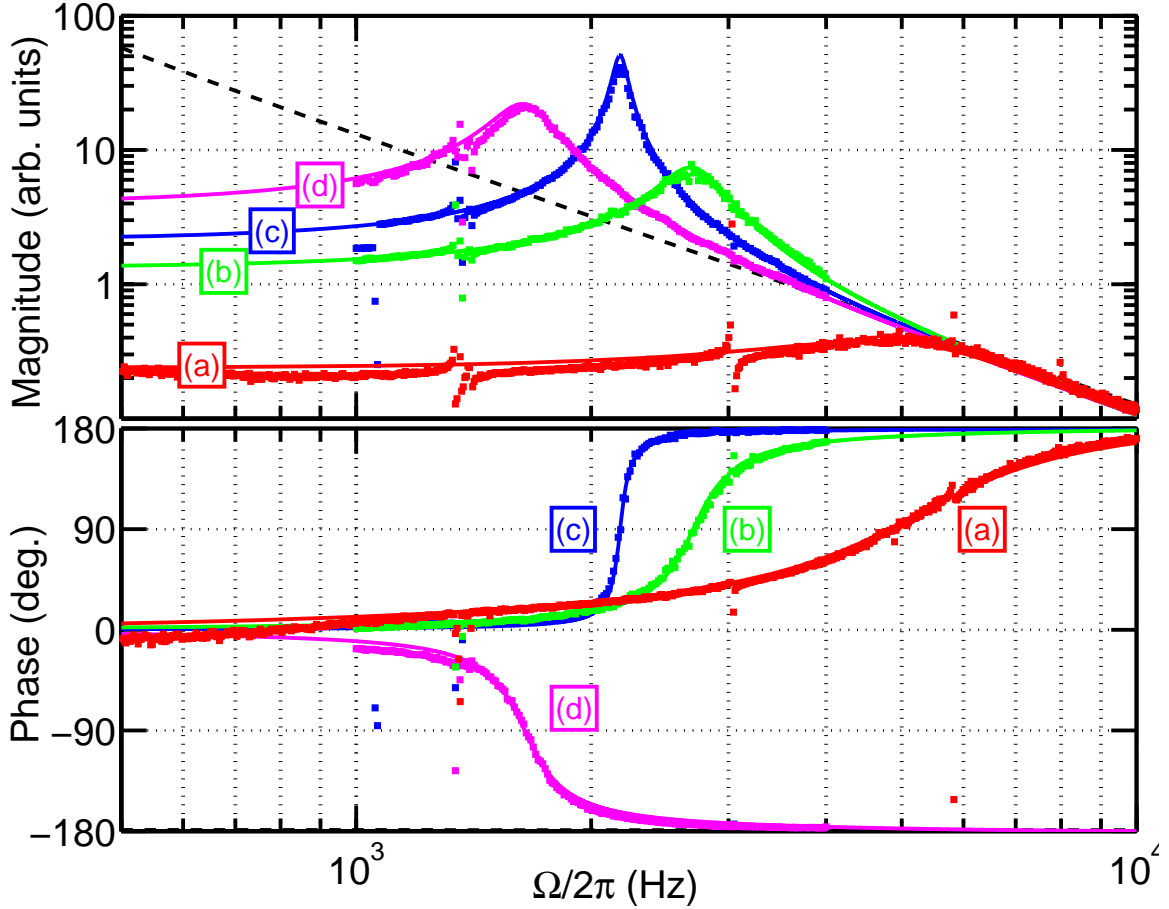
Figure 4-3: The optical spring response for various power levels and detunings of the carrier and subcarrier. Measured transfer functions of displacement per force are shown as points, while the solid lines are theoretical curves. The dashed line shows the response of the system with no optical spring. An unstable optical spring resonance with varying damping and resonant frequency is produced when (a) $\delta_C = 0.5, \delta_{SC} = 0$; (b) $\delta_C = 3, \delta_{SC} = 0.5$; (c) $\delta_C = 3, \delta_{SC} = 0$; and it is stabilized in (d) $\delta_C = 3, \delta_{SC} = -0.3$. Note that the damping of the optical spring increases greatly as the optomechanical resonance frequency increases, approaching $\Gamma_{\text{eff}} \approx \Omega_{\text{eff}}$ for the highest frequency optical spring.

the cavity without external control; ambient motion would otherwise disrupt the cavity resonance condition.

- **Stabilization**: Also shown in figure 4-3 are curves corresponding to varying carrier and subcarrier detunings. In curves (b), (c) and (d), we detune the carrier by more than the cavity linewidth since the optical spring is less unstable for large δ_C. With no subcarrier detuning, the optomechanical resonant frequency reaches $\Omega_{\text{eff}} = 2\pi \times 2178$ Hz, shown in curve (c). Note that the optical spring is unstable, as evidenced by the phase *increase* of 180° about the resonance (corresponding to anti-damping).

  Next we detune the subcarrier in the same direction as the carrier, shown in curve (b), which increases the resonant frequency and also increases the anti-damping, demonstrated by the broadening of the resonant peak. For both curves (b) and (c), electronic servo control is used to keep the cavity locked. If the control system is disabled, the amplitude of the cavity field and mirror oscillations grow exponentially.

  Remarkably, when the subcarrier is detuned in the opposite direction from the carrier, the optical spring resonance becomes stable, shown in curve (d), allowing operation of the cavity without electronic feedback at frequencies above 30 Hz; we note the change in phase behavior and the reduction of the resonant frequency. This shows how the frequency and damping of the optical spring can be independently controlled.

- **Optical cooling**: In this experiment, the displacement spectrum is dominated by laser frequency noise at Ω_{eff}. We can nonetheless estimate the effective temperature of the optomechanical mode by measuring the displacement of the mirror, and equating

$$\frac{1}{2}m\Omega_{\text{eff}}^2 x_{\text{rms}}^2 = \frac{1}{2}k_B T_{\text{eff}} \tag{4.9}$$

  where x_{rms} is the RMS motion of the mirror.

  To determine x_{rms} in this experiment, we measure and integrate over the noise
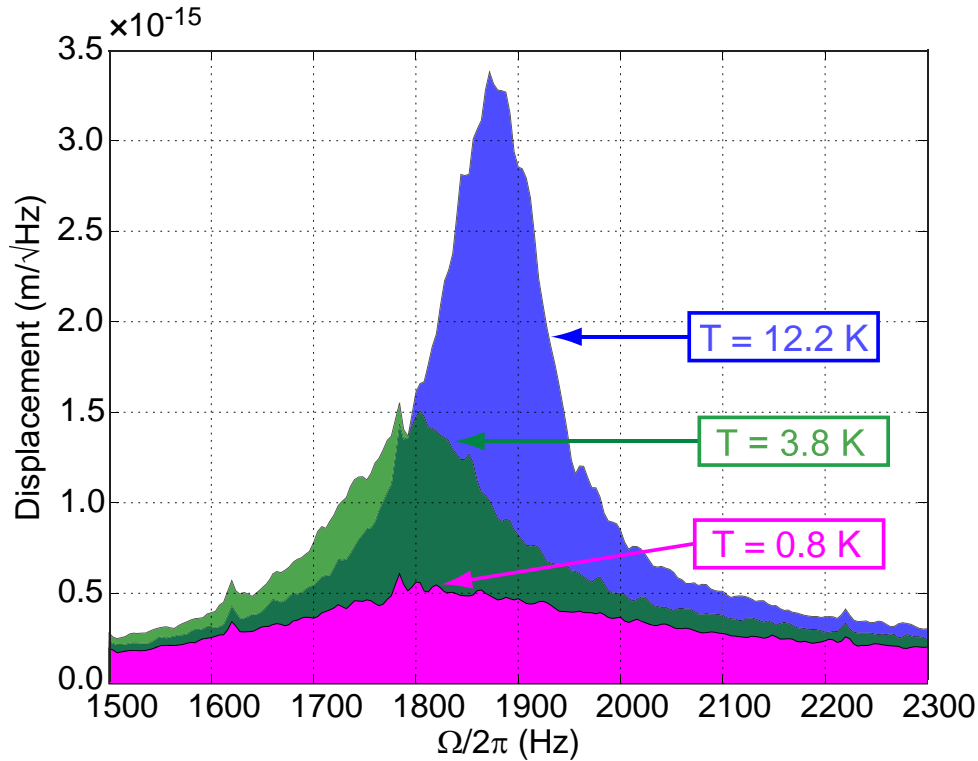
Figure 4-4: The measured noise spectral density of the cavity length is shown for several configurations corresponding to different detunings. The magenta curve corresponds to $\delta_C \approx 3$ and $\delta_{SC} \approx -0.5$. The green and blue curves are obtained by reducing δ_{SC} and increasing δ_C in order to keep Ω_{eff} approximately constant, while varying Γ_{eff}. The spectrum is integrated between 1500 and 2300 Hz to calculate the rms motion of the oscillator mode, giving effective temperatures of 0.8, 3.8 and 12.2 K. The limiting noise source here is not thermal noise, but in fact frequency noise of the laser, suggesting that with reduced frequency noise, even lower temperatures could be attained.

spectral density of the error signal from the cavity, calibrated by injecting a frequency modulation of known amplitude at 12 kHz. The displacement noise measured in this way is shown in figure 4-4. The lowest measured temperature is 0.8 K, corresponding to a cooling factor of 2.5×10^3.

In the next section we will investigate the quantum limit of the double optical spring technique. We will find that radiation pressure noise presents an obstacle, and that feedback forces offer in some respects a more convenient route to the ground state in a suspended-mirror cavity like ours. However, the ability to operate such a cavity *without* feedback control remains a unique advantage of this scheme, which is made possible by the rigidity and stability of the double spring.

4.3   Quantum limit of optical forces

To understand the limitations of optically-derived forces as applied to cooling, we would like to estimate the effective temperature T_o of the cold bath that an optical field provides. The quantum noise of the light determines this ultimate limiting temperature.

In the double-spring optical trap discussed in the previous section, where radiation pressure forces act in a detuned cavity, the limit to cooling can be attributed to the intra-cavity radiation pressure fluctuations. Recall from chapter 2 that, in the quasistatic approximation ($\Omega \ll \gamma_c$), the radiation pressure force noise has a white power spectrum whose magnitude is given by

$$S_F^{(RP)}(\Omega) = \hbar m \Omega_q^2 \left(\frac{1}{1 + \delta^2} \right)^2 \tag{4.10}$$

To estimate T_o, we can equate $S_F^{(RP)}$ with the magnitude of a thermal excitation spectrum,

$$S_F^{(T)}(\Omega) = 4 k_B T_o m \Gamma_{\text{eff}} \tag{4.11}$$

Writing the result in terms of the carrier optical spring frequency Ω_C, and subcarrier damping rate Γ_{SC}, we obtain useful expressions for the phonon occupation number due to each optical field:

$$
\begin{aligned}
N_C &= \frac{k_B T_C}{\hbar \Omega_{\text{eff}}} \\
&= \frac{1}{2} \frac{\Omega_C^2}{\Omega_{\text{eff}} \Gamma_{\text{eff}}} \frac{1}{\delta_C}
\end{aligned}
\tag{4.12}
$$

$$
\begin{aligned}
N_{SC} &= \frac{k_B T_{SC}}{\hbar \Omega_{\text{eff}}} \\
&= -\frac{1}{2} \frac{\Gamma_{SC}}{\Gamma_{\text{eff}}} \frac{1 + \delta_{SC}^2}{2 \delta_{SC}} \frac{\gamma_c}{\Omega_{\text{eff}}}
\end{aligned}
\tag{4.13}
$$

From equation (4.12), we see that the carrier's contribution N_C can be made negligibly small, in the limit of large carrier detuning δ_C. It should be noted that, in this limit, the carrier power must be vastly increased, in order to maintain the desired

optical spring frequency (the required power scales as δ_C^3).

When it comes to the subcarrier's contribution N_{SC}, we seem to be caught between a rock and a hard place. Even after optimizing the detunings (choosing δ_C large so that $\Gamma_{\text{eff}} \approx \Gamma_{SC}$, and setting $\delta_{SC} = -1$), equation (4.13) reduces to $N_{SC} \approx \gamma_c/(2\Omega_{\text{eff}})$. So we cannot approach the ground state as long as $\Omega_{\text{eff}} \ll \gamma_c$. But as Ω_{eff} starts to approach γ_c, we have the problem that the quasistatic approximation breaks down, and the system can no longer be treated as a simple oscillator governed by an optical spring constant. (The optical restoring force becomes frequency-dependent.)

There is, however, one possible escape from this subcarrier noise dilemma. N_C and N_{SC} can both be improved by using squeezed light to suppress the radiation pressure noise, which would allow the double-spring oscillator to approach the ground state.

We note that micro-mechanical cooling experiments often use very stiff mirror oscillators, with $\Omega_m \gtrsim \gamma_c$. In such cases the optical damping force may be suitable for ground state cooling [55]. This regime is sometimes referred to as the "good cavity" limit. However, the phrase is quite misleading, since whether a cavity is "good" or not surely depends on the application that one has in mind. It turns out that cavities like the ones we use — which are less convenient for implementing passive cavity cooling schemes — are especially well suited to the purpose of monitoring the mirror displacement. In what follows, we will introduce an alternative cooling strategy that plays to the strengths of a cavity that is "good" for measurement.

4.4   Feedback cooling

In this section, we discuss an experimental demonstration of improved mirror cooling, using a feedback-based cold damping approach. This work was previously published in reference [39].

4.4.1   Cold damping technique

The roots of the cold damping technique can be traced back at least as far as 1956, when vibration reduction in mechanical structures by active feedback was discussed

by Olson [105]. In 1979, Robert Forward (also the builder of an early prototype gravitational wave interferometer) used feedback to damp a structure supporting a mirror [51]. Active damping in the context of quantum noise was introduced by Mancini et al. [86], experimentally implemented by Cohadon et al. [36], and subsequently applied by other groups [78, 117].

Cold damping relies on a highly sensitive readout of mirror displacement that, in our experiments, is provided by the light that exits the cavity. We synthesize a damping force by tailoring the filter function that is applied to the displacement signal before feeding it back to control the mirror.

The degree of freedom that we seek to monitor and control is the mirror's center-of-mass displacement x. However, our optical measurements actually probe the location of the mirror surface (averaged over the optical beam), which differs from the center-of-mass location due to the mirror's *internal* thermal noise, and includes an additional *sensing* noise due to the laser shot noise. Combining these noises into a total displacement noise x_S, we can write the output signal as

$$x_{\mathrm{meas}} = x + x_S \tag{4.14}$$

The center-of-mass is also subject to force noises F, such as radiation pressure noise and the thermally driven motion of the mirror suspensions, plus the optical spring force, and our feedback force, which is proportional to $\widetilde{x}_{\mathrm{meas}}$ in the frequency domain:

$$-m\left(\Omega^2 - i\Omega\Gamma_m - \Omega_m^2\right)\widetilde{x} = \widetilde{F} - K_o(\Omega)\widetilde{x} - K_f(\Omega)\widetilde{x}_{\mathrm{meas}} \tag{4.15}$$

Here $K_o(\Omega)$ is the (complex) optical spring constant as defined in equations (4.6) and (4.7), while $K_f(\Omega)$ is the feedback kernel. In this experiment, we have

$$K_f(\Omega) \approx im\Omega\Gamma_f \tag{4.16}$$

with Γ_f large enough to overwhelm the optical anti-damping Γ_o, such that the modified dynamics of x are stable.

Combining the preceding equations, we can write the equation of motion for the damped oscillator under feedback, driven by random forces:

$$\left(-m\Omega^2 + im\Omega\Gamma_{\text{eff}} + m\Omega_{\text{eff}}^2\right)\widetilde{x} = \widetilde{F} - K_f(\Omega)\widetilde{x}_S \tag{4.17}$$

The added noise term $K_f(\Omega)\widetilde{x}_S$ in equation (4.17) represents the conversion of sensing noise into a force noise on the optic, by the action of the feedback system. This noise mechanism is the price we pay for cold damping, and it will be analyzed further in section 4.5.

4.4.2   Experimental setup

We turned to cold damping in this work after modifying the experiment of section 4.2 in order to achieve a lower noise floor. The apparatus, shown schematically in figure 4-5, is identical to that of section 4.2 except for the following upgrades:

- The coupling of laser frequency noise to cavity displacement is reduced by shortening the cavity length L by nearly a factor of 10 (from 0.9 m to 10 cm). At the 10 cm length, the bases of the mirror suspension towers nearly touch each other, precluding any further reduction.

- The thermal noise of the end mirror suspension is improved by snipping its fibers just below the point where they attach to the 1 gram mirror. In this way, the suspension is reduced in stiffness by a factor of 180, and in mechanical loss by a factor of 80 (from $\Omega_m = 2\pi \times 180$ Hz with a Q_m of 3200 to $\Omega_m = 2\pi \times 12.7$ Hz with a Q_m of 19950).

After improving the frequency noise by a factor of 10, and the thermal noise by an even larger factor, we would expect to again be limited by frequency noise, but with $T_{\text{eff}} \sim x_{\text{rms}}^2$ about 100 times lower. However, the shorter cavity length also imposes two significant limitations:

- The cavity FSR is stretched from 160 MHz to 1.5 GHz. Consequently, the 160 MHz AOM that formerly generated the subcarrier field (offset by one FSR)
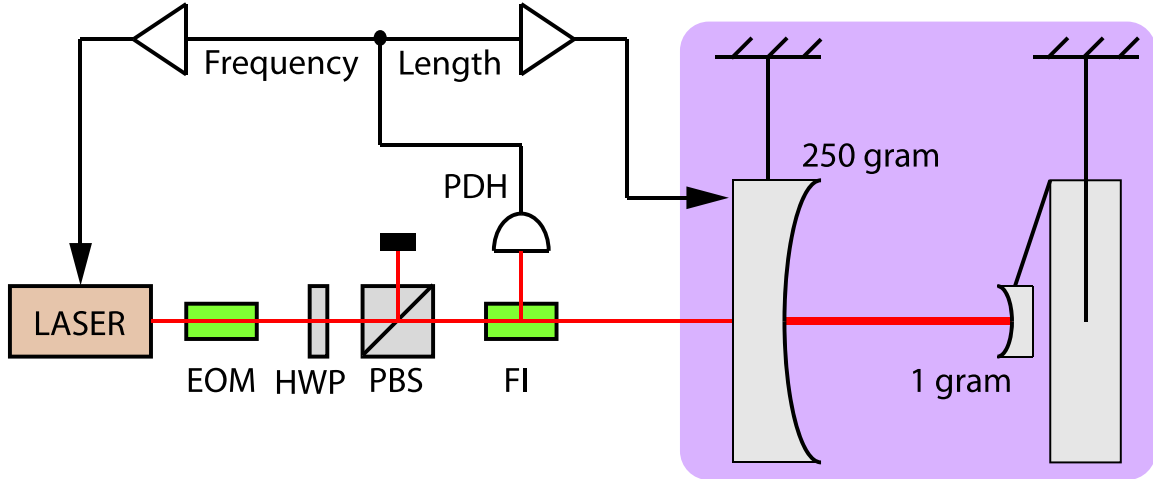
Figure 4-5: Simplified schematic of the feedback cooling experiment. (Compare to figure 4-1.)

can no longer be used for that purpose. Although it would be not be hard to make and use a subcarrier in the same FSR as the carrier (for instance, via two opposing AOMs, or an additional phase-locked laser), it is even easier to dispense with the subcarrier, and apply cold damping instead.

- The cavity linewidth γ_c is broadened from $2\pi \times 11$ kHz to $2\pi \times 95$ kHz. This change weakens the filtering action of the cavity pole on the intracavity radiation pressure, at the 137 kHz drumhead mode frequency of the 1 gram mirror. As a result, this mode becomes easier to push into parametric instability (and is very difficult to stabilize by feedback, since the end mirror is not actuated directly). To avoid ringing up the drumhead mode, we operate with only about 100 mW of input laser power, when the laser is detuned on the blue side of the cavity resonance to make an optical spring. Thus the optical spring frequency is limited to about 1 kHz.

To maximize the optical restoring force, the cavity is locked off-resonance by $\delta \approx 0.5$. The PDH error signal for the locking servo is split between a high bandwidth analog path fed back to the laser frequency, and a digital path fed back to the input mirror's magnet/coil actuators.
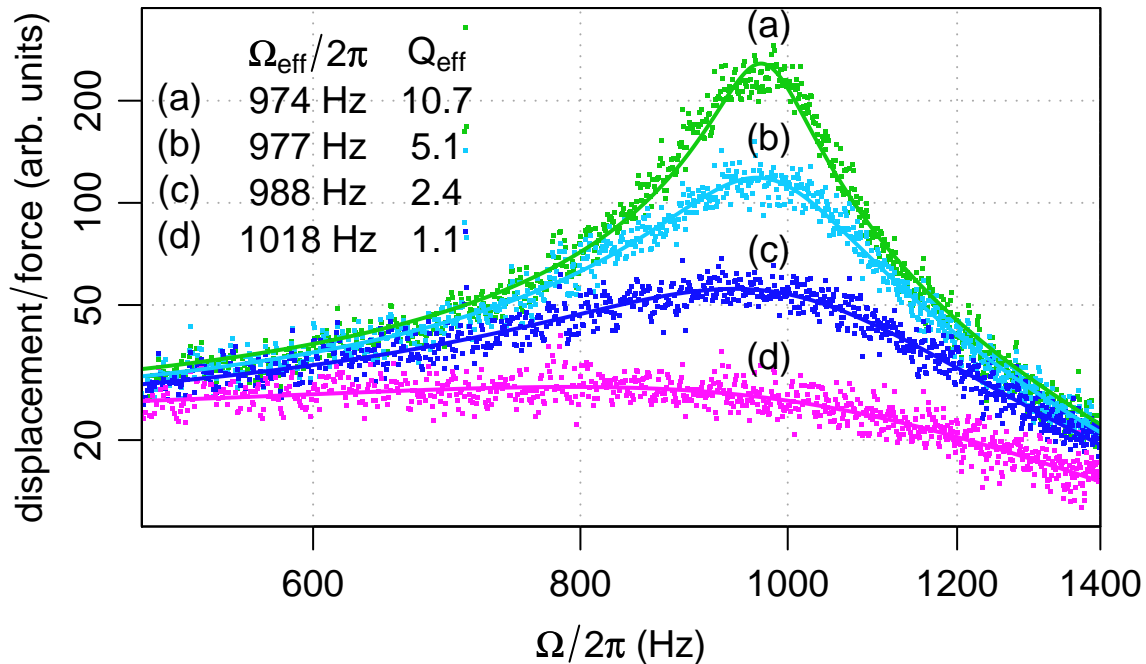
Figure 4-6: The transfer function of an applied force to mirror motion, for increasing levels of damping [curves (a) to (d)]. The force is applied via the magnet/coil actuators, and the response is measured by the PDH error signal. The points are measured data, and the lines are fitted Lorentzians from which the resonant frequency and damping constant are derived for each configuration. Statistical errors in the fit parameters are of order 1%.

The digital feedback is used at frequencies below 10 Hz to keep the cavity locked in its operating state. The analog path to the laser frequency is arranged so that it provides derivative feedback, damping and cooling the motion of the oscillator. The effective damping may be controlled by adjusting the gain of the feedback loop.

Additional analog feedback is supplied to the magnet/coil actuators to damp a parametric instability of the input mirror at 28 kHz [77, 38].

4.4.3 Results

As expected, the noise in this experiment remains dominated by frequency noise of the laser at Ω_{eff}. We estimate the effective temperature of the optomechanical mode, as determined by this noise, according to equation (4.9).

To determine x_{rms} in our experiment, we first find the resonant frequency and damping of the oscillator by measuring its frequency dependent response to a driving
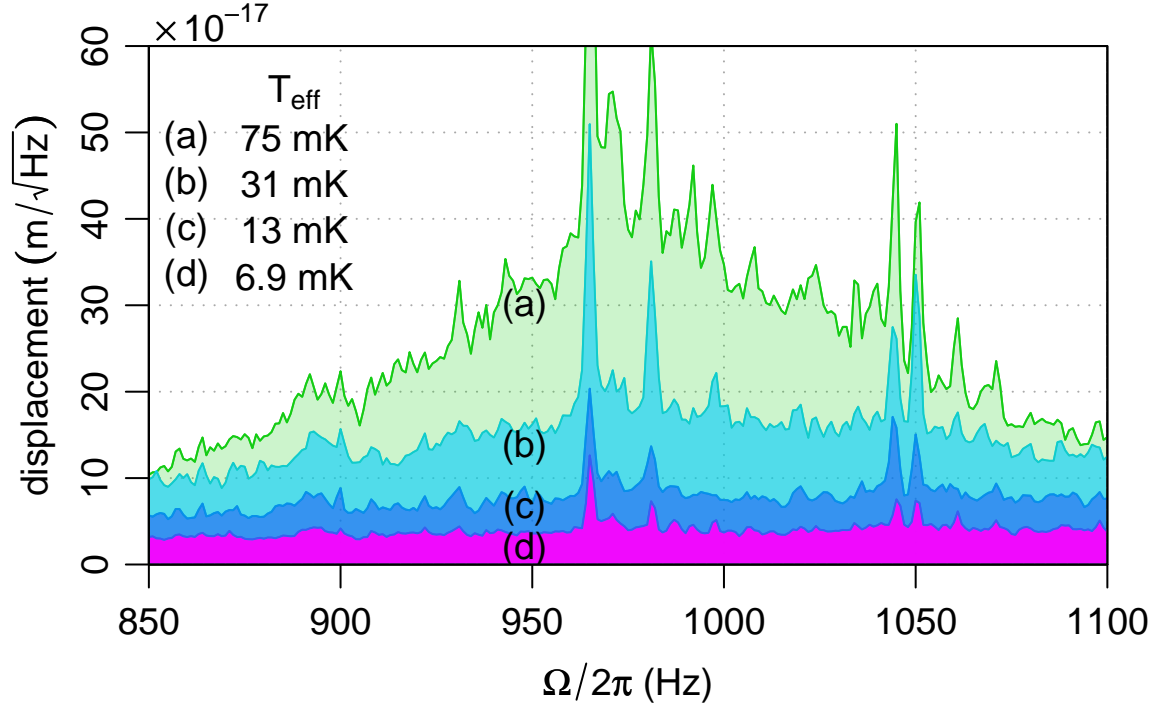
Figure 4-7: The measured noise spectral density of the mirror displacement. The curves (a) to (d) correspond to increasing gain in the damping feedback loop; for each, the parameters of the resonance are measured and depicted in figure 4-6. The spectra are integrated from 850 to 1100 Hz, the frequency range where the mirror motion is the dominant signal, to obtain the rms motion of the mirror and its effective temperature. The broad limiting noise source is frequency noise of the laser. Narrow spectral features in addition to the main optical spring resonance are due to coupling of acoustically driven phase noise.

force, shown in figure 4-6. In the same configuration, we then measure the noise spectral density of the error signal from the cavity, calibrated by injecting a frequency modulation of known amplitude at 12 kHz. The measured displacement spectra, as the electronic damping was varied, are shown in figure 4-7.

Since the effective resonant frequency is at $\Omega_{\text{eff}} \approx 2\pi \times 1000$ Hz, we integrate the spectrum from 850 Hz to 1100 Hz to obtain an estimate of the motion of the mirror. To correct for the finite integration band, we assume a thermally driven displacement noise spectrum for the oscillator, given by

$$S_x^{(T)}(\Omega) = \frac{4k_B T \Gamma_{\text{eff}}/m}{(\Omega_{\text{eff}}^2 - \Omega^2)^2 + \Omega^2 \Gamma_{\text{eff}}^2} \tag{4.18}$$

and find T_{eff} by setting our measured spectrum integral equal to a thermal spectrum

integrated over the same frequency band. The lowest temperature reached is 6.9 ± 1.4 mK. Thus the cooling factor from the ambient $T_m = 295$ K is 43000 ± 11000. Systematic error in the calibration dominates statistical error in these uncertainty estimates.

We note that the mechanical quality factor was increased by a factor of about 80, from 19950 to 1.6×10^6, by optical dilution. Without the cold restoring force, a cooling factor exceeding $2Q_m = 39900$ cannot be achieved in this system, due to the limit of equation (4.4).

4.5 Quantum limit of feedback forces

Returning to equation (4.17), which governs the center-of-mass motion under feedback forces, let us now suppose that the noise terms $\widetilde{F}$ and $\widetilde{x}_S$ are due to radiation pressure noise and shot noise, respectively. So in the quasistatic approximation and with detection in the optimal quadrature, both noises are white, with spectral densities given by:

$$S_F^{(RP)}(\Omega) = \hbar m \Omega_q^2 \left(\frac{1}{1 + \delta^2} \right)^2 \tag{4.19}$$

$$S_x^{(S)}(\Omega) = \frac{\hbar}{m \Omega_q^2} \left(1 + \delta^2 \right)^2 \tag{4.20}$$

as we derived in chapter 2.

The effective temperature and occupation number associated with the radiation pressure noise were obtained in equation (4.12), which we can now simplify further: only the carrier field is being used, and its optical spring supplies the dominant restoring force ($\Omega_{\mathrm{eff}} \approx \Omega_C$). Accordingly, we write

$$N_C = \frac{1}{2} \frac{Q_{\mathrm{eff}}}{\delta_C} \tag{4.21}$$

Under cold damping with feedback kernel $K_f(\Omega) \approx im\Omega\Gamma_f$, the servo converts shot noise into a frequency-dependent force noise, $K_f(\Omega)\widetilde{x}_S$. Due to the frequency

dependence, a comprehensive treatment of this noise mechanism becomes somewhat complicated [55, 42]. For instance, the feedback must be band-limited in some way, or else the noise at high frequencies would grow without bound.

In this section, we would like to obtain a simple estimate of the limiting occupation number, and so we will make the approximation that the feedback force noise is white: $K_f(\Omega)\widetilde{x}_S \approx K_f(\Omega_{\text{eff}})\widetilde{x}_S$. This approximation is reasonable provided that the oscillator mode is well localized around Ω_{eff} (which is true whenever $Q_{\text{eff}} \gg 1$).

Equating the spectral density of the cold damping feedback noise with that of a thermal excitation, we find the effective temperature and occupation number attributable to the feedback:

$$
\begin{aligned}
N_f &= \frac{k_B T_f}{\hbar \Omega_{\text{eff}}} \\
&= \frac{1}{4} \frac{\Gamma_f^2}{\Omega_q^2} Q_{\text{eff}} \left(1 + \delta_C^2\right)^2
\end{aligned}
\tag{4.22}
$$

In order to set equation (4.22) in a more useful form, we write Ω_q in terms of Ω_{eff}, and Γ_f in terms of $\Gamma_{\text{eff}} \approx \Gamma_f + \Gamma_C$, obtaining

$$
N_f = \frac{1}{8} \frac{\delta_C}{Q_{\text{eff}}} + 2 \frac{\Omega_{\text{eff}}}{\gamma_c} \delta_C \left(\frac{1}{1 + \delta_C^2}\right) + 2 \frac{\Omega_{\text{eff}}^2}{\gamma_c^2} Q_{\text{eff}} \delta_C \left(\frac{1}{1 + \delta_C^2}\right)^2
\tag{4.23}
$$

Note that as long as we select $\Omega_{\text{eff}} \ll \gamma_c$ and $\delta_C \gg 1$, the second two terms of equation (4.23) can be made negligible. Then the total occupation number can be written as follows:

$$
\begin{aligned}
N_{\text{eff}} &= N_C + N_f \\
&\approx \frac{1}{2} \frac{Q_{\text{eff}}}{\delta_C} + \frac{1}{8} \frac{\delta_C}{Q_{\text{eff}}}
\end{aligned}
\tag{4.24}
$$

Finally, we have to optimize the ratio $\delta_C / Q_{\text{eff}}$, so as to achieve the smallest occupation number. The minimum occurs when $\delta_C = 2Q_{\text{eff}}$, which yields $N_{\text{eff}} \approx \frac{1}{2}$. Thus, we are able to approach the ground state under these conditions.

4.6 Toward the ground state in LIGO

Can we bring the trapping and cooling techniques we have developed in this chapter to a LIGO interferometer? This is a rather compelling idea, both for technical and historical reasons.

One technical advantage is the exquisite sensitivity of the LIGO instruments, where most of the non-fundamental noise sources have been wrung out already. Another factor is the kilogram-scale test masses they contain: quantum mechanics has yet to be tested on a mass scale even remotely so large.

In historical terms, the model system of a cavity with a movable mirror, together with the theory of quantum measurement and backaction in such a system, forms the intellectual foundation that underpins almost every experimental effort to reach the mechanical ground state. The interferometric gravitational wave detector is the canonical application that first motivated the development of this body of ideas. So it is fitting to look for ways that advanced gravitational wave detectors can continue to contribute to our understanding of the quantum domain in mechanical systems.

The biggest problem in trapping and cooling the LIGO mirrors is that radiation pressure forces strong enough to manipulate their dynamics are not presently available. However, we have already seen how to replace optical cooling with a feedback damping force. In this section, we will supplant optical trapping with a servo spring, obtaining an electro-optical trap for LIGO's mirrors. The result has been published in reference [3].

4.6.1 The LIGO interferometers

In the initial phase of LIGO, three kilometer-scale interferometric detectors were operated, with the goal of directly detecting gravitational waves of astrophysical origin [9, 4]. The results reported here are derived from measurements performed on the 4 km detector at LIGO's Hanford Observatory.

The detector, shown in figure 4-8, comprises a Michelson interferometer with a 4 km long Fabry-Perot cavity of finesse 220 placed in each arm in order to increase the sensitivity. Each mirror of the interferometer has mass 10.8 kg, and is suspended

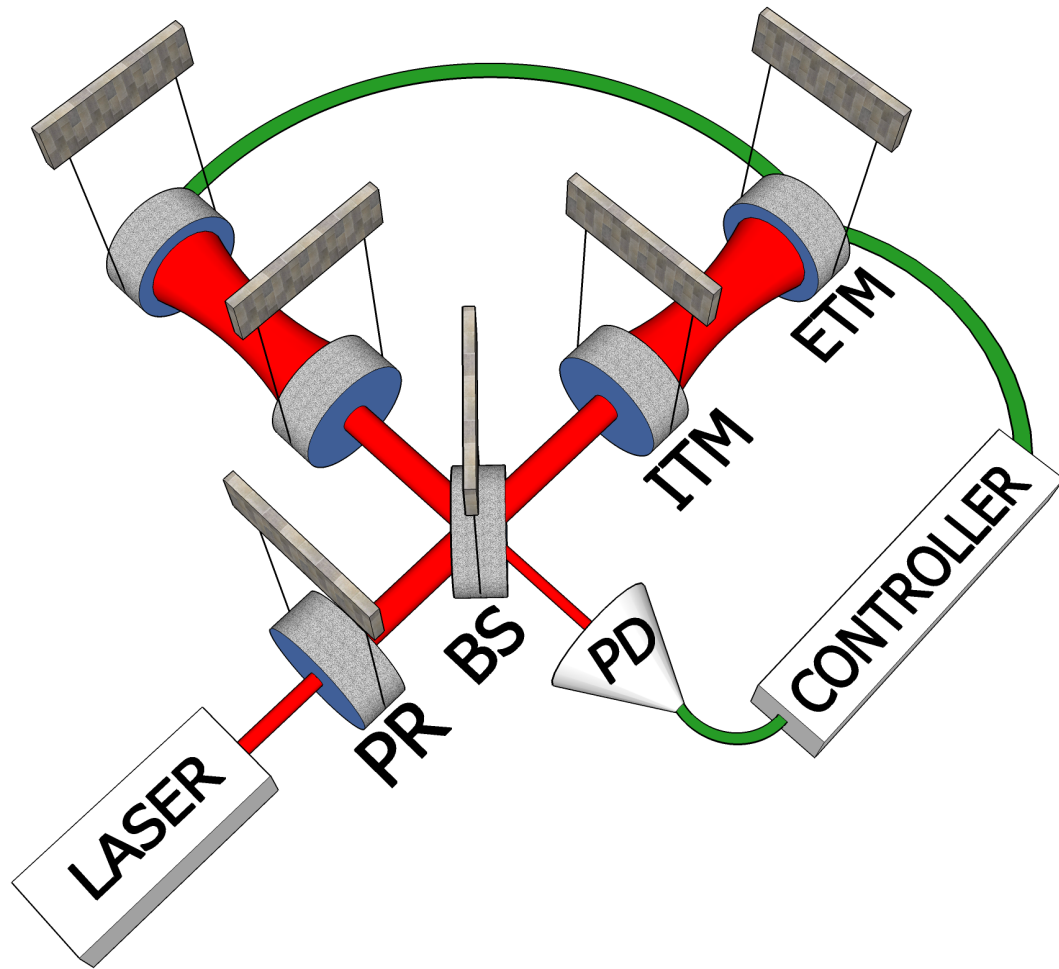**Figure 4-8:** Optical layout of a LIGO interferometer. Light reflected from the two Fabry-Perot cavities formed by input and end mirrors, $M_1 - M_4$, is recombined at the beam splitter (BS). To control the differential degree of freedom, an optical signal proportional to mirror displacement is measured on the photodetector (PD), and fed back as a differential force on the mirrors, after filtering to form restoring and damping forces.

from a vibration-isolated platform on a fine wire to form a pendulum with resonant frequency $\Omega_m = 0.74$ Hz, in order to shield it from external forces and to enable it to respond to a gravitational wave as a mechanically free mass above the natural resonant frequency. To minimize the effects of laser shot noise, the interferometer operates with high power levels: approximately 400 W of laser power of wavelength 1064 nm is incident on the beam splitter, resulting in over 15 kW of laser power circulating in each arm cavity.

The detector is sensitive to changes in relative mirror displacements of about 10^{-18} m in a 100 Hz band centered around 150 Hz. It is this low noise level which allows for the preparation of low-energy states for the oscillator mode considered next.

The four mirrors of the LIGO interferometer (figure 4-8) are each an extended object with a displacement x_i $(i = 1, \ldots, 4)$ defined along the optical beam axis. While all longitudinal and angular degrees of freedom of the mirrors are actively controlled, we limit our discussion to the differential arm cavity motion, which is the degree of freedom excited by a passing gravitational wave, and hence designed to be the most sensitive to mirror displacements. This mode corresponds to the differential motion of the centers of mass of the four mirrors, $x = (x_1 - x_2) - (x_3 - x_4)$, and has a reduced mass $m = 2.7$ kg.

A signal proportional to differential length changes is measured at the antisymmetric output of the beam splitter, as shown in figure 4-8. This signal is filtered by a servo compensation network before being applied as a force on the differential degree of freedom, by voice coils that actuate magnets affixed to the mirrors.

4.6.2 Servo spring

In order to synthesize a restoring force and a damping force, we wish to apply a feedback kernel of the form

$$K_f(\Omega) \approx m\Omega_{\text{eff}}^2 + im\Omega\Gamma_{\text{eff}} \tag{4.25}$$
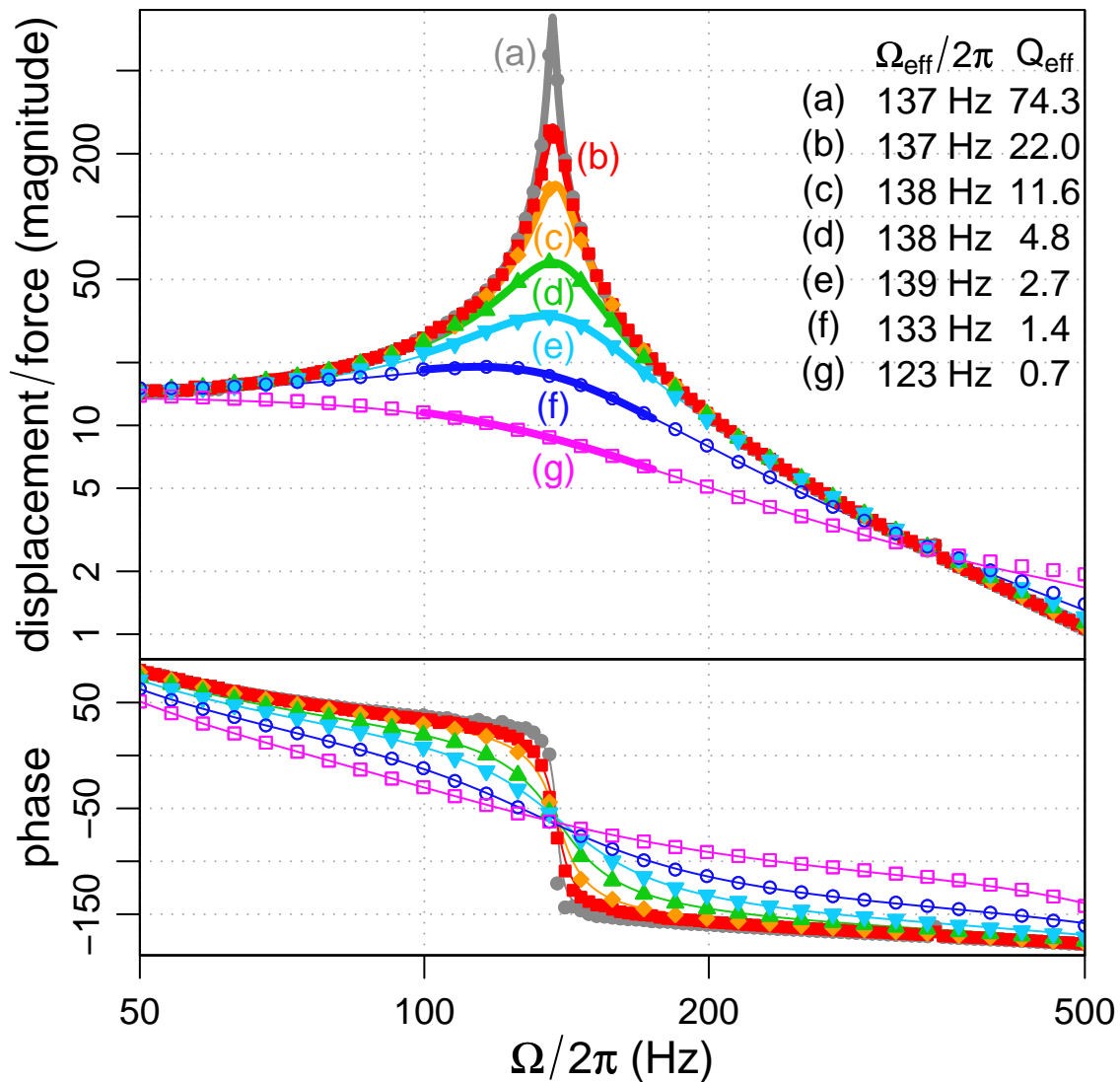
Figure 4-9: Response function of mirror displacement to an applied force, for various levels of damping. The points are measured data, the thin lines are a zero-parameter model of the complete feedback loop, and the thick lines spanning the resonance are fitted Lorentzians, from which the effective resonant frequency and quality factor are derived for each configuration.

with Ω_{eff} and Γ_{eff} much larger than Ω_m and Γ_m, respectively, such that the modified dynamics of x are given by a damped oscillator driven by random forces, as in equation (4.17). This feedback creates an electro-optical potential well in which the mirrors oscillate.

In LIGO, we can modify the existing servo control system that holds the interferometer on resonance, so that it convolves the position-dependent PDH signal with filter functions approximating the real and imaginary parts of K_f given by equation (4.25). However, the LIGO feedback system incorporates additional filters and propagation delays that cause deviations from the ideal damped spring. For example, at frequencies below 100 Hz, the magnitude of $K_f(\Omega)$ sharply increases, in order to suppress seismically driven motion; while above a few kilohertz, it is precipitously reduced, to prevent the control system from feeding shot noise back onto the mirrors.

Nonetheless, in the frequency band important for this measurement (near the electro-optical resonant frequency), the feedback is well approximated by a spring and damping force, as shown in figure 4-9.

4.6.3   Analysis and results

Note that the output signal x_{meas} measures the center of mass motion with an additional sensing noise, rather than x alone (see equation (4.14)). In order to establish a bound on the true mirror motion x, the limiting sources of noise must be considered.

If external force noise dominates ($\widetilde{F} \gg K_f(\Omega)\widetilde{x}_S$), then $x_{\text{meas}} \approx x$, and the measured signal corresponds to the center-of-mass motion. However, in the case that sensing noise dominates (that is, $K_f(\Omega)\widetilde{x}_S \gg \widetilde{F}$), then a correction factor must be applied to the measured signal to recover the center-of-mass motion. Taking equations (4.14) and (4.17), in the limit that $F = 0$, we find that

$$\widetilde{x} = \frac{K_f(\Omega)}{m\Omega^2}\widetilde{x}_{\text{meas}} \tag{4.26}$$

When $K_f(\Omega)/(m\Omega^2) \gg 1$, the measured noise $\widetilde{x}_{\text{meas}}$ may be arbitrarily suppressed by the feedback; however, the mirror motion will reach a finite level as limited by the

sensing noise $\widetilde{x}_S$. This "squashing" effect has been explored previously [117, 113]. It is important to correct for this effect in order to avoid underestimating the mirror motion.

In LIGO, the levels of each noise $\widetilde{x}_S$ and $\widetilde{F}$ are not precisely known. However, we can make a conservative correction by applying a factor $\max\left(1, K_f(\Omega)/(m\Omega^2)\right)$ to determine the worst possible center-of-mass motion, thereby accounting for the fact that the servo can inject noise back onto the oscillator.

We may then determine the effective temperature of the mode according to equation (4.9). We apply the above-mentioned correction to obtain an upper bound for x_{rms}^2, as follows:

$$x_{\mathrm{rms}}^2 = \int \max\left(1, \frac{K_f(\Omega)}{m\Omega^2}\right)^2 S_{x_{\mathrm{meas}}}(\Omega)\, d\Omega \tag{4.27}$$

Here $S_{x_{\mathrm{meas}}}$ is the single-sided power spectral density of the measured motion x_{meas}. Note that we *must* limit the frequency band of this integral, because we cannot measure the mirror's motion at arbitrarily high frequencies, and including all the high-frequency sensing noise in the integration would cause it to diverge.

Finally, the corresponding occupation number may be determined by

$$N_{\mathrm{eff}} = \frac{k_B T_{\mathrm{eff}}}{\hbar \Omega_{\mathrm{eff}}} \tag{4.28}$$

Figure 4-10 shows the amplitude spectral density of mirror displacement, with the sensing noise correction factor already applied, for varying levels of cold damping. To determine the effective temperature of the mode from these data, we must estimate the effective frequency Ω_{eff} and the root-mean-square displacement fluctuation x_{rms}.

To do so, first we drive the differential mirror motion and measure the response, shown in figure 4-9. These response functions are fit to a damped oscillator model; Ω_{eff} and Q_{eff} are products of the fit.

Then x_{rms} is computed by integrating the spectrum according to equation (4.27), in the band from 100 to 170 Hz. To correct for the finite integration band, we scale the
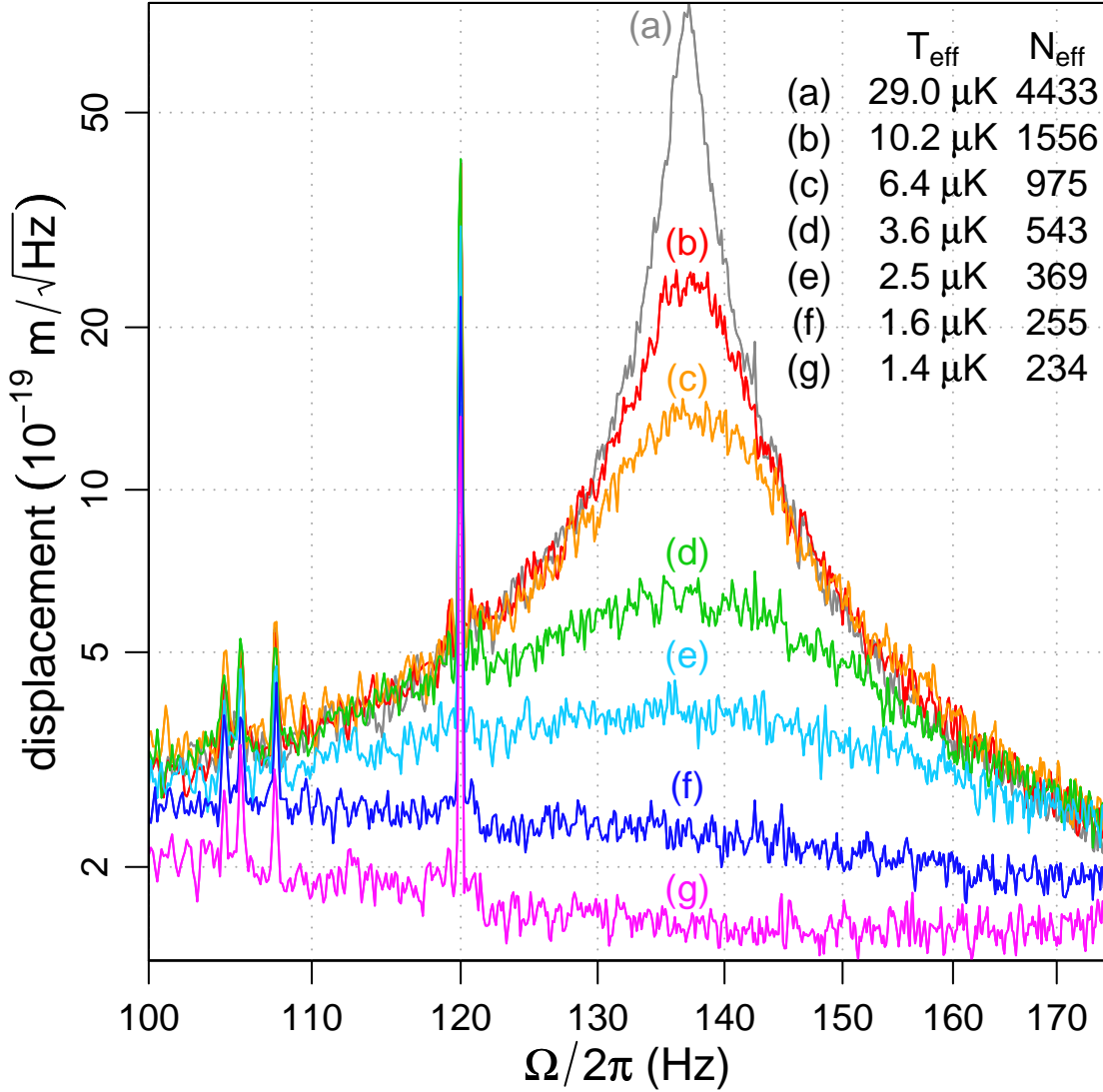
	T_{eff}	N_{eff}
(a)	29.0 µK	4433
(b)	10.2 µK	1556
(c)	6.4 µK	975
(d)	3.6 µK	543
(e)	2.5 µK	369
(f)	1.6 µK	255
(g)	1.4 µK	234

Figure 4-10: Amplitude spectral density of displacement in the frequency band of integration. The curves (from highest to lowest) were produced by applying increasingly strong cold damping to the oscillator, corresponding to the measurements of figure 4-9. The depression in the lowest curve is due to the shape of the background noise spectrum; the effects of the servo are corrected for according to equations (4.14) and (4.27). The narrow line features between are mechanical resonances of auxiliary subsystems, and a 120 Hz power line is also visible.

result by setting our measured spectrum integral equal to the spectrum of a thermally driven oscillator (given by equation (4.18)) integrated over the same frequency band.

In this way, we measure a minimum effective temperature $T_{\text{eff}} = 1.4 \pm 0.2 \ \mu\text{K}$, corresponding to thermal occupation number $N_{\text{eff}} = 234 \pm 35$. Systematic error of 15% in the calibration dominates statistical error in these uncertainty estimates.

4.6.4 Future prospects

In this work, we have established a new method by which interferometric gravitational wave detectors, designed as sensitive probes of general relativity and astrophysical phenomena, might also become sensitive probes of macroscopic quantum mechanics.

An interesting question arises as to whether this technique can lead to ground state cooling of the interferometer mirrors. It is straightforward to adapt the simplified treatment of section 4.5 to the case of a servo spring. Moreover, a detailed calculation [42] has been performed, showing that the continuous displacement measurement required for feedback does in fact introduce a small additional term to the uncertainty relation for the oscillator position and momentum fluctuations, due to measurement-induced steady state decoherence.

A sub-SQL noise spectrum in the vicinity of Ω_{eff} can circumvent this limit. Such a spectrum can be achieved by injection of a squeezed state into the antisymmetric port of the interferometer, for example. As classical noises are suppressed, and the squeezing becomes stronger, the oscillator should approach a pure state.

Recall that a major upgrade of the LIGO detectors is presently underway. Advanced LIGO, expected to be completed in 2014, should give a factor of 10 to 15 improvement in displacement sensitivity relative to that of the detector used for this work (with a concomitant factor of 4 increase in mass). In Advanced LIGO, the circulating laser power will increase to 800 kW, permitting strong restoring forces to be generated optically. The Advanced LIGO detectors are expected to operate near the SQL.

Future detectors will surpass the SQL, and in so doing, enable compelling experimental demonstrations of quantum theory at the macroscale, involving kilogram-scale test masses with kilometer-scale separations [99, 42, 76].
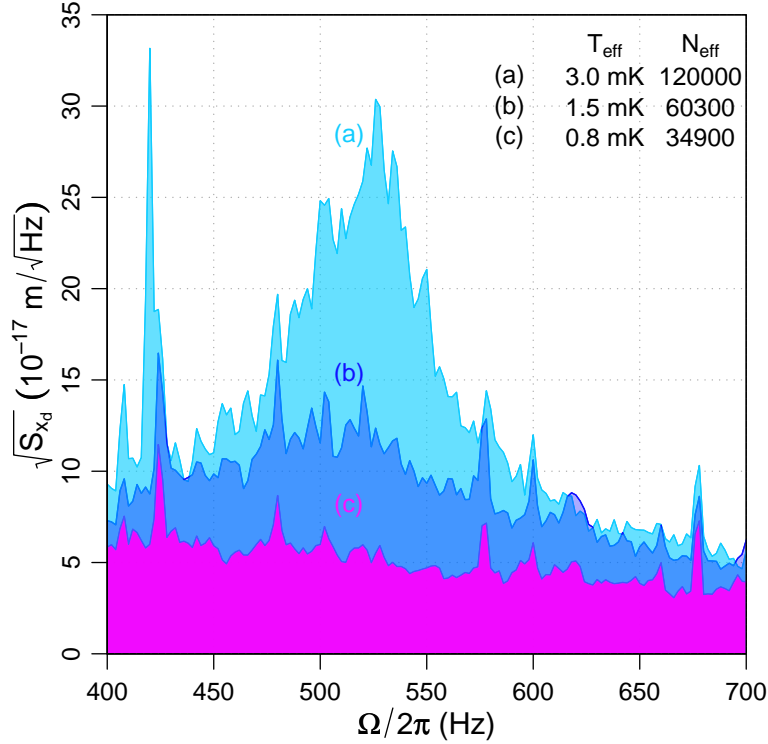
Figure 4-11: Cooling as a benchmark for the ponderomotive interferometer.

4.7   Cooling as a benchmark

The trapping and cooling technique that was introduced in the previous section can be applied to any instrument capable of displacement actuation and sensing. After the series of experiments described in sections 4.2 and 4.4 were completed, the ponderomotive interferometer was upgraded to its full Fabry-Perot Michelson configuration, as set forth in chapter 3. Taking advantage of its improved noise floor (which was mainly due to the cancellation of laser noise in the Michelson), we used the optimal feedback cooling strategy to obtain nearly a factor of ten reduction in temperature, relative to the single-cavity result found in section 4.4. The present limits to cooling in our experiment can be attributed to the 1-gram mirror suspensions, as we will see in the next chapter. Data from this benchmark cooling run are plotted in figure 4-11.

Chapter 5

Radiation pressure and thermal noise

In this chapter, we will investigate suspension thermal noise, which is the primary noise mechanism that currently limits the performance of the ponderomotive interferometer. This effect dominates the interferometer's displacement noise spectrum throughout a broad frequency band, and has so far prevented us from observing quantum backaction in the system.

In addition to being the highest priority problem to solve in future iterations of the experiment, our thermal noise limited spectrum represents an opportunity to validate our understanding of an important noise mechanism. Suspension thermal noise is of interest in a wide range of mechanical instruments, including other quantum opto-mechanics experiments, reference cavities for laser frequency stabilization, and gravitational wave interferometers. We find excellent agreement of our spectrum with theory in a regime where, to our knowledge, this type of noise had not been previously observed.

5.1   Thermal noise

Damping and thermal noise are two sides of the same coin. Both phenomena occur whenever a system is allowed to exchange energy with its environment. Damping is

what we observe when the system is initially very excited: energy leaks out of the system and is dissipated as heat in the environment. Eventually an equilibrium is reached between this process, and the small influx of energy due to random fluctuations of the environment that act to excite the system.

The Fluctuation Dissipation Theorem, derived by Callen and Welton [32], is the conceptual linchpin that defines the precise relationship between the equilibrium level of thermal noise and the strength of the damping. It can be written in the following form:

$$S_F^{(T)}(\Omega) = 4k_B T R(\Omega) \tag{5.1}$$

where $S_F(\Omega)$ is the power spectrum of force noise that acts on the system, and $R(\Omega)$ is the resistance, which characterizes the damping.

For example, in an electrical circuit, equation (5.1) gives a description of Johnson noise, the noisy electromotive force produced by a resistor R at temperature T. In a mechanical system, the same thermodynamics are at work, although the concept of "resistance" may not be familiar in the context of mechanics. It is given by the real part of the mechanical impedance $Z(\Omega) = 1/(-i\Omega\chi(\Omega))$, where $\chi(\Omega)$ is the mechanical susceptibility (transfer function of force to displacement). Note that the thermal displacement noise spectrum can be obtained from equation (5.1) by inserting the susceptibility, as follows:

$$
\begin{aligned}
S_x^{(T)}(\Omega) &= |\chi(\Omega)|^2 S_F^{(T)}(\Omega) \\
&= \frac{4k_B T R(\Omega)}{\Omega^2 |Z(\Omega)|^2} \\
&= \frac{4k_B T}{\Omega^2} \mathrm{Re}\left\{\frac{1}{Z(\Omega)}\right\}
\end{aligned}
\tag{5.2}
$$

The quantity $1/Z(\Omega)$ is known as the *admittance.*

Using this theorem, we can translate measurements of the mechanical losses found in the interferometer into estimates of its thermal noise limited sensitivity. Likewise, displacement measurements that reach the thermal noise limit can be used to inform us about the dissipation mechanisms at work in the interferometer.

A widely used, dimensionless parametrization of damping is the *loss angle* $\phi(\Omega)$, which extends an oscillator's spring constant to include a small imaginary part:*

$$K_m(\Omega) = m\Omega_m^2 \left(1 - i\phi(\Omega)\right) \tag{5.3}$$

The loss angle can take on an arbitrary frequency dependence, which allows it to describe a wide array of dissipation mechanisms. It has a simple relationship with the resistance: $\phi(\Omega) = \dfrac{\Omega}{m\Omega_m^2} R(\Omega)$.

Ordinary *viscous* damping corresponds to a loss angle $\phi(\Omega) = \Gamma_m \Omega / \Omega_m^2$, linearly proportional to frequency. However, an alternative form of damping was introduced by Kimball and Lovell [74], and is expected to describe the internal friction of a mechanical structure such as a mirror suspension. This *structural* damping is what remains after all external effects (such as air friction or eddy current damping) are made negligible. Structural damping is characterized by a loss angle $\phi(\Omega) = \Gamma_m / \Omega_m = 1/Q_m$, independent of frequency (at least across some finite band of frequencies).

Near the resonant frequency Ω_m, the effects of viscous and structural damping are almost indistinguishable. However, away from resonance, their thermal noise power spectra have different slopes (see figure 5-1). They diverge by the factor Ω/Ω_m, in accordance with the Fluctuation Dissipation Theorem. This difference is very important in mechanical instruments where measurements are made off-resonance, including seismometers, gravitational wave detectors, and the ponderomotive interferometer. In any such device, the nature of the damping mechanism plays a pivotal role in determining the thermal noise limited sensitivity.

Nonetheless, to our knowledge, only a few measurements of suspension thermal noise exhibiting structural damping have been reported until now. In those cases it was observed at very low frequencies, below 10 Hz [103, 84, 11]. By contrast, the ponderomotive interferometer is sensitive to suspension thermal noise across a wide frequency band of 80–5000 Hz. Previous measurements of thermal noise in this band have been limited by the noise of the optical coatings, rather than the noise of the

---

*The extra factor in the spring constant is sometimes written as $(1 + j\phi(\Omega))$, with a sign flip in the imaginary part, which is as it should be if one propagates in time with $e^{j\Omega t}$ rather than $e^{-i\Omega t}$.
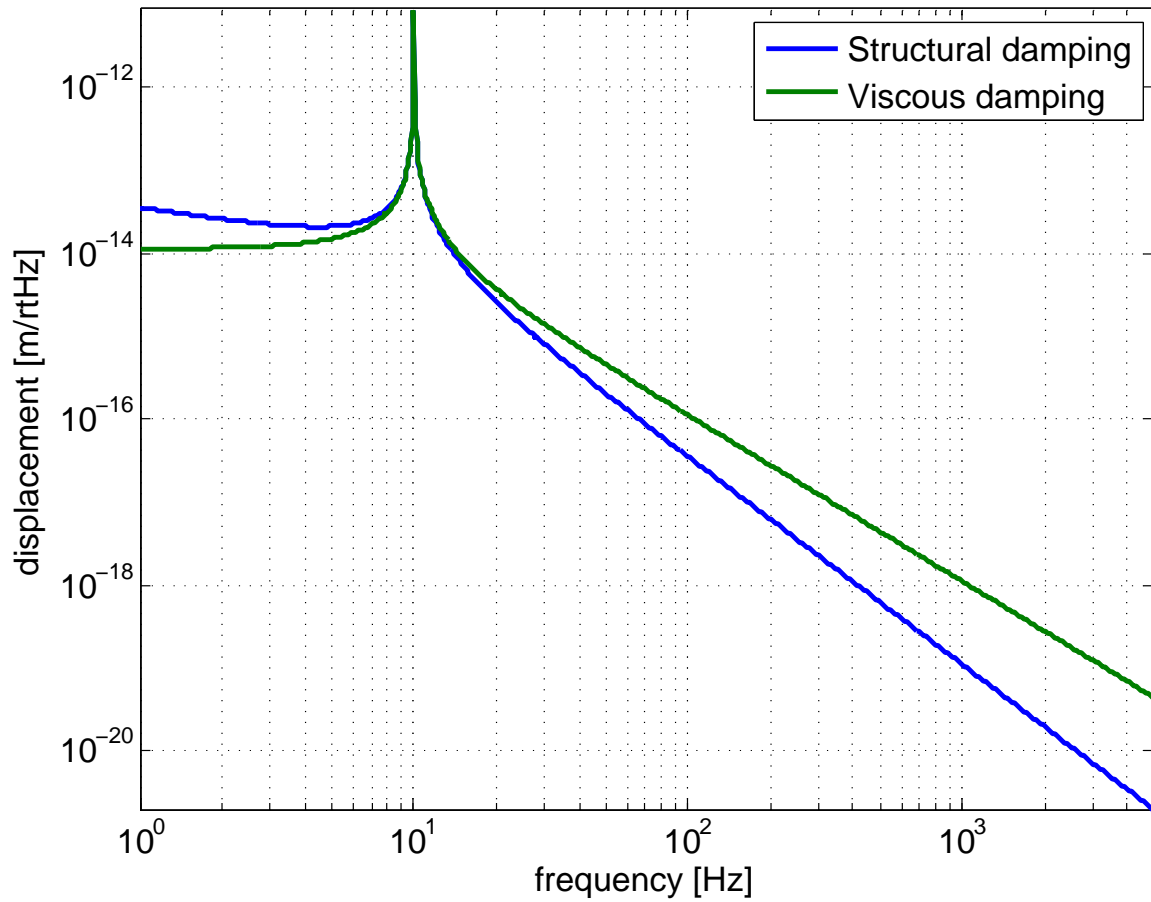
Figure 5-1: Thermal displacement noise amplitude spectra due to viscous and structural damping (assuming a 10 Hz oscillator of Q 10^6 and reduced mass 0.5 gram at temperature 300 K), showing the divergent noise above and below resonance. The viscous damping curve roughly coincides with the level of radiation pressure noise achievable in the experiment.

suspension itself [67, 104, 19].

We have verified our interpretation of the interferometer's noise floor, by using it to fit a model of thermal noise due to structural damping in the 1 gram end mirror suspension. The calculation follows the method described by Levin [82]. This method was implemented in the finite element analysis software COMSOL by Abraham Neben, who also developed exquisitely detailed 3D models of the end mirror suspension. In section 5.1.1 we review Levin's method. In section 5.1.2, we discuss the properties of the end mirror suspension. Details of the finite element computation and fitting procedure are found in section 5.1.3]. In section 5.1.4 we consider the implications of this result for future iterations of our experiment. The results discussed here have been presented in reference [101].

5.1.1 Levin's method

To calculate the thermal noise spectrum using equation (5.2), we need to know the real part of the admittance $1/Z(\Omega)$. For idealized models such as the simple harmonic oscillator, it is straightforward to derive the equation of motion and find the admittance analytically.

But an exact analytic treatment is not practical for a real system like a mirror suspension, which has many normal modes of oscillation that contribute to the thermal noise limit. An approximate method for a multi-mode system is to apply the Fluctuation Dissipation Theorem to the normal modes individually (treating each one as an independent harmonic oscillator), and thus to obtain thermal noise power spectra corresponding to each mode. The resulting spectra are simply added up to estimate the total noise. The assumption underlying this approach is that the noise of distinct modes is uncorrelated, and can be summed incoherently. However, this assumption may not be justified, particularly when the losses are not distributed homogeneously throughout the mechanical structure.

Levin's "direct approach" [82] is capable of accurately estimating the thermal noise spectrum of a mirror surface's displacement, as sampled by an incident laser beam. To use this method, we must work out the mirror's response to a force applied on its

surface. The force is sinusoidal in time with frequency Ω and peak amplitude F_0, and it is spatially distributed across the mirror's face with a profile matching that of the laser beam. We then compute the average power, $W_{\text{diss}}(\Omega)$, that is dissipated in the mirror as a result of the applied force. Finally, we use the prescription

$$\text{Re}\left\{\frac{1}{Z(\Omega)}\right\} = \frac{W_{\text{diss}}(\Omega)}{F_0^2} \tag{5.4}$$

and equation (5.2) to obtain the thermal displacement noise power spectrum.

Levin's approach is relatively easy to translate into a numerical method using finite element analysis. In this way, it can correctly account for all known information about the geometry and material properties of each component of a mirror suspension, yielding highly accurate results. However, when interpreting those results, it can still be valuable to think in terms of normal modes. For instance, the thermal noise of an individual mode may be dominant in a particular frequency band, and knowing which mode is the culprit may suggest a route to mitigating the noise. This has proven to be the case in our analysis of the thermal noise of the ponderomotive interferometer's 1 gram end mirror suspension.

5.1.2 End mirror suspension as built

The overall experimental setup used to obtain thermal noise limited displacement spectra is described in chapter 3. Central to the results of this chapter are the 1 gram mirror oscillators, which are suspended from fused silica fibers as illustrated in figure 5-2. Each fiber is 40 mm in length, and tapers from a maximum diameter of 3 mm to a minimum of ~ 150 μm. A thicker region, called the "ear", is located at the bottom, and is about 10 mm long and 1.5 mm in diameter. The shape of the ear was informed by the need for a steep spatial gradient at the transition between the small diameter fiber and the large diameter ear, which allows for better decoupling of ear and mirror motion. See figure 5-3 for a close-up view of the ear region. The ears are bonded to the mirror with Vac-Seal epoxy (Tra-Con).

The purpose of the tapering fibers is to minimize the thermal noise of the funda-
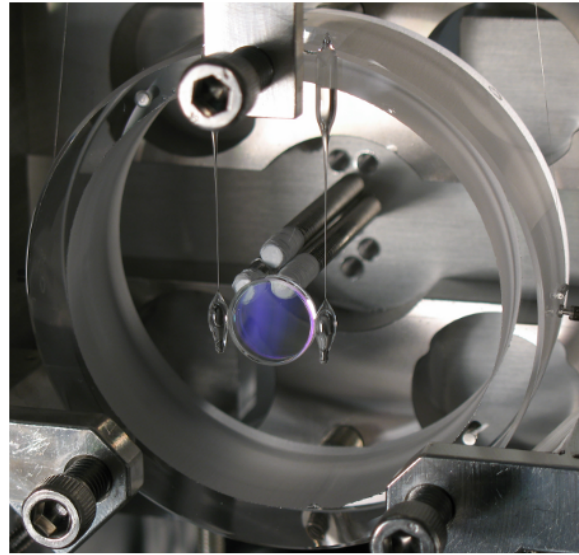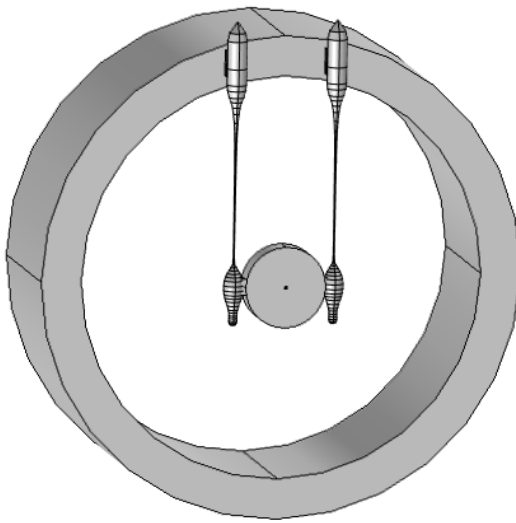
Figure 5-2: Left panel: Finite element model of a 1 gram mirror suspended by fused silica fibers, showing the fibers that taper in the middle and are thicker at the ends where the epoxy bonding is done. The 1 gram mirror oscillator is attached to a fused silica ring that is itself suspended as a pendulum. This double pendulum system provides greater isolation from seismic noise, but has little impact on the accuracy of the model due to the much greater mass of the outer ring. Right panel: photograph of the 1 gram mirror suspension.
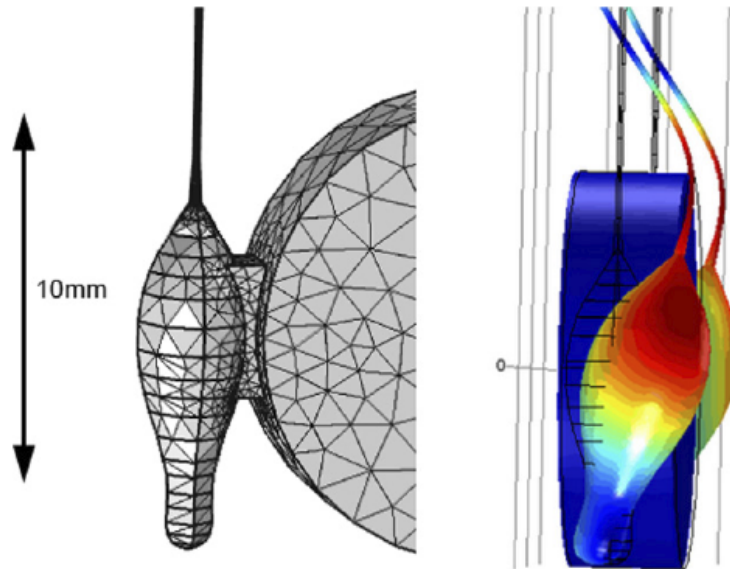

Figure 5-3: Left panel: Close-up view of the finite element mesh of the 1 gram mirror suspension. The model was generated from high-resolution photographs of the mirror and ears. Right panel: image of the displacement of the twisting ear mode, with blue being least displaced and red being most displaced.
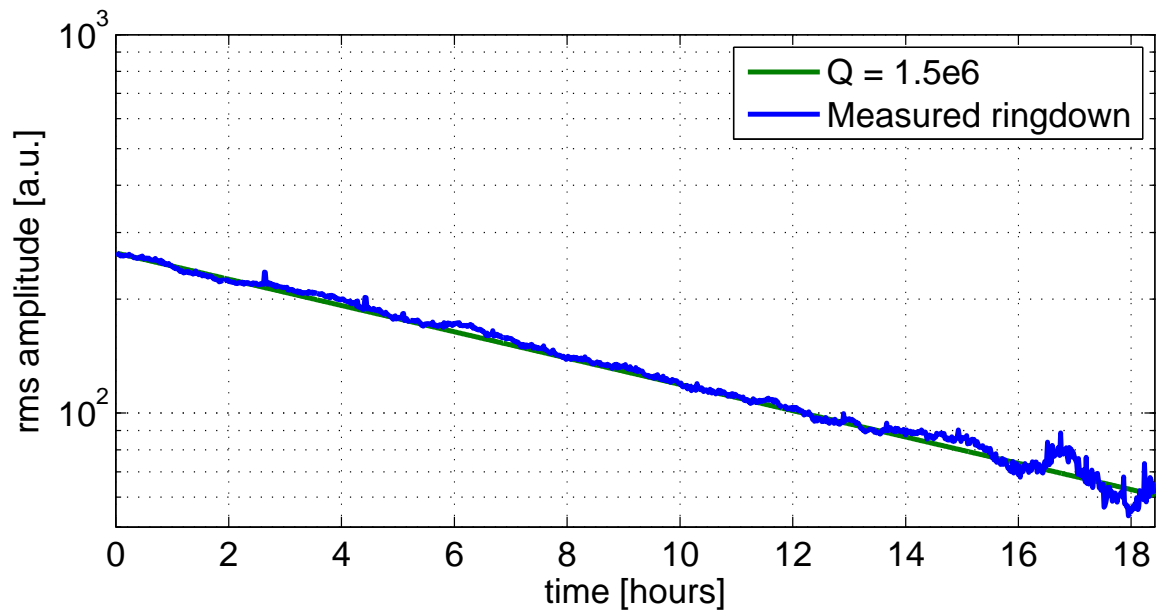
Figure 5-4: Ringdown measurement of the quality factor of the 10 Hz longitudinal mode of the end mirror suspension, showing $Q \sim 10^6$.
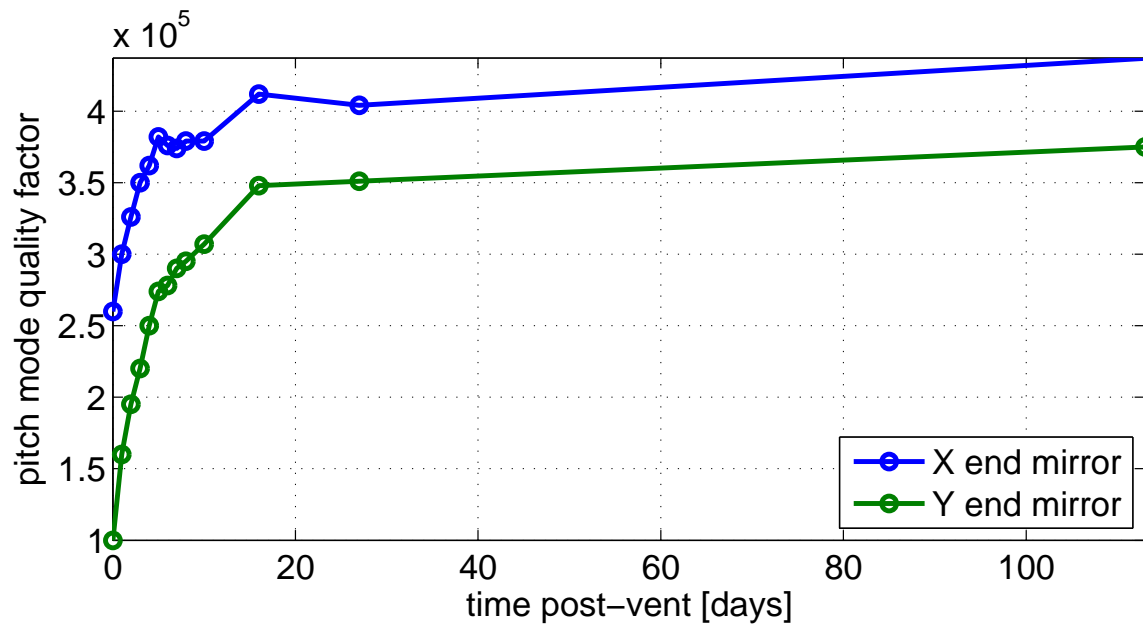

Figure 5-5: Pitch mode quality factors, degraded after a vent, take a few weeks to recover to their typical values.

mental mode of oscillation (which occurs at about 10 Hz), by ensuring that it stores energy mostly in the pristine fused silica near the middle of the fiber, and not in the lossy epoxy at either end. Quality factors of greater than 10^6 are measured for the 10 Hz mode (see figure 5-4), which would imply that the thermal noise of this mode is far better than what is required to observe the quantum backaction.

However, the 1 gram mirror's yaw mode (near 40 Hz) and pitch mode (near 70 Hz) exhibit degraded losses. Quality factors are $\lesssim 5 \times 10^5$, with the pitch mode Q superior to that of the yaw mode. The losses are observed to evolve over time: they are at their worst when the vacuum chamber has recently been vented, and slowly recover afterward, as shown in figure 5-5. We speculate that this process is related to absorption of water by the Vac-Seal epoxy from the air during a vent, and subsequent outgassing while under vacuum.

We also observed a family of modes above 30 kHz, with quality factors on the order of 100. These modes can be excited by driving the actuators of the end mirror suspension, confirming that they are modes of that suspension.

Finally, we observed a displacement noise floor with a $1/f$ power spectrum, spanning a broad frequency band from 80–5000 Hz. This noise was shown to be unrelated to the readout and actuation chains, and unexplained by any known coupling to the noise of the laser, or the noise of auxiliary feedback loops in the interferometer. In the next section, finite element analysis is used to confirm that 30 kHz bending modes of the ear-mirror epoxy bond can account for the observed noise floor.

5.1.3 Thermal noise finite element analysis

The finite element method is an approach to solving for continuum dynamics in various physical scenarios by discretizing the geometry. We perform finite element simulations with the COMSOL Multiphysics package, using its Structural Mechanics module. With that software, we model the 3D geometry, then implement the Levin approach. We apply a Gaussian load to the mirror face, and solve for the steady-state mirror response to the load oscillating at a set of frequencies $\{\Omega\}$, yielding the complex admittance $1/Z(\{\Omega\})$ directly. See Table 5.1 for material parameters used in the

Property	Value for fused silica	Value for Vac-Seal epoxy
Density	2.20 g/cm^3	1.01 g/cm^3
Young's modulus†	73.1 GPa	2.75 GPa
Poisson's ratio	0.17	0.25
Loss angle‡	3×10^{-7}	0.035

Table 5.1: Material properties and their assumed values.

simulations.

Using the measured displacement spectrum, we fit for the loss angle of the epoxy, and arrived at $\phi_{\text{epoxy}} = 0.035$. This value results in excellent agreement between our experimental data and the output from the model, as shown in figure 5-6. We take this result as confirmation that our displacement noise floor is dominated in the 80–5000 Hz band by structural thermal noise.

The 80–200 Hz band is in the above-resonance "wing" of the 80 Hz pitch mode. If all the pitch modal energy were in the very low loss fused silica, then we would expect to measure $Q = 1/\phi_{\text{fused silica}} \sim 3 \times 10^6$. However, we measure only $\sim 5 \times 10^5$, indicating both that pitch thermal noise is setting our noise floor in that band, and that epoxy loss is dominating that noise.

In the 200–5000 Hz band the spectrum shows the characteristic $1/f$ below-resonance thermal noise power spectrum of a structurally damped oscillator, which is well reproduced by simulations. The modes responsible for this noise are the bending modes of the ear-mirror joint, with resonant frequencies starting around 30 kHz. (See figure 5-3, for an example of one such ear-mirror bending mode.)

5.1.4 Thermal noise mitigation

Various schemes have been presented to reduce the level of thermal noise in an interferometer [75, 145, 73, 98], relying either on carefully tuned passive cancellations or multiple measurements to disentangle the thermal noise from displacement signal.

---

†Value for Vac-Seal is per manufacturer specification for comparable epoxies.

‡All fused silica loss occurs in the fibers where surface losses dominate. For fibers with minimum diameter $\sim 150\ \mu$m, Gretarsson and Harry find the value given here for fused silica [63]. Concerning the value for Vac-Seal, see the discussion in the text.
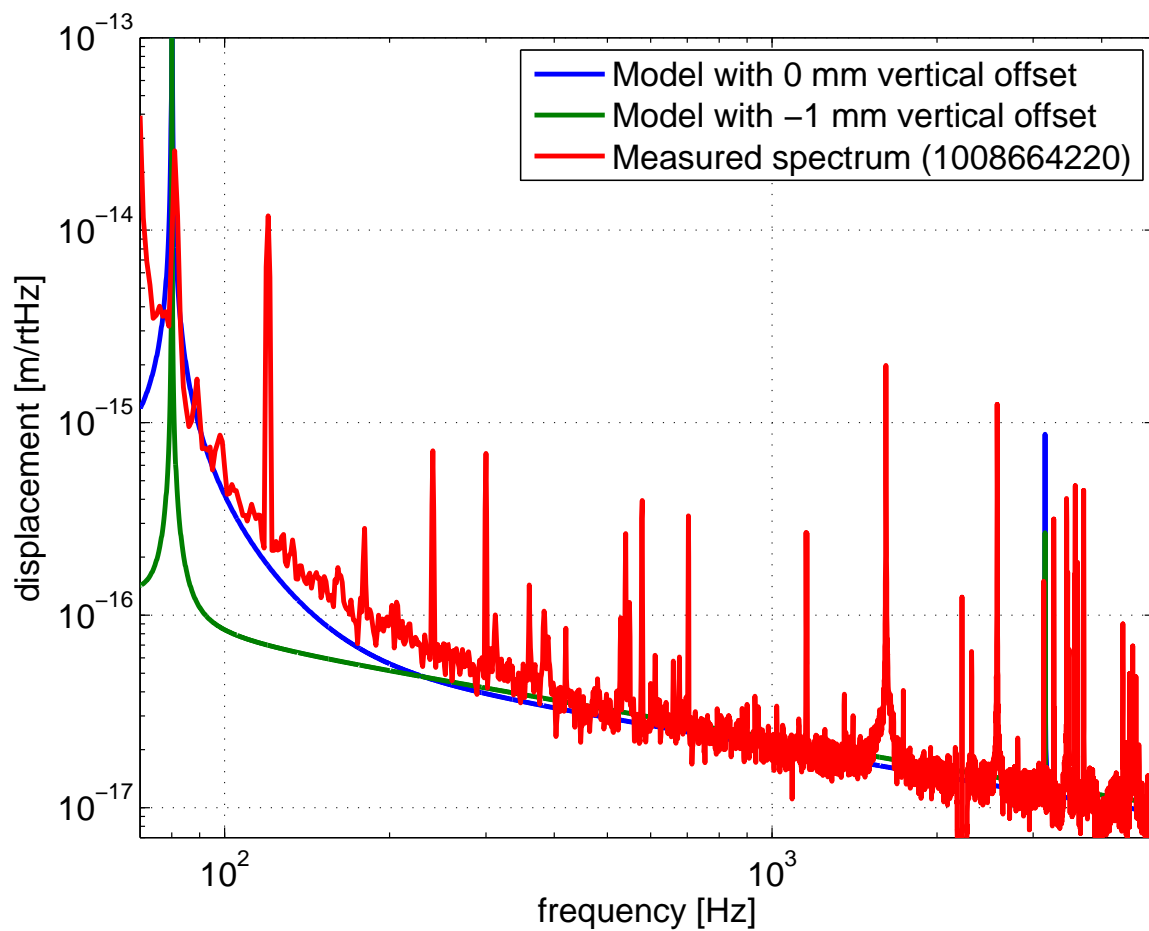
Figure 5-6: Measured displacement sensitivity compared with the thermal noise prediction from finite element analysis with the normal mode method, including a 0 and −1 mm vertical beam offset from the mirror center. Non-uniform optical losses over the mirror surface have prevented us from exploring the full space of beam offsets in the experiment, but this limitation should be remedied in the upgrade now underway.

Figure 5-7: Predicted thermal noise for alternate, square-profile ear geometries with a chopped mirror, showing the improved performance relative to radiation pressure noise. Inset: rendering of a chopped mirror suspended with 3×3 mm square ears.

Our modeling results suggest several simpler geometric ways to lower our noise floor.
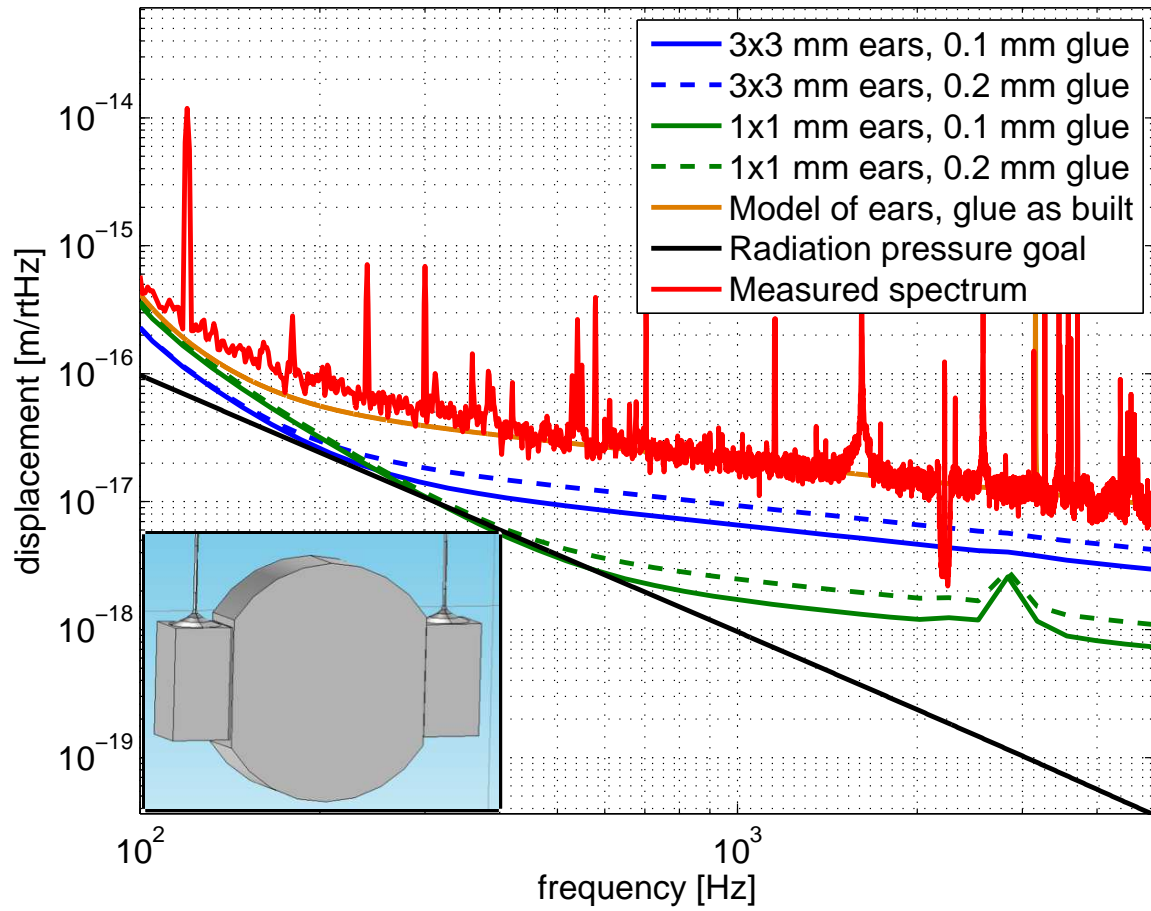
In the 80–200 Hz band, the measured spectrum is dominated by the thermal noise from the pitch mode of the oscillator. Introducing a vertical offset of the incident laser beam, shifting it ≈ 1 mm from the center of the mirror, places the beam near the node of the pitch mode. This offset should decrease the sensed pitch thermal noise (by increasing the modal mass), as depicted in Figure 5-6.

Above 200 Hz, the thermal noise of the mirror-ear bending modes takes over. As the loss angle ϕ_{epoxy} is 5 orders of magnitude larger than $\phi_{\mathrm{fused\ silica}}$ (for $\sim 150\ \mu$m fibers [63]), it is the epoxy that dominates both the pitch and the mirror-ear bending thermal noise. To minimize the effect of this thermal noise in our measurement band, we investigated alternative mirror-ear geometries to maximize the strength of the ear-mirror bond per amount of epoxy. By maximizing this quantity, we redistribute the thermal noise of the mirror-ear modes to higher frequencies, out of the measurement band. This quantity of merit is optimized in the case of plane-on-plane contact, and so we propose a design that incorporates ears with square cross-section, and "chopped" mirrors with flattened regions on the circular edge. Figure 5-7 shows a model of this square-ears/chopped-mirror geometry, together with the predicted thermal noise for variations on that geometry. We expect these square ears to be the most expedient path forward, and are pursuing this design for the next iteration of the end mirror suspension. The design is also compatible with other adhesives such as silicate bonding [132].

5.1.5   Summary

We have experimentally demonstrated and theoretically analyzed the structural thermal noise-limited performance of a 1 gram mirror oscillator, finding excellent agreement between the model and the measurement. We have also proposed some avenues to reduce the thermal noise floor in this experiment. The observation of off-resonance thermal noise has importance for a broad class of experiments in cavity optomechanics and gravitational wave interferometry. Accurate modeling of these complex structures depends on detailed knowledge of their geometry and material properties, but lets

us better understand and optimize their mechanical design. The optimizations we have presented should permit our experiment to enter the quantum backaction limited regime.

Chapter 6

Ponderomotive entanglement

In this chapter, we turn our attention to future goals for the ponderomotive interferometer, after it has entered the quantum backaction regime. A longstanding goal has been to demonstrate that the interferometer can serve as a source of squeezed light. In fact, this is the purpose for which the experiment was originally designed [40]. Here, we will propose another application: it should be possible to employ the optical trap configuration, discussed in chapter 4, as a novel source of *entangled* light. This proposal was published in reference [142].

6.1   Background

Entanglement is one of the cornerstones of quantum mechanics, having first emerged in the context of the famous EPR paradox [47]. It continues to be a conceptually challenging phenomenon that plays an important role in fundamental tests of quantum theory. Moreover, it has found many new applications in the field of quantum information, including cryptography and teleportation.

It is anticipated that the radiation pressure coupling of light incident on a movable mirror can be used to entangle the mirror with the optical field [20, 88], or with other resonators [87, 143, 112, 114], while also allowing the system to act as a source of entangled light [59, 56]. Analogous effects are possible when capacitive coupling is substituted for the radiation pressure [16]. Recent predictions indicate that such

effects may be observed using micromechanical devices within experimentally feasible parameter regimes [49, 136, 109].

Meanwhile, the improving sensitivity of gravitational-wave interferometers is beginning to open a new experimental regime for macroscopic quantum mechanics, and promises to reveal quantum features such as squeezing and entanglement of their mirrors' motion [99]. In addition to the profoundly macroscopic size of these systems, another distinctive feature of this regime is that radiation pressure effects, particularly the optical spring [27, 29, 38, 128, 96], can play a dominant role in the dynamics.

A good example of radiation pressure dominated dynamics is the stable optical trap presented in chapter 4. Recall that this technique exploits the optical restoring and damping forces of *two* laser fields detuned from cavity resonance — resulting in a stable, strong, and cold trap, where the mirror's thermal noise has undergone a great deal of optical dilution.

Motivated by these developments, we have evaluated the prospects for observing entanglement in the optical trap configuration. We concentrate on entanglement between the two output optical fields, i.e., the device's potential as a source of quadrature-entangled light. Since this type of entanglement places the least stringent demands on the quantum state of the mirror, we expect that it will be among the earliest to be demonstrated experimentally. We also note that the protocols previously developed to characterize non-mechanical entanglement sources [107, 130, 21] can be directly applied in this setting.

This chapter is organized as follows. In section 6.2 we offer a review of the logarithmic negativity entanglement measure. In section 6.3 we describe the dynamics of the stable optical trap in some detail, providing a quantum treatment of a cavity mirror coupled to two optical fields based on their Langevin equations, including thermal noise of the mirror coating. This leads to a simple and general formula quantifying the entanglement of the optical fields at the output, presented in section 6.4. The prospects for experimentally realizing this entanglement are considered in section 6.5, before concluding with section 6.6.

6.2 Entanglement criterion

Many of the best-known examples of entanglement in physics involve discrete systems, such as qubits. Moreover, the entanglement criterion we are about to describe (which is known as the logarithmic negativity) was originally defined for discrete systems, before being generalized to the case of continuous variables (such as the position and momentum of a particle). In what follows, we will briefly review this historical development.

6.2.1 Finite-dimensional entanglement

If we consider two qubits, labeled A and B, it is sometimes possible to describe the state of each qubit individually. For instance, both qubits may be in the state $|0\rangle$, so that the joint state $|\psi\rangle_{AB} = |00\rangle_{AB}$. In that case, the joint state is called *separable*. Represented symbolically, $|00\rangle_{AB} = |0\rangle_A \otimes |0\rangle_B$.

On the other hand, in quantum mechanics it is permissible to form a superposition of two separable states, such as: $|\psi\rangle_{AB} = \left(|00\rangle_{AB} + |11\rangle_{AB}\right)/\sqrt{2}$. This is one of the famous *entangled* Bell states, a joint state that does not admit separate identities for the states of its two constituent qubits.

However, there are similar-looking superpositions of separable states that *are* themselves separable. For instance, $\left(|00\rangle_{AB} + |01\rangle_{AB}\right)/\sqrt{2}$ separates into $|0\rangle_A \otimes \left(|0\rangle_B + |1\rangle_B\right)/\sqrt{2}$. Note that it is not always obvious at a glance whether a given joint state can be factorized in this way, especially for a higher-dimensional system. Deciding whether entanglement is present in some arbitrary joint state turns out to be a challenging problem.

Peres [111] made progress on this problem by deriving a necessary criterion for a density matrix to describe a separable state. This criterion was also shown by Horodecki [68] to be sufficient for 2×2 or 2×3 dimensional systems, and *not* sufficient in higher dimensions. The reasoning is as follows.

First, note that a separable joint density matrix $\boldsymbol{\rho}_{AB}$ can be written in the form $\boldsymbol{\rho}_{AB} = \sum_k p_k \left(\boldsymbol{\rho}_{A,k} \otimes \boldsymbol{\rho}_{B,k}\right)$, where $\boldsymbol{\rho}_{A,k}$ and $\boldsymbol{\rho}_{B,k}$ are themselves density matrices for

the subsystems A and B, and the probability weights $p_k \geq 0$ with $\sum_k p_k = 1$. Also, taking the transpose of a matrix does not change its eigenvalues, which for a valid density matrix are required to be non-negative. Therefore, the *partial* transpose of a separable joint density matrix, $\boldsymbol{\sigma}_{AB} = \sum_k p_k \left(\boldsymbol{\rho}_{A,k}^T \otimes \boldsymbol{\rho}_{B,k} \right)$, should continue to be a valid joint density matrix, with non-negative eigenvalues. But if $\boldsymbol{\rho}_{AB}$ is not separable, the partially transposed $\boldsymbol{\sigma}_{AB}$ may have a negative eigenvalue.

So the Peres-Horodecki criterion tells us to look for negative eigenvalues of $\boldsymbol{\sigma}_{AB}$. When we find one, we know that the state must be entangled. The sum of negative eigenvalues of $\boldsymbol{\sigma}_{AB}$ is known as the *negativity* $\mathcal{N}$; and the so-called *logarithmic negativity* [116] is $E_N = \log_2(2\mathcal{N} + 1)$. This entanglement measure is frequently used in the literature, and has several advantages: it is simple to compute, and possesses an operational interpretation [18].

6.2.2 Continuous-variable entanglement

Simon [131] figured out how the Peres-Horodecki criterion could be applied to continuous variable systems. The result uses the fact that, for continuous variables, transposing the density operator is equivalent to time reversal $(p \rightarrow -p)$.

For convenience, we can define a vector of observables for a bipartite system: $\mathbf{u} = [X_1, P_1, X_2, P_2]^T$, containing the canonical positions X_j and momenta P_j of subsystems $j \in \{1, 2\}$. For the purpose of assessing entanglement, we need only the fluctuating part of $\mathbf{u}$, so we will assume that $\mathbf{u}$ has zero mean (the steady-state value $\bar{u}_j$ of each element is subtracted off if nonzero). We also specify dimensionless canonical commutation relations between the elements of $\mathbf{u}$, as follows: $[X_j, P_k] = i\delta_{jk}$, and $[X_j, X_k] = [P_j, P_k] = 0$. Note that the dimensionless coordinates X and P are related to the usual position and momentum x, p of a mechanical oscillator via the canonical transformation $x \rightarrow \sqrt{\hbar/(m\Omega_m)}X$, $p \rightarrow \sqrt{\hbar m\Omega_m}P$.

Any Gaussian state of the system can be described by a variance matrix $\boldsymbol{V}$. This 4×4 symmetric matrix contains the second order moments between the elements of

u, and is defined as follows:

$$\boldsymbol{V} = \begin{bmatrix} \boldsymbol{V}_{11} & \boldsymbol{V}_{12} \\ \boldsymbol{V}_{12}^T & \boldsymbol{V}_{22} \end{bmatrix}; \quad \boldsymbol{V}_{jk} = \begin{bmatrix} \langle X_j X_k \rangle_+ & \langle X_j P_k \rangle_+ \\ \langle P_j X_k \rangle_+ & \langle P_j P_k \rangle_+ \end{bmatrix}. \tag{6.1}$$

Here the quantity $\langle uv \rangle_+$ denotes the symmetrized average $\langle uv + vu \rangle / 2$.

A valid variance matrix must satisfy the uncertainty principle, stated in matrix form as [131]:

$$\boldsymbol{V} + \frac{i}{2} \boldsymbol{C} \geq 0 \tag{6.2}$$

where the matrix $\boldsymbol{C}$ encodes the commutation relations: $iC_{mn} = [u_m, u_n]$. If the system is in a separable state, then the variance matrix must continue to satisfy the uncertainty principle under a partial transpose $(P_2 \rightarrow -P_2)$:

$$\boldsymbol{\Lambda} \boldsymbol{V} \boldsymbol{\Lambda} + \frac{i}{2} \boldsymbol{C} \geq 0 \tag{6.3}$$

where the matrix $\boldsymbol{\Lambda} = \mathrm{diag}(1, 1, 1, -1)$ implements the partial transpose operation. Equation (6.3) gives us a succinct necessary criterion for separability.

Finally, one may write the logarithmic negativity in terms of $\boldsymbol{V}$, as follows [12]:

$$E_N = \max \left[0, -\frac{1}{2} \ln \left(2\Sigma - 2\sqrt{\Sigma^2 - 4 \det \boldsymbol{V}} \right) \right] \tag{6.4}$$

where $\Sigma = \det \boldsymbol{V}_{11} + \det \boldsymbol{V}_{22} - 2 \det \boldsymbol{V}_{12}$.

6.3   Opto-mechanical dynamics

A schematic of the ponderomotive interferometer, in its optical trap configuration, is shown in figure 6-1. Note that in each arm cavity, the motion of the massive input mirrors can be neglected. Moreover, the antisymmetric port readout is decoupled from all disturbances common to both cavities, as discussed in chapter 3. Hence, we can limit our attention to a single mechanical mode: the differential degree of freedom.

In order to quantify the entanglement E_N according to equation (6.4), we need
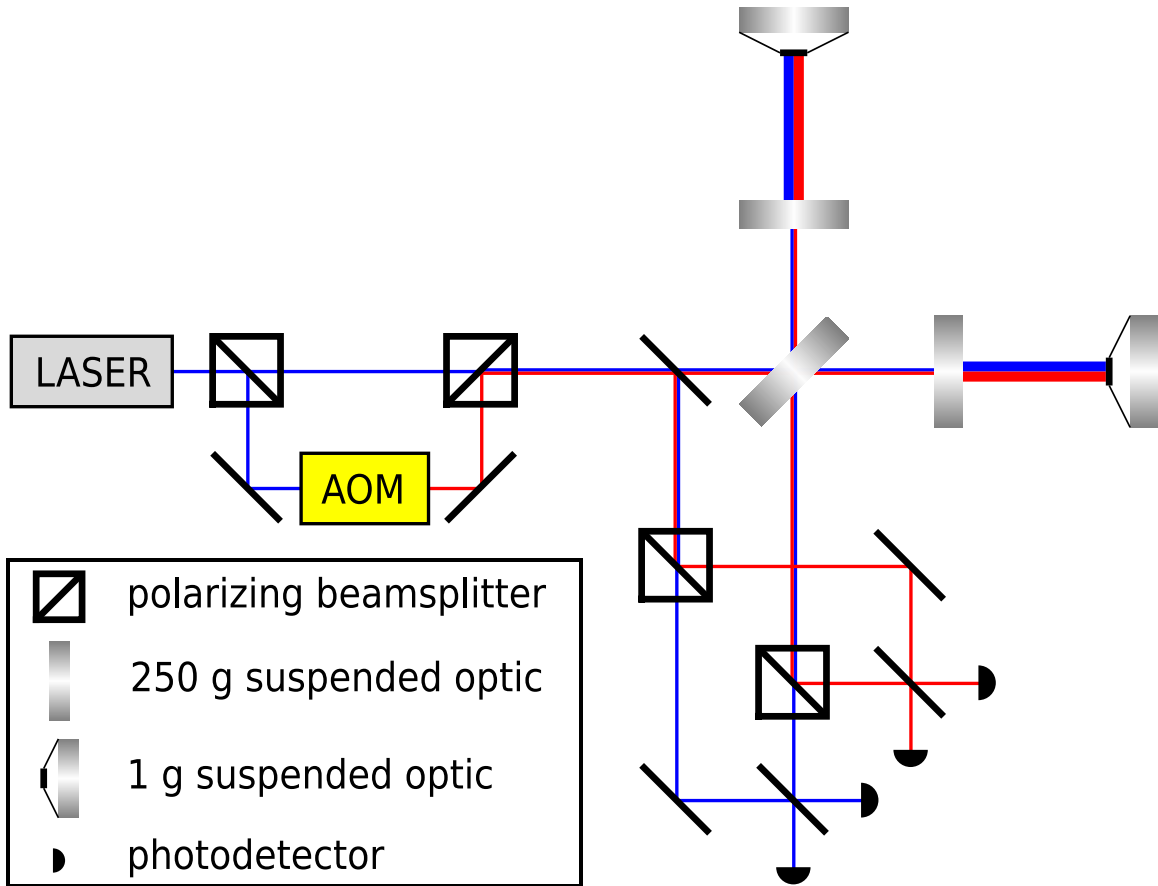
Figure 6-1: Schematic of an optical trapping and homodyne readout apparatus for the differential mode of a Fabry-Perot Michelson interferometer. Each arm cavity comprises a highly reflective, low-mass end mirror and a massive input mirror of finite transmissivity. The system is driven by two orthogonally polarized laser beams: a strong "carrier" field, and a weaker frequency-shifted "subcarrier" created by an acousto-optic modulator (AOM). Each optical field is monitored using a balanced homodyne readout. Feedback loops required to hold the interferometer on resonance are not shown.

to compute the system's second order moments. To do so, we first write down its linearized, Heisenberg-picture equations of motion. These equations can be derived using the quantum Langevin approach (cf. [53, 56, 109]). They can be expressed in the succinct form

$$\dot{\mathbf{u}}_{\text{ic}} = \boldsymbol{K}\mathbf{u}_{\text{ic}} + \mathbf{u}_{\text{in}}. \tag{6.5}$$

This operator equation relates the vector $\mathbf{u}_{\text{ic}}$ of intra-cavity coordinates, and the vector $\mathbf{u}_{\text{in}}$ of input noises driving the system, via the coupling matrix $\boldsymbol{K}$.

Elements of $\mathbf{u}_{\text{ic}} = [X, P, X_1, Y_1, X_2, Y_2]^T$ include the (dimensionless) coordinates X, P of the mirror, and the cavity mode quadrature operators defined by $X_j = (a_j^\dagger + a_j)/\sqrt{2}, Y_j = i(a_j^\dagger - a_j)/\sqrt{2}$. The input noise vector is

$$\mathbf{u}_{\text{in}} = \left[0, \frac{F_T}{\sqrt{\hbar m \Omega_m}}, \sqrt{2\gamma_c}X_{\text{in},1}, \sqrt{2\gamma_c}Y_{\text{in},1} + \frac{G_1 x_{\text{surf}}}{\sqrt{\hbar/(m\Omega_m)}}, \right.$$
$$\left. \sqrt{2\gamma_c}X_{\text{in},2}, \sqrt{2\gamma_c}Y_{\text{in},2} + \frac{G_2 x_{\text{surf}}}{\sqrt{\hbar/(m\Omega_m)}} \right]^T \tag{6.6}$$

which includes a Langevin force F_T driving Brownian motion of the mirror center of mass, the vacuum noises $X_{\text{in},j}, Y_{\text{in},j}$ entering each cavity mode, and a mirror surface displacement x_{surf} due to thermal noise of the optical coating layer. The coupling matrix is

$$\boldsymbol{K} = \begin{bmatrix} 0 & \Omega_m & 0 & 0 & 0 & 0 \\ -\Omega_m & -\Gamma_m & G_1 & 0 & G_2 & 0 \\ 0 & 0 & -\gamma_c & -\Delta_1 & 0 & 0 \\ G_1 & 0 & \Delta_1 & -\gamma_c & 0 & 0 \\ 0 & 0 & 0 & 0 & -\gamma_c & -\Delta_2 \\ G_2 & 0 & 0 & 0 & \Delta_2 & -\gamma_c \end{bmatrix}. \tag{6.7}$$

Here the cavity mode operators have been represented in the frame rotating with their drive fields, so that only their detunings appear in the equations. The

Parameter	Symbol	Value
End mirror resonant frequency	$\Omega_m/2\pi$	1 Hz
End mirror damping rate	$\Gamma_m/2\pi$	1 μHz
End mirror reduced mass	m	0.5 g
Cavity resonant frequency	$\omega_c/2\pi$	$c/(1064 \text{ nm})$
Cavity linewidth (HWHM)	$\gamma_c/2\pi$	9.5 kHz
Cavity length	L	1 m
Carrier power		5 W
Carrier detuning	δ_1	-3
Subcarrier power		0.3 W
Subcarrier detuning	δ_2	$\frac{1}{2}$
Coating noise coefficient	C	1.5×10^{-13} s^2/kg
Ambient temperature	T	300 K

Table 6.1: Ponderomotive entangler parameters and their nominal values. Note that the optical coating noise parameter C depends on both material and geometric properties of the end mirror, and is broken down further in reference [40].

opto-mechanical coupling is parametrized by

$$G_j^2 = \Omega_{q,j}^2 \frac{\gamma_c}{\Omega_m} \frac{1}{1 + \delta_j^2} \tag{6.8}$$

where $\Omega_{q,j}$ is the usual "quantum frequency" of field j, and the detuning of each field is $\Delta_j = \omega_j - (1 - \bar{x}/L)\omega_c$, with $\delta_j = \Delta_j/\gamma_c$. All other parameters are defined in table 6.1.

In the frequency domain, it is straightforward to solve equation (6.5) algebraically for $\widetilde{\mathbf{u}}_{\text{ic}}$ in terms of $\widetilde{\mathbf{u}}_{\text{in}}$ [56]. To gain insight into the solution, we begin with the case where $G_1 = G_2 = 0$, decoupling the subsystems. Then the mirror's equation of motion is that of a thermally driven pendulum, $\widetilde{x} = \chi_m(\Omega)\widetilde{F}_T$, where the mechanical susceptibility to force is given by $\chi_m(\Omega) = [m(\Omega_m^2 - i\Gamma_m\Omega - \Omega^2)]^{-1}$.

Turning on the interaction has two effects on the mirror. First, it introduces new driving terms due to radiation pressure noise. Second, it alters the mirror's response function. When motion is slow on the cavity timescale ($\Omega \ll \gamma_c$), the opto-mechanical susceptibility may still be written in the form $\chi_{\text{eff}}(\Omega) = [m(\Omega_{\text{eff}}^2 - i\Gamma_{\text{eff}}\Omega - \Omega^2)]^{-1}$, but

the system's new resonance parameters are:

$$\Omega_{\text{eff}}^2 = \Omega_m^2 + \sum_j \Omega_j^2; \quad \Omega_j^2 = \Omega_{q,j}^2 \frac{\delta_j}{2} \left(\frac{1}{1 + \delta_j^2} \right)^2$$

$$\Gamma_{\text{eff}} = \Gamma_m + \sum_j \Gamma_j; \quad \Gamma_j = -\frac{2\Omega_j^2}{\gamma_c(1 + \delta_j^2)} \tag{6.9}$$

These expressions reveal an important feature of strong radiation pressure coupling: it can create both static and dynamic instability. Considering a *single* optical field j, note that its contributions to the spring constant, $m\Omega_{\text{eff},j}^2$, and the damping rate, $\Gamma_{\text{eff},j}$, have opposite sign. If both of these terms are permitted to exceed the mechanical contributions, $m\Omega_m^2$ and Γ_m respectively, then the system becomes unstable. This follows from the presence of either an overall anti-restoring force, or an anti-damping force, depending upon which sign is chosen for the detuning δ_j. For this reason, prior studies on ponderomotive entanglement have avoided the regime where the optical spring constant dominates. However, in the presence of *two* optical fields, the coupling strengths and detunings can be chosen so that, when considered together, the effective resonant frequency and damping rate both have positive sign, and are dominated by terms of optical origin. These are the conditions needed to realize a stable optical trap [37].

Strong coupling is the prerequisite for optical trapping: strong, in particular, when compared with the mechanical resonant frequency. The optical spring constant is maximized at $\delta_j = 1/\sqrt{3}$, which leads to a criterion

$$\Omega_{\text{max},j}^2 \equiv \frac{3\sqrt{3}}{32} \Omega_q^2 \gtrsim \Omega_m^2 \tag{6.10}$$

delineating the boundary of the regime where a dominant optical spring is possible.

6.4   Output variances

The optical fields exiting the cavity are potentially quantum-correlated, due to the coupling of their intra-cavity amplitude and phase with the motion of a common mirror.
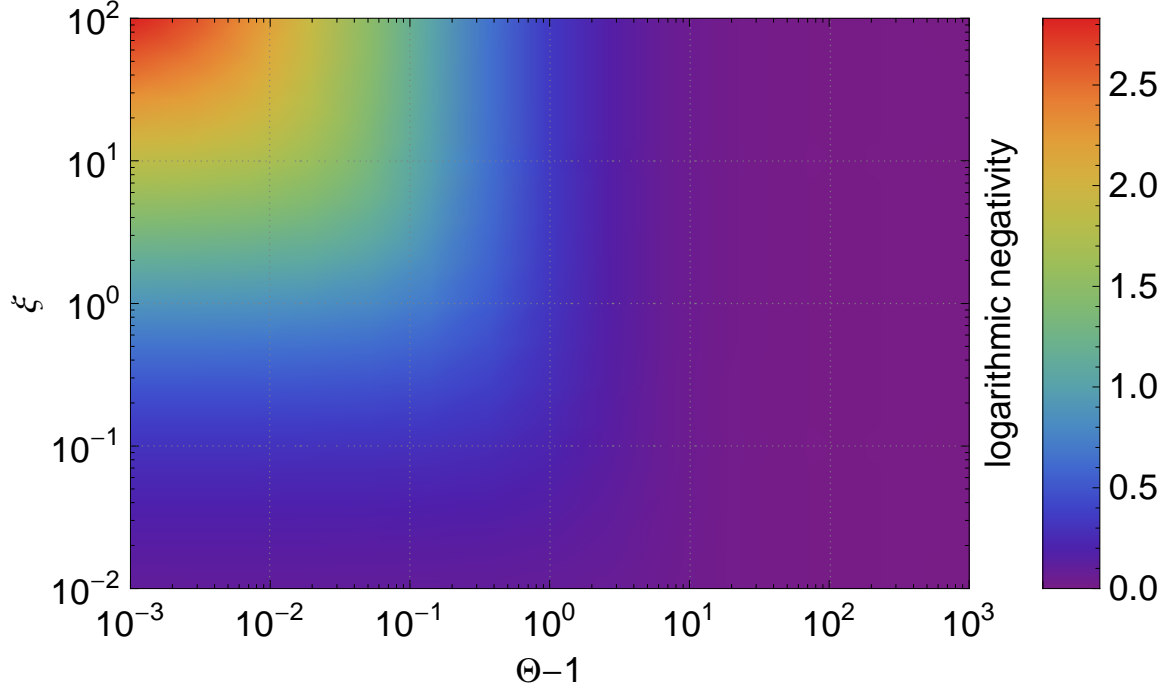
Figure 6-2: Logarithmic negativity of output carrier-subcarrier entanglement in the DC limit.

To study these correlations, the variance matrix of the output fields is obtained from the solution to equation (6.5) via the cavity input-output relation, $a_{\text{in}} + a_{\text{out}} = \sqrt{2\gamma_c} a_{\text{ic}}$. Subsequently, one finds the variance matrix of the output spatial mode at sideband frequency Ω, in terms of the power spectra of the noise inputs, which are [53, 67]*:

$$S_{F_T}(\Omega) = 2m\Gamma_m \hbar\Omega \left[\coth(\hbar\Omega/[2k_B T]) - 1\right]$$

$$S_{a_{\text{in},j}}(\Omega) = 1 \tag{6.11}$$

$$S_{x_{\text{surf}}}(\Omega) = 2\frac{C}{\Omega} k_B T$$

Applying equation (6.4) to these modes, one finds that the logarithmic negativity

---

*It should be noted that the simple temperature scaling given for the spectra of F_T and x_{surf}, although it is widely used, does not capture the range of behaviors observed for the losses of real materials as a function of temperature [66]. Our results are valid for room temperature (300 K), and for negligible thermal noise (0 K), and can be compared with other predictions using the same simple model. However, we do not attempt to model here the real behavior at intermediate temperatures.

of the output fields can be written simply in the DC limit ($\Omega \to 0$):

$$E_{N,\text{out}} = -\frac{1}{2} \ln \left(1 + 2\xi \left[\Theta - \sqrt{\Theta^2 + \xi^{-1}} \right] \right), \tag{6.12}$$

where ξ and Θ are dimensionless quantities parametrizing the entangler strength, and the degradation due to thermal noise, respectively. The dependence of $E_{N,\text{out}}$ on these quantities is depicted in figure 6-2. They are defined as:

$$\xi = \frac{4}{\delta_1 \delta_2} \frac{\Omega_1^2 \Omega_2^2}{\Omega_{\text{eff}}^4} \tag{6.13}$$

$$\Theta = 1 + \frac{1}{2} \frac{k_B T}{\hbar \Omega_m Q_m} \left(\sum_j \frac{\Omega_m^2}{\Omega_j^2 / \delta_j} \right) \tag{6.14}$$

using also the mechanical quality factor $Q_m = \Omega_m / \Gamma_m$. Note that an upper bound for ξ over all detunings is given by

$$\xi \leq \frac{1024}{27} \frac{(\Omega_{\text{max},1}^2 / \Omega_m^2)(\Omega_{\text{max},2}^2 / \Omega_m^2)}{(1 + \sum_j \Omega_j^2 / \Omega_m^2)^2}. \tag{6.15}$$

Writing ξ in this form makes explicit the connection between a strong entangler and the possibility of a strong optical spring. Unless the criterion (6.10) is satisfied by at least one field, ξ is constrained to be small.

The expression (6.14) shows how the entanglement can survive at temperatures that are strikingly high, given the mirror mechanical properties. Here the factor $k_B T / (\hbar \Omega_m Q_m)$ can be interpreted as a thermal noise figure of merit for the mechanics; it is, in fact, the limiting thermal occupation number under cold damping. The factor in parentheses represents the optical modification to the mechanical thermal noise. This factor is lower bounded over all detunings by $\sum_j \frac{\sqrt{27}}{16} \Omega_m^2 / \Omega_{\text{max},j}^2$. Hence, when the criterion (6.10) is satisfied by *both* optical fields, a large suppression of the thermal noise is possible.
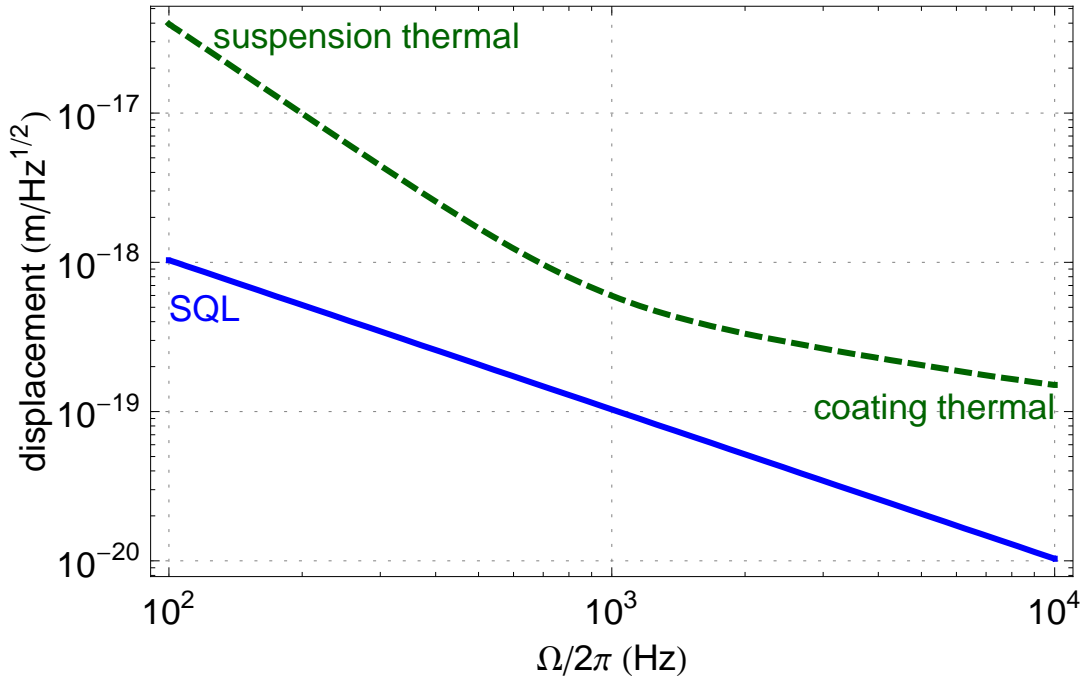
Figure 6-3: Budget of limiting classical noise sources based on the parameters of table 6.1, plotted with the Standard Quantum Limit $S_{\mathrm{SQL}}(\Omega) = 2\hbar/(m\Omega^2)$.

6.5 Experimental prospects

A real experiment must contend with technical noise sources such as seismic and laser noise, as well as the noises (vacuum, coating and suspension thermal) that are included in the treatment given here. We assume that all technical noises can be remediated, including the excess thermal noise discussed in chapter 5. This would permit the experiment to achieve the classical noise budget presented in figure 6-3, and allow us to evaluate the prospects for entanglement using the analysis described above.

Results of numerical evaluation of $E_{N,\mathrm{out}}(\Omega)$ are presented in figure 6-4, showing that entanglement of the output light should be produced within the frequency band of interest, and that it is remarkably robust against thermal noise — even surviving a room-temperature environment. The spectra are flat until suppressed by the onset of the coating noise; while in the absence of thermal noise they are cut off at the cavity linewidth $\gamma_c/2\pi \approx 9.5$ kHz. The magnitude at low frequency is well approximated by
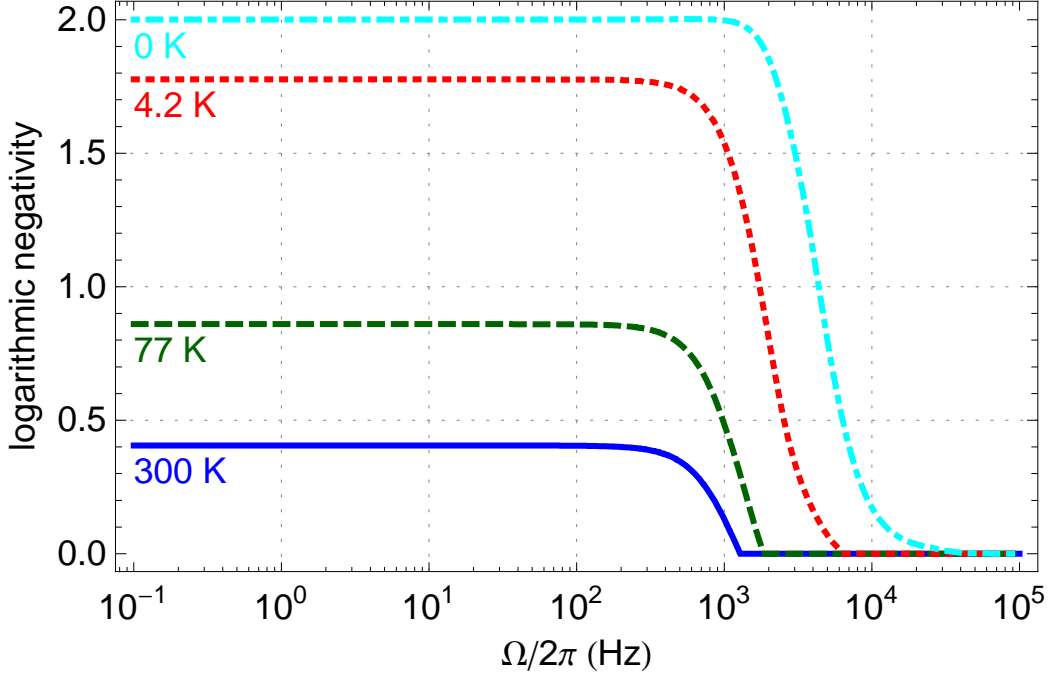
Figure 6-4: Predicted logarithmic negativity spectra for entanglement of the output carrier and subcarrier fields, plotted for various ambient temperatures.*Additional parameters are specified in table 6.1.

equation (6.12).

Given the assumptions of table 6.1, the entangler strength parameter is $\xi \approx 13.2$, and the thermal degradation parameter is $\Theta \approx 1.8$ at room temperature. In this "strong entangler" limit, one finds

$$E_{N,\text{out}} \overset{\xi \gg 1}{\to} -\frac{1}{2} \ln \left(1 - \frac{1}{\Theta} + \frac{1}{4} \frac{\xi^{-1}}{\Theta^3} \right), \tag{6.16}$$

from which it is evident that the magnitude of the negativity is being constrained solely by Θ, as depicted in figure 6-2. Although within the limits of our approximations the output entanglement never totally vanishes, a soft, low-loss suspension is necessary to avoid diminution of the logarithmic negativity by thermal noise. To capture an appreciable fraction of the available entanglement, for a suspension with $\Omega_m/2\pi \sim 1$ Hz a quality factor $Q_m \sim 10^6$ is required. This is experimentally challenging but has been achieved, for example, in suspensions constructed of monolithic fused silica [31].

Finally, we observe that homodyne detection of both output optical fields provides

a way to measure the covariance of any pair of quadratures, and hence to recover any element of the covariance matrix, permitting the entanglement borne by these fields to be quantified in an experimental setting. Such techniques have been demonstrated on entangled light produced by optical parametric oscillator systems [79, 43].

6.6 Concluding remarks

We have evaluated the capabilities of a ponderomotive entangler in a novel parameter regime that we believe is experimentally achievable. A singular feature of the system under consideration is the production of entanglement by gram-scale mechanical objects, while immersed in a room-temperature environment. In addition, the produced entanglement can link optical fields of widely separated frequencies, yielding a resource that may find applications in quantum communications and metrology [64]. An experimental demonstration of entanglement in the ponderomotive interferometer should be possible using mirror suspensions optimized for good thermal noise performance.

Chapter 7

Outlook

The experimental work presented in this thesis has pushed the current incarnation of the ponderomotive interferometer toward the quantum regime as far as it is practical to go. Further progress is constrained by the thermal noise of the 1 gram mirror suspensions. Therefore, the next era for this experiment will begin with the suspension upgrade indicated in chapter 5.

Even a modest improvement in the suspension thermal noise will open up the possibility to directly observe quantum back-action, thus validating our understanding of an important limiting noise source in Advanced LIGO. When this milestone has been achieved, the interferometer will be generating quantum correlations in its output, and so the measurement of optical squeezing (discussed in chapter 2 and reference [40]) and optical entanglement (chapter 6) can also be pursued.

The feedback cooling technique we described in chapter 4 promises an exciting future for studies of quantum mechanics in gravitational wave interferometers. As tomorrow's Advanced LIGO interferometers approach the Standard Quantum Limit, their 40 kg mirrors will become capable of approaching the ground state of motion as well.

We also note that the double optical spring configuration demonstrated in chapter 4 has been proposed as a technique to optimize the sensitivity of Advanced LIGO [118].

Injecting a squeezed optical field to reduce the quantum noise in a gravitational wave interferometer was among the earliest proposals for surpassing the Standard Quantum

Limit [34]. Shot noise reduction by this technique has recently been demonstrated in GEO600 [1] and in an Enhanced LIGO detector, although the quantum back-action was submerged in technical noise. Frequency independent squeezing would permit the Advanced LIGO detectors to achieve their designed quantum noise performance with less optical power, easing the challenge of compensating for thermal lensing in the optics. However, to take full advantage of squeezing injection will require the squeezed quadrature to have a specific optimal frequency dependence, which can be implemented by filtering the optical field using additional Fabry-Perot cavities [76]. The resulting sub-SQL quantum noise should enable the preparation of very pure quantum states of the interferometer mirrors.

The ponderomotive interferometer has a thermal noise floor due to the mirror coatings (as shown in figure 3-8), which has to be overcome before it can reach the SQL. Thomas Corbitt's group has been attempting to consolidate the best features of the ponderomotive interferometer and micro-mechanical technologies, employing a low resonant frequency, microgram scale mirror oscillator that is fabricated from AlGaAs, a high Q coating material [123]. The prospects for getting to the SQL in a tabletop experiment along these lines appear bright. AlGaAs as a coating material may also lead to reduced thermal noise for future gravitational wave detectors (beyond Advanced LIGO). There is likely to be a good deal more in the category of technological improvements that can be harvested at the interface between gravitational wave detectors and micro-opto-mechanical devices, as both fields continue to mature.

Possible applications in quantum information and communication have been contemplated for mechanical systems in the quantum regime [122]. For gravitational wave interferometers, the principal goal in exploring this regime is to obtain sensitivity improvements, but an additional motivation may be to supply fundamental tests of quantum theory at the macroscale. The theoretical debate over macroscopic quantum mechanics continues, and there are several outstanding conjectures concerning the breakdown of quantum coherence in massive systems [44, 110]. With a view to refuting or confirming such conjectures, Yanbei Chen and collaborators have reported on techniques for realizing mechanical squeezing, entanglement, and other highly non-classical

behavior in gravitational wave interferometers and related systems [99, 93, 72].

Decades of human excitement, effort, and ingenuity have left unresolved a number of persistent questions concerning gravitational waves and their putative sources, and the validity of quantum mechanics in the macroscopic domain. But the work has not gone to waste. Instead, these seemingly disparate themes have converged in the exquisitely sensitive interferometers we are building today — and the quest for answers has never been more compelling.

Symbol glossary

$a^\dagger, a$ Cavity field creation and annihilation operators (or their fluctuating parts). 34, 37

$a_{\text{in}}^\dagger, a_{\text{in}}$ Noise operators describing vacuum fluctuations of the cavity input field. 36

$\bar{x}$ Mean classical amplitude of a variable x. 36

C Coating noise coefficient. 120

c Speed of light. 23

χ Movable mirror susceptibility (transfer function of force to displacement). 37, 120

$C(\theta, \Omega)$ Transfer function of displacement to the output quadrature Y_θ. 39

d End mirror coating thickness. 44, 68

Δ Cavity detuning (angular frequency units). 26

δ Cavity detuning (dimensionless). 26

E Optical field complex amplitude; also, Young's modulus. 22, 25, 44, 68, 77, 108

$\mathcal{E}_{\text{in}}$ Cavity input field coupling rate. 35

E_N Logarithmic negativity. 116, 117

ϵ_c Contrast defect. 44, 48

$\mathcal{F}$ Cavity finesse. 26, 44, 90

l_x, l_y Optical path lengths of the arms of a Michelson interferometer. 22, 45

λ Laser wavelength. 23, 44

m Movable mirror reduced mass. 30, 44, 74, 92, 120

N Phonon occupation number. 81, 88

ω_0 Laser frequency. 23

ω_c Cavity resonant frequency. 26, 120

Ω_{eff} Movable mirror effective resonant frequency. 31

Ω_m Movable mirror mechanical resonant frequency. 31, 44, 74, 84, 92, 120

Ω_{max} Value of the optical spring resonant frequency at the cavity detuning $\delta = 1/\sqrt{3}$ for which it is maximized. 121

Ω_o Optical spring resonant frequency. 30

Ω_q Frequency where the quantum radiation pressure noise and shot noise are equalized for a displacement measurement on a free mass, achieving the Standard Quantum Limit. 30, 41

P Optical power circulating inside a cavity; also, dimensionless momentum operator. 26, 44, 92, 116

p Movable mirror momentum operator (or its fluctuating part). 34, 37

P_{AS} Optical power exiting the output (antisymmetric) port of a Michelson interferometer. 23

P_{in} Optical power applied to the input port of an interferometer. 23, 26, 44, 74, 92

ϕ Optical phase or phase difference in an interferometer; also, loss angle. 23, 25, 44, 68, 101, 108

x Movable mirror position operator (or its fluctuating part). 34, 37, 92

x_{meas} Movable mirror measured displacement. 83

x_{rms} Root-mean-square displacement. 79, 95

x_S Shot noise of the measured output quadrature Y_θ, calibrated in displacement units; also, generic displacement sensing noise. 39

x_{surf} Movable mirror surface displacement due to coating thermal noise. 119

ξ Dimensionless variable parametrizing the strength of entanglement. 123

Y Quadrature operator associated with a field's phase. 37, 39

$Z(\Omega)$ Mechanical impedance. 100

Bibliography

[1] J. Abadie et al. "A gravitational wave observatory operating beyond the quantum shot-noise limit". In: *Nature Physics* 7.12 (2011), pp. 962–965. DOI: `10.1038/nphys2083` (cit. on p. 128).

[2] J Abadie et al. "Predictions for the rates of compact binary coalescences observable by ground-based gravitational-wave detectors". In: *Classical and Quantum Gravity* 27.17 (2010), p. 173001. DOI: `10.1088/0264-9381/27/17/173001` (cit. on p. 16).

[3] B Abbott et al. "Observation of a kilogram-scale oscillator near its quantum ground state". In: *New Journal of Physics* 11.7 (2009), p. 073032. DOI: `10.1088/1367-2630/11/7/073032` (cit. on p. 90).

[4] B P Abbott et al. "LIGO: the Laser Interferometer Gravitational-Wave Observatory". In: *Reports on Progress in Physics* 72.7 (2009), p. 076901. DOI: `10.1088/0034-4885/72/7/076901` (cit. on pp. 17, 90).

[5] R. Abbott and P. King. "Control System Design for the LIGO Pre-Stabilized Laser". In: *Accelerator and Large Experimental Physics Control Systems*. Ed. by H. Shoaee. 2001, p. 361 (cit. on p. 45).

[6] R. Abbott and P. King. *(Infrared) Pre-stabilized Laser (PSL) Final Design*. LIGO Document T990025-00-D. 1999 (cit. on p. 45).

[7] R Abbott et al. "Seismic isolation enhancements for initial and Advanced LIGO". In: *Classical and Quantum Gravity* 21.5 (2004), S915. DOI: `10.1088/0264-9381/21/5/081` (cit. on p. 64).

[8]   R. S. Abbott and P. J. King. "Diode-pumped Nd:YAG laser intensity noise suppression using a current shunt". In: *Review of Scientific Instruments* 72.2 (2001), pp. 1346–1349. DOI: `10.1063/1.1334627` (cit. on p. 45).

[9]   Alex Abramovici et al. "LIGO: The Laser Interferometer Gravitational-Wave Observatory". In: *Science* 256.5055 (1992), pp. 325–333. DOI: `10.1126/science.256.5055.325` (cit. on p. 90).

[10] F Acernese et al. "Virgo status". In: *Classical and Quantum Gravity* 25.18 (2008), p. 184001. DOI: `10.1088/0264-9381/25/18/184001` (cit. on p. 17).

[11] E.G. Adelberger, B.R. Heckel, and A.E. Nelson. "Tests of the gravitational inverse-square law". In: *Annual Review of Nuclear and Particle Science* 53.1 (2003), pp. 77–121. DOI: `10.1146/annurev.nucl.53.041002.110503` (cit. on p. 101).

[12] Gerardo Adesso and Fabrizio Illuminati. "Entanglement in continuous-variable systems: recent advances and current perspectives". In: *Journal of Physics A: Mathematical and Theoretical* 40.28 (2007), p. 7821. DOI: `10.1088/1751-8113/40/28/S01` (cit. on p. 117).

[13] Rana Adhikari. "Sensitivity and Noise Analysis of 4 km Laser Interferometric Gravitational Wave Antennae". PhD thesis. Massachusetts Institute of Technology, July 2004 (cit. on pp. 55, 61).

[14] "An upper limit on the stochastic gravitational-wave background of cosmological origin". In: *Nature* 460.7258 (2009), pp. 990–994. DOI: `10.1038/nature08278` (cit. on p. 16).

[15] O. Arcizet et al. "Radiation-pressure cooling and optomechanical instability of a micromirror". In: *Nature* 444.7115 (2006), pp. 71–74. DOI: `10.1038/nature05244` (cit. on p. 73).

[16] A. D. Armour, M. P. Blencowe, and K. C. Schwab. "Entanglement and Decoherence of a Micromechanical Resonator via Coupling to a Cooper-Pair Box".

In: *Phys. Rev. Lett.* 88 (14 Mar. 2002), p. 148301. DOI: `10.1103/PhysRevLett.88.148301` (cit. on p. 113).

[17] Markus Aspelmeyer, Pierre Meystre, and Keith Schwab. "Quantum optomechanics". In: *Physics Today* 65.7 (2012), pp. 29–35. DOI: `10.1063/PT.3.1640` (cit. on p. 18).

[18] K. Audenaert, M. B. Plenio, and J. Eisert. "Entanglement Cost under Positive-Partial-Transpose-Preserving Operations". In: *Phys. Rev. Lett.* 90 (2 Jan. 2003), p. 027901. DOI: `10.1103/PhysRevLett.90.027901` (cit. on p. 116).

[19] Eric D. Black, Akira Villar, and Kenneth G. Libbrecht. "Thermoelastic-Damping Noise from Sapphire Mirrors in a Fundamental-Noise-Limited Interferometer". In: *Phys. Rev. Lett.* 93 (24 Dec. 2004), p. 241101. DOI: `10.1103/PhysRevLett.93.241101` (cit. on p. 103).

[20] S. Bose, K. Jacobs, and P. L. Knight. "Preparation of nonclassical states in cavities with a moving mirror". In: *Phys. Rev. A* 56 (5 Nov. 1997), pp. 4175–4186. DOI: `10.1103/PhysRevA.56.4175` (cit. on pp. 18, 113).

[21] W. P. Bowen et al. "Experimental Investigation of Criteria for Continuous Variable Entanglement". In: *Phys. Rev. Lett.* 90 (4 Jan. 2003), p. 043601. DOI: `10.1103/PhysRevLett.90.043601` (cit. on p. 114).

[22] V. B. Braginskiĭ and A. B. Manukin. "Ponderomotive Effects of Electromagnetic Radiation". In: *Soviet Journal of Experimental and Theoretical Physics* 25 (Oct. 1967), p. 653 (cit. on p. 28).

[23] V. B. Braginskiĭ, A. B. Manukin, and M. Y. Tikhonov. "Investigation of Dissipative Ponderomotive Effects of Electromagnetic Radiation". In: *Soviet Journal of Experimental and Theoretical Physics* 31 (1970), p. 829 (cit. on p. 28).

[24] V.B. Braginsky and A.B. Manukin. *Measurement of Weak Forces in Physics Experiments.* University Press, 1977. ISBN: 9780226070704 (cit. on p. 18).

[25]   V.B. Braginsky, S.E. Strigin, and S.P. Vyatchanin. "Analysis of parametric oscillatory instability in power recycled LIGO interferometer". In: *Physics Letters A* 305.34 (2002), pp. 111 –124. ISSN: 0375-9601. DOI: 10.1016/S0375-9601(02)01357-9 (cit. on p. 32).

[26]   V.B. Braginsky, S.E. Strigin, and S.P. Vyatchanin. "Parametric oscillatory instability in Fabry-Perot interferometer". In: *Physics Letters A* 287.56 (2001), pp. 331 –338. ISSN: 0375-9601. DOI: 10.1016/S0375-9601(01)00510-2 (cit. on pp. 32, 33).

[27]   V.B. Braginsky and S.P. Vyatchanin. "Low quantum noise tranquilizer for Fabry-Perot interferometer". In: *Physics Letters A* 293.56 (2002), pp. 228 –234. ISSN: 0375-9601. DOI: 10.1016/S0375-9601(02)00020-8 (cit. on pp. 30, 73, 114).

[28]   Vladimir B. Braginsky et al. "Noise in gravitational-wave detectors and other classical-force measurements is not influenced by test-mass quantization". In: *Phys. Rev. D* 67 (8 Apr. 2003), p. 082001. DOI: 10.1103/PhysRevD.67.082001 (cit. on p. 40).

[29]   Alessandra Buonanno and Yanbei Chen. "Signal recycled laser-interferometer gravitational-wave detectors as optical springs". In: *Phys. Rev. D* 65 (4 Jan. 2002), p. 042001. DOI: 10.1103/PhysRevD.65.042001 (cit. on pp. 30, 73, 114).

[30]   G. Cagnoli et al. "Damping dilution factor for a pendulum in an interferometric gravitational waves detector". In: *Physics Letters A* 272.12 (2000), pp. 39 –45. ISSN: 0375-9601. DOI: 10.1016/S0375-9601(00)00411-4 (cit. on p. 72).

[31]   G. Cagnoli et al. "Very High Q Measurements on a Fused Silica Monolithic Pendulum for Use in Enhanced Gravity Wave Detectors". In: *Phys. Rev. Lett.* 85 (12 Sept. 2000), pp. 2442–2445. DOI: 10.1103/PhysRevLett.85.2442 (cit. on p. 125).

[32]   Herbert B. Callen and Theodore A. Welton. "Irreversibility and Generalized Noise". In: *Phys. Rev.* 83 (1 July 1951), pp. 34–40. DOI: 10.1103/PhysRev.83.34 (cit. on p. 100).

[33] S.M. Carroll. *Spacetime and Geometry: An Introduction to General Relativity.* Prentice Hall, 2004. ISBN: 9780805387322 (cit. on p. 16).

[34] Carlton M. Caves. "Quantum-mechanical noise in an interferometer". In: *Phys. Rev. D* 23 (8 Apr. 1981), pp. 1693–1708. DOI: `10.1103/PhysRevD.23.1693` (cit. on pp. 18, 128).

[35] Carlton M. Caves. "Quantum-Mechanical Radiation-Pressure Fluctuations in an Interferometer". In: *Phys. Rev. Lett.* 45 (2 July 1980), pp. 75–79. DOI: `10.1103/PhysRevLett.45.75` (cit. on p. 18).

[36] P. F. Cohadon, A. Heidmann, and M. Pinard. "Cooling of a Mirror by Radiation Pressure". In: *Phys. Rev. Lett.* 83 (16 Oct. 1999), pp. 3174–3177. DOI: `10.1103/PhysRevLett.83.3174` (cit. on p. 83).

[37] Thomas Corbitt et al. "An All-Optical Trap for a Gram-Scale Mirror". In: *Phys. Rev. Lett.* 98 (15 Apr. 2007), p. 150802. DOI: `10.1103/PhysRevLett.98.150802` (cit. on pp. 73, 121).

[38] Thomas Corbitt et al. "Measurement of radiation-pressure-induced optomechanical dynamics in a suspended Fabry-Perot cavity". In: *Phys. Rev. A* 74 (2 Aug. 2006), p. 021802. DOI: `10.1103/PhysRevA.74.021802` (cit. on pp. 30, 32, 73, 86, 114).

[39] Thomas Corbitt et al. "Optical Dilution and Feedback Cooling of a Gram-Scale Oscillator to 6.9 mK". In: *Phys. Rev. Lett.* 99 (16 Oct. 2007), p. 160801. DOI: `10.1103/PhysRevLett.99.160801` (cit. on p. 82).

[40] Thomas Corbitt et al. "Squeezed-state source using radiation-pressure-induced rigidity". In: *Phys. Rev. A* 73 (2 Feb. 2006), p. 023801. DOI: `10.1103/PhysRevA.73.023801` (cit. on pp. 42, 73, 113, 120, 127).

[41] Thomas Randall Corbitt. "Quantum Noise and Radiation Pressure Effects in High Power Optical Interferometers". PhD thesis. Massachusetts Institute of Technology, Aug. 2008 (cit. on p. 43).

141

[42]   Stefan Danilishin et al. "Creation of a quantum oscillator by classical control". In: *arXiv/0809.2024* (2008) (cit. on pp. 89, 97).

[43]   James DiGuglielmo et al. "Experimental characterization of Gaussian quantum-communication channels". In: *Phys. Rev. A* 76 (1 July 2007), p. 012323. DOI: `10.1103/PhysRevA.76.012323` (cit. on p. 126).

[44]   L. Diósi. "A universal master equation for the gravitational violation of quantum mechanics". In: *Physics Letters A* 120.8 (1987), pp. 377 –381. ISSN: 0375-9601. DOI: `10.1016/0375-9601(87)90681-5` (cit. on p. 128).

[45]   A. Dorsel et al. "Optical Bistability and Mirror Confinement Induced by Radiation Pressure". In: *Phys. Rev. Lett.* 51 (17 Oct. 1983), pp. 1550–1553. DOI: `10.1103/PhysRevLett.51.1550` (cit. on p. 73).

[46]   R. W. P. Drever et al. "Laser phase and frequency stabilization using an optical resonator". In: *Applied Physics B: Lasers and Optics* 31 (2 1983), pp. 97–105. ISSN: 0946-2171. DOI: `10.1007/BF00702605` (cit. on pp. 55, 75).

[47]   A. Einstein, B. Podolsky, and N. Rosen. "Can Quantum-Mechanical Description of Physical Reality Be Considered Complete?" In: *Phys. Rev.* 47 (10 May 1935), pp. 777–780. DOI: `10.1103/PhysRev.47.777` (cit. on p. 113).

[48]   M. Evans. *Optickle*. LIGO Document T070260-00-D. 2007 (cit. on pp. 55, 66).

[49]   Aires Ferreira, Ariel Guerreiro, and Vlatko Vedral. "Macroscopic Thermal Entanglement Due to Radiation Pressure". In: *Phys. Rev. Lett.* 96 (6 Feb. 2006), p. 060407. DOI: `10.1103/PhysRevLett.96.060407` (cit. on p. 114).

[50]   Arthur Fine. "The Einstein-Podolsky-Rosen Argument in Quantum Theory". In: *The Stanford Encyclopedia of Philosophy*. Ed. by Edward N. Zalta. Winter 2012 edition. 2012 (cit. on p. 15).

[51]   Robert L. Forward. "Electronic damping of vibrations in optical structures". In: *Appl. Opt.* 18.5 (Mar. 1979), pp. 690–697. DOI: `10.1364/AO.18.000690` (cit. on p. 83).

[52] Tobin Thomas Fricke. "Homodyne Detection for Laser-Interferometric Gravitational Wave Detectors". PhD thesis. Louisiana State University, Dec. 2011 (cit. on p. 24).

[53] C. Gardiner and P. Zoller. *Quantum Noise: A Handbook of Markovian and Non-Markovian Quantum Stochastic Methods with Applications to Quantum Optics.* Springer Series in Synergetics. Springer, 2004. ISBN: 9783540223016 (cit. on pp. 34–36, 40, 119, 122).

[54] C. W. Gardiner and M. J. Collett. "Input and output in damped quantum systems: Quantum stochastic differential equations and the master equation". In: *Phys. Rev. A* 31 (6 June 1985), pp. 3761–3774. DOI: `10.1103/PhysRevA.31.3761` (cit. on p. 39).

[55] C. Genes et al. "Ground-state cooling of a micromechanical oscillator: Comparing cold damping and cavity-assisted cooling schemes". In: *Phys. Rev. A* 77 (3 Mar. 2008), p. 033804. DOI: `10.1103/PhysRevA.77.033804` (cit. on pp. 82, 89).

[56] S. Giannini, S. Mancini, and P. Tombesi. "Information theoretic aspects in ponderomotive systems". In: *Quantum Information and Computation* 3.3 (2003), pp. 265–279 (cit. on pp. 113, 119, 120).

[57] G. W. Gibbons and S. W. Hawking. "Theory of the Detection of Short Bursts of Gravitational Radiation". In: *Phys. Rev. D* 4 (8 Oct. 1971), pp. 2191–2197. DOI: `10.1103/PhysRevD.4.2191` (cit. on p. 16).

[58] S. Gigan et al. "Self-cooling of a micromirror by radiation pressure". In: *Nature* 444.7115 (2006), pp. 67–70. DOI: `10.1038/nature05273` (cit. on p. 73).

[59] V. Giovannetti, S. Mancini, and P. Tombesi. "Radiation pressure induced Einstein-Podolsky-Rosen paradox". In: *EPL (Europhysics Letters)* 54.5 (2001), p. 559. DOI: `10.1209/epl/i2001-00284-x` (cit. on p. 113).

[60] Vittorio Giovannetti and David Vitali. "Phase-noise measurement in a cavity with a movable mirror undergoing quantum Brownian motion". In: *Phys. Rev. A* 63 (2 Jan. 2001), p. 023812. DOI: 10.1103/PhysRevA.63.023812 (cit. on pp. 34, 35).

[61] E Goetz et al. "Accurate calibration of test mass displacement in the LIGO interferometers". In: *Classical and Quantum Gravity* 27.8 (2010), p. 084024. DOI: 10.1088/0264-9381/27/8/084024 (cit. on p. 62).

[62] E. Goulielmakis et al. "Direct Measurement of Light Waves". In: *Science* 305.5688 (2004), pp. 1267–1269. DOI: 10.1126/science.1100866 (cit. on p. 22).

[63] Andri M. Gretarsson and Gregory M. Harry. "Dissipation of mechanical energy in fused silica fibers". In: *Review of Scientific Instruments* 70.10 (1999), pp. 4081–4087. DOI: 10.1063/1.1150040 (cit. on pp. 108, 111).

[64] Nicolai B. Grosse et al. "Observation of Entanglement between Two Light Beams Spanning an Octave in Optical Frequency". In: *Phys. Rev. Lett.* 100 (24 June 2008), p. 243601. DOI: 10.1103/PhysRevLett.100.243601 (cit. on p. 126).

[65] H Grote and the LIGO Scientific Collaboration. "The GEO 600 status". In: *Classical and Quantum Gravity* 27.8 (2010), p. 084003. DOI: 10.1088/0264-9381/27/8/084003 (cit. on p. 17).

[66] G. Harry, T.P. Bodiya, and R. DeSalvo. *Optical Coatings and Thermal Noise in Precision Measurement*. Cambridge University Press, 2012. ISBN: 9781107003385 (cit. on p. 122).

[67] Gregory M Harry et al. "Thermal noise in interferometric gravitational wave detectors due to dielectric optical coatings". In: *Classical and Quantum Gravity* 19.5 (2002), p. 897. DOI: 10.1088/0264-9381/19/5/305 (cit. on pp. 68, 103, 122).

[68] Pawel Horodecki. "Separability criterion and inseparable mixed states with positive partial transposition". In: *Physics Letters A* 232.5 (1997), pp. 333 –339. ISSN: 0375-9601. DOI: `10.1016/S0375-9601(97)00416-7` (cit. on p. 115).

[69] Seiji Kawamura and Janeen Hazel. *Small Optics Suspension Final Design (Mechanical System)*. LIGO Document T970135-02-D. 1997 (cit. on p. 52).

[70] William Kells and Erika D'Ambrosio. "Considerations on parametric instability in FabryPerot interferometer". In: *Physics Letters A* 299.4 (2002), pp. 326 –330. ISSN: 0375-9601. DOI: `10.1016/S0375-9601(02)00611-4` (cit. on p. 32).

[71] D. Kennefick. *Traveling at the Speed of Thought: Einstein and the Quest for Gravitational Waves*. Princeton University Press, 2007. ISBN: 9780691117270 (cit. on p. 15).

[72] Farid Khalili et al. "Preparing a Mechanical Oscillator in Non-Gaussian Quantum States". In: *Phys. Rev. Lett.* 105 (7 Aug. 2010), p. 070403. DOI: `10.1103/PhysRevLett.105.070403` (cit. on p. 129).

[73] F.Ya. Khalili. "Reducing the mirrors coating noise in laser gravitational-wave antennae by means of double mirrors". In: *Physics Letters A* 334.1 (2005), pp. 67 –72. ISSN: 0375-9601. DOI: `10.1016/j.physleta.2004.10.078` (cit. on p. 108).

[74] A. L. Kimball and D. E. Lovell. "Internal Friction in Solids". In: *Phys. Rev.* 30 (6 Dec. 1927), pp. 948–959. DOI: `10.1103/PhysRev.30.948` (cit. on p. 101).

[75] H. J. Kimble, Benjamin L. Lev, and Jun Ye. "Optical Interferometers with Reduced Sensitivity to Thermal Noise". In: *Phys. Rev. Lett.* 101 (26 Dec. 2008), p. 260602. DOI: `10.1103/PhysRevLett.101.260602` (cit. on p. 108).

[76] H. J. Kimble et al. "Conversion of conventional gravitational-wave interferometers into quantum nondemolition interferometers by modifying their input and/or output optics". In: *Phys. Rev. D* 65 (2 Dec. 2001), p. 022002. DOI: `10.1103/PhysRevD.65.022002` (cit. on pp. 41, 97, 128).

[77] T. J. Kippenberg et al. "Analysis of Radiation-Pressure Induced Mechanical
      Oscillation of an Optical Microcavity". In: *Phys. Rev. Lett.* 95 (3 July 2005),
      p. 033901. DOI: 10.1103/PhysRevLett.95.033901 (cit. on p. 86).

[78] Dustin Kleckner and Dirk Bouwmeester. "Sub-kelvin optical cooling of a
      micromechanical resonator". In: *Nature* 444.7115 (2006), pp. 75–78. DOI: 10.
      1038/nature05231 (cit. on p. 83).

[79] Julien Laurat et al. "Entanglement of two-mode Gaussian states: characteriza-
      tion and experimental production and manipulation". In: *Journal of Optics
      B: Quantum and Semiclassical Optics* 7.12 (2005), S577. DOI: 10.1088/1464-
      4266/7/12/021 (cit. on p. 126).

[80] C. K. Law. "Interaction between a moving mirror and radiation pressure: A
      Hamiltonian formulation". In: *Phys. Rev. A* 51 (3 Mar. 1995), pp. 2537–2541.
      DOI: 10.1103/PhysRevA.51.2537 (cit. on p. 35).

[81] Peter Lebedew. "Untersuchungen über die Druckkräfte des Lichtes". In: *Annalen
      der Physik* 311.11 (1901), pp. 433–458. ISSN: 1521-3889. DOI: 10.1002/andp.
      19013111102 (cit. on p. 28).

[82] Yu. Levin. "Internal thermal noise in the LIGO test masses: A direct approach".
      In: *Phys. Rev. D* 57 (2 Jan. 1998), pp. 659–663. DOI: 10.1103/PhysRevD.57.
      659 (cit. on p. 103).

[83] James L. Levine and Richard L. Garwin. "New Negative Result for Gravitational
      Wave Detection, and Comparison with Reported Detection". In: *Phys. Rev.
      Lett.* 33 (13 Sept. 1974), pp. 794–797. DOI: 10.1103/PhysRevLett.33.794
      (cit. on p. 16).

[84] A. D. Ludlow et al. "Compact, thermal-noise-limited optical cavity for diode
      laser stabilization at 1×10^{-15}". In: *Opt. Lett.* 32.6 (Mar. 2007), pp. 641–643.
      DOI: 10.1364/OL.32.000641 (cit. on p. 101).

[85] S. Mancini, V. I. Man'ko, and P. Tombesi. "Ponderomotive control of quantum macroscopic coherence". In: *Phys. Rev. A* 55 (4 Apr. 1997), pp. 3042–3050. DOI: `10.1103/PhysRevA.55.3042` (cit. on p. 18).

[86] Stefano Mancini, David Vitali, and Paolo Tombesi. "Optomechanical Cooling of a Macroscopic Oscillator by Homodyne Feedback". In: *Phys. Rev. Lett.* 80 (4 Jan. 1998), pp. 688–691. DOI: `10.1103/PhysRevLett.80.688` (cit. on p. 83).

[87] Stefano Mancini et al. "Entangling Macroscopic Oscillators Exploiting Radiation Pressure". In: *Phys. Rev. Lett.* 88 (12 Mar. 2002), p. 120401. DOI: `10.1103/PhysRevLett.88.120401` (cit. on p. 113).

[88] William Marshall et al. "Towards Quantum Superpositions of a Mirror". In: *Phys. Rev. Lett.* 91 (13 Sept. 2003), p. 130401. DOI: `10.1103/PhysRevLett.91.130401` (cit. on p. 113).

[89] Nicolás de Mateo Smith-Lefebvre. "Techniques for Improving the Readout Sensitivity of Gravitational Wave Antennae". PhD thesis. Massachusetts Institute of Technology, June 2012 (cit. on p. 24).

[90] Nergis Mavalvala, Daniel Sigg, and David Shoemaker. "Experimental Test of an Alignment-Sensing Scheme for a Gravitational-Wave Interferometer". In: *Appl. Opt.* 37.33 (Nov. 1998), pp. 7743–7746. DOI: `10.1364/AO.37.007743` (cit. on p. 63).

[91] James Clerk Maxwell. "A Treatise on Electricity and Magnetism". In: vol. 2. Clarendon Press Series. Oxford: Clarendon Press, 1873. Chap. 20, p. 391 (cit. on p. 27).

[92] C H Metzger and K Karrai. "Cavity cooling of a microlever". In: *Nature* 432.7020 (2004), pp. 1002–1005. DOI: `10.1038/nature03118` (cit. on p. 73).

[93] Haixing Miao et al. "Probing macroscopic quantum states with a sub-Heisenberg accuracy". In: *Phys. Rev. A* 81 (1 Jan. 2010), p. 012114. DOI: `10.1103/PhysRevA.81.012114` (cit. on p. 129).

[94] Albert A. Michelson. "The relative motion of the Earth and of the Luminiferous Ether". In: *American Journal of Science* 22.128 (1881), pp. 120–129 (cit. on p. 22).

[95] C. W. Misner et al. "Gravitational Synchrotron Radiation in the Schwarzschild Geometry". In: *Phys. Rev. Lett.* 28 (15 Apr. 1972), pp. 998–1001. DOI: `10.1103/PhysRevLett.28.998` (cit. on p. 16).

[96] Osamu Miyakawa et al. "Measurement of optical response of a detuned resonant sideband extraction gravitational wave detector". In: *Phys. Rev. D* 74 (2 July 2006), p. 022001. DOI: `10.1103/PhysRevD.74.022001` (cit. on pp. 30, 73, 114).

[97] G. E. Moss, L. R. Miller, and R. L. Forward. "Photon-Noise-Limited Laser Transducer for Gravitational Antenna". In: *Appl. Opt.* 10.11 (Nov. 1971), pp. 2495–2498. DOI: `10.1364/AO.10.002495` (cit. on p. 16).

[98] Benoît Mours, Edwige Tournefier, and Jean-Yves Vinet. "Thermal noise reduction in interferometric gravitational wave antennas: using high order TEM modes". In: *Classical and Quantum Gravity* 23.20 (2006), p. 5777. DOI: `10.1088/0264-9381/23/20/001` (cit. on p. 108).

[99] Helge Müller-Ebhardt et al. "Entanglement of Macroscopic Test Masses and the Standard Quantum Limit in Laser Interferometry". In: *Phys. Rev. Lett.* 100 (1 Jan. 2008), p. 013601. DOI: `10.1103/PhysRevLett.100.013601` (cit. on pp. 97, 114, 129).

[100] A. Naik et al. "Cooling a nanomechanical resonator with quantum back-action". In: *Nature* 443.7108 (2006), pp. 193–196. DOI: `10.1038/nature05027` (cit. on p. 73).

[101] Abraham R Neben et al. "Structural thermal noise in gram-scale mirror oscillators". In: *New Journal of Physics* 14.11 (2012), p. 115008. DOI: `10.1088/1367-2630/14/11/115008` (cit. on p. 103).

[102]   E. F. Nichols and G. F. Hull. "A Preliminary Communication on the Pressure of Heat and Light Radiation". In: *Phys. Rev. (Series I)* 13 (5 Nov. 1901), pp. 307–320. DOI: `10.1103/PhysRevSeriesI.13.307` (cit. on p. 28).

[103]   Kenji Numata, Amy Kemery, and Jordan Camp. "Thermal-Noise Limit in the Frequency Stabilization of Lasers with Rigid Cavities". In: *Phys. Rev. Lett.* 93 (25 Dec. 2004), p. 250602. DOI: `10.1103/PhysRevLett.93.250602` (cit. on p. 101).

[104]   Kenji Numata et al. "Wide-Band Direct Measurement of Thermal Fluctuations in an Interferometer". In: *Phys. Rev. Lett.* 91 (26 Dec. 2003), p. 260602. DOI: `10.1103/PhysRevLett.91.260602` (cit. on p. 103).

[105]   Harry F. Olson. "Electronic Control of Noise, Vibration, and Reverberation". In: *The Journal of the Acoustical Society of America* 28.5 (1956), pp. 966–972. DOI: `10.1121/1.1908532` (cit. on p. 83).

[106]   Christian D Ott. "The gravitational-wave signature of core-collapse supernovae". In: *Classical and Quantum Gravity* 26.6 (2009), p. 063001. DOI: `10.1088/0264-9381/26/6/063001` (cit. on p. 16).

[107]   Z. Y. Ou et al. "Realization of the Einstein-Podolsky-Rosen paradox for continuous variables". In: *Phys. Rev. Lett.* 68 (25 June 1992), pp. 3663–3666. DOI: `10.1103/PhysRevLett.68.3663` (cit. on p. 114).

[108]   A. F. Pace, M. J. Collett, and D. F. Walls. "Quantum limits in interferometric detection of gravitational radiation". In: *Phys. Rev. A* 47 (4 Apr. 1993), pp. 3173–3189. DOI: `10.1103/PhysRevA.47.3173` (cit. on p. 34).

[109]   M. Paternostro et al. "Creating and Probing Multipartite Macroscopic Entanglement with Light". In: *Phys. Rev. Lett.* 99 (25 Dec. 2007), p. 250401. DOI: `10.1103/PhysRevLett.99.250401` (cit. on pp. 114, 119).

[110]   Roger Penrose. "On Gravity's role in Quantum State Reduction". In: *General Relativity and Gravitation* 28 (5 1996), pp. 581–600. ISSN: 0001-7701. DOI: `10.1007/BF02105068` (cit. on p. 128).

[111] Asher Peres. "Separability Criterion for Density Matrices". In: *Phys. Rev. Lett.* 77 (8 Aug. 1996), pp. 1413–1415. DOI: `10.1103/PhysRevLett.77.1413` (cit. on p. 115).

[112] M. Pinard et al. "Entangling movable mirrors in a double-cavity system". In: *EPL (Europhysics Letters)* 72.5 (2005), p. 747. DOI: `10.1209/epl/i2005-10317-6` (cit. on p. 113).

[113] M. Pinard et al. "Full mechanical characterization of a cold damped mirror". In: *Phys. Rev. A* 63 (1 Dec. 2000), p. 013808. DOI: `10.1103/PhysRevA.63.013808` (cit. on p. 95).

[114] Stefano Pirandola et al. "Macroscopic Entanglement by Entanglement Swapping". In: *Phys. Rev. Lett.* 97 (15 Oct. 2006), p. 150403. DOI: `10.1103/PhysRevLett.97.150403` (cit. on p. 113).

[115] F. A. E. Pirani. "Invariant Formulation of Gravitational Radiation Theory". In: *Phys. Rev.* 105 (3 Feb. 1957), pp. 1089–1099. DOI: `10.1103/PhysRev.105.1089` (cit. on p. 16).

[116] M. B. Plenio. "Logarithmic Negativity: A Full Entanglement Monotone That is not Convex". In: *Phys. Rev. Lett.* 95 (9 Aug. 2005), p. 090503. DOI: `10.1103/PhysRevLett.95.090503` (cit. on p. 116).

[117] M. Poggio et al. "Feedback Cooling of a Cantilever's Fundamental Mode below 5 mK". In: *Phys. Rev. Lett.* 99 (1 July 2007), p. 017201. DOI: `10.1103/PhysRevLett.99.017201` (cit. on pp. 83, 95).

[118] Henning Rehbein et al. "Double optical spring enhancement for gravitational-wave detectors". In: *Phys. Rev. D* 78 (6 Sept. 2008), p. 062003. DOI: `10.1103/PhysRevD.78.062003` (cit. on p. 127).

[119] Norna A Robertson. "Laser interferometric gravitational wave detectors". In: *Classical and Quantum Gravity* 17.15 (2000), R19. DOI: `10.1088/0264-9381/17/15/201` (cit. on p. 72).

[120] Jameson Rollins et al. "Solid-state laser intensity stabilization at the 10^{-8} level". In: *Opt. Lett.* 29.16 (Aug. 2004), pp. 1876–1878. DOI: 10.1364/OL.29.001876 (cit. on p. 46).

[121] Jameson Graef Rollins. "Intensity Stabilization of a Solid-State Laser for Interferometric Gravitational Wave Detectors". MA thesis. Massachusetts Institute of Technology, Feb. 2004 (cit. on p. 45).

[122] Amir H Safavi-Naeini and Oskar Painter. "Proposal for an optomechanical traveling wave phonon-photon translator". In: *New Journal of Physics* 13.1 (2011), p. 013017. DOI: 10.1088/1367-2630/13/1/013017 (cit. on p. 128).

[123] S. R. Sankar et al. "Brownian noise and route to quantum fluctuations in a microgram oscillator". Manuscript in preparation (cit. on p. 128).

[124] Peter R. Saulson. "Thermal noise in mechanical experiments". In: *Phys. Rev. D* 42 (8 Oct. 1990), pp. 2437–2445. DOI: 10.1103/PhysRevD.42.2437 (cit. on p. 72).

[125] R. L. Savage, P. J. King, and S. U. Seel. "A Highly Stabilized 10-Watt Nd:YAG Laser for the Laser Interferometer Gravitational-Wave Observatory (LIGO)". In: *Laser Physics* 8.3 (1998), pp. 679–685 (cit. on p. 45).

[126] A. Schliesser et al. "Radiation Pressure Cooling of a Micromechanical Oscillator Using Dynamical Backaction". In: *Phys. Rev. Lett.* 97 (24 Dec. 2006), p. 243905. DOI: 10.1103/PhysRevLett.97.243905 (cit. on p. 73).

[127] L. Schnupp. In: *European Collaboration Meeting on Interferometric Detection of Gravitational Waves*. Sorrento, Italy, 1988 (cit. on p. 55).

[128] Benjamin S. Sheard et al. "Observation and characterization of an optical spring". In: *Phys. Rev. A* 69 (5 May 2004), p. 051801. DOI: 10.1103/PhysRevA.69.051801 (cit. on pp. 30, 73, 114).

[129] John A. Sidles and Daniel Sigg. "Optical torques in suspended Fabry-Perot interferometers". In: *Physics Letters A* 354.3 (2006), pp. 167 –172. ISSN: 0375-9601. DOI: 10.1016/j.physleta.2006.01.051 (cit. on p. 49).

[130] Ch. Silberhorn et al. "Generation of Continuous Variable Einstein-Podolsky-Rosen Entanglement via the Kerr Nonlinearity in an Optical Fiber". In: *Phys. Rev. Lett.* 86 (19 May 2001), pp. 4267–4270. DOI: `10.1103/PhysRevLett.86.4267` (cit. on p. 114).

[131] R. Simon. "Peres-Horodecki Separability Criterion for Continuous Variable Systems". In: *Phys. Rev. Lett.* 84 (12 Mar. 2000), pp. 2726–2729. DOI: `10.1103/PhysRevLett.84.2726` (cit. on pp. 116, 117).

[132] P H Sneddon et al. "The intrinsic mechanical loss factor of hydroxy-catalysis bonds for use in the mirror suspensions of gravitational wave detectors". In: *Classical and Quantum Gravity* 20.23 (2003), p. 5025. DOI: `10.1088/0264-9381/20/23/006` (cit. on p. 111).

[133] R. Takahashi et al. "Control of a 10 m delay-line laser interferometer using the pre-modulation method". In: *Physics Letters A* 187.2 (1994), pp. 157 –162. ISSN: 0375-9601. DOI: `10.1016/0375-9601(94)90054-X` (cit. on p. 55).

[134] J. H. Taylor, L. A. Fowler, and P. M. McCulloch. "Measurements of general relativistic effects in the binary pulsar PSR1913+16". In: *Nature* 277.5696 (1979), pp. 437–440. DOI: `10.1038/277437a0` (cit. on p. 16).

[135] J. A. Tyson. "Null Search for Bursts of Gravitational Radiation". In: *Phys. Rev. Lett.* 31 (5 July 1973), pp. 326–329. DOI: `10.1103/PhysRevLett.31.326` (cit. on p. 16).

[136] D. Vitali et al. "Optomechanical Entanglement between a Movable Mirror and a Cavity Field". In: *Phys. Rev. Lett.* 98 (3 Jan. 2007), p. 030405. DOI: `10.1103/PhysRevLett.98.030405` (cit. on pp. 18, 114).

[137] Vladan Vuletić and Steven Chu. "Laser Cooling of Atoms, Ions, or Molecules by Coherent Scattering". In: *Phys. Rev. Lett.* 84 (17 Apr. 2000), pp. 3787–3790. DOI: `10.1103/PhysRevLett.84.3787` (cit. on p. 71).

[138]   J. Weber. "Detection and Generation of Gravitational Waves". In: *Phys. Rev.* 117 (1 Jan. 1960), pp. 306–313. DOI: 10.1103/PhysRev.117.306 (cit. on p. 16).

[139]   J. Weber. "Evidence for Discovery of Gravitational Radiation". In: *Phys. Rev. Lett.* 22 (24 June 1969), pp. 1320–1324. DOI: 10.1103/PhysRevLett.22.1320 (cit. on p. 16).

[140]   Rainer Weiss. "Electromagnetically Coupled Broadband Gravitational Antenna". In: *Quarterly Progress Report, Research Laboratory of Electronics (MIT)* 105 (1972), p. 54 (cit. on p. 16).

[141]   B. Willke et al. "Spatial and temporal filtering of a 10-W Nd:YAG laser with a Fabry–Perot ring-cavity premode cleaner". In: *Opt. Lett.* 23.21 (Nov. 1998), pp. 1704–1706. DOI: 10.1364/OL.23.001704 (cit. on p. 45).

[142]   Christopher Wipf et al. "Route to ponderomotive entanglement of light via optically trapped mirrors". In: *New Journal of Physics* 10.9 (2008), p. 095017. DOI: 10.1088/1367-2630/10/9/095017 (cit. on p. 113).

[143]   Jing Zhang, Kunchi Peng, and Samuel L. Braunstein. "Quantum-state transfer from light to macroscopic oscillators". In: *Phys. Rev. A* 68 (1 July 2003), p. 013808. DOI: 10.1103/PhysRevA.68.013808 (cit. on p. 113).

[144]   C. Zhao et al. "Parametric Instabilities and Their Control in Advanced Interferometer Gravitational-Wave Detectors". In: *Phys. Rev. Lett.* 94 (12 Apr. 2005), p. 121102. DOI: 10.1103/PhysRevLett.94.121102 (cit. on p. 32).

[145]   Yi Zhao et al. "Suppression of extraneous thermal noise in cavity optomechanics". In: *Opt. Express* 20.4 (Feb. 2012), pp. 3586–3612. DOI: 10.1364/OE.20.003586 (cit. on p. 108).